

---

Britta Zieser

Probing the Matter Distribution  
on Intermediate and Large Scales  
with Weak Light Deflections

---



# Dissertation

submitted to the  
Combined Faculties of the Natural Sciences and Mathematics  
of the Ruperto-Carola University of Heidelberg, Germany  
for the degree of  
Doctor of Natural Sciences

Put forward by  
**Britta Zieser**  
born in Düsseldorf  
Oral examination: July 8, 2015



# Probing the Matter Distribution on Intermediate and Large Scales with Weak Light Deflections

---

Referees: Prof. Dr. Matthias Bartelmann  
Prof. Dr. Volker Springel



## Untersuchungen der Materieverteilung auf mittleren und großen Skalen anhand schwacher Lichtablenkungen

Der Gravitationslinseneffekt kann das kosmische Dichtefeld, seine Entwicklung und die Geometrie der Raumzeit eingrenzen. Im ersten Teil dieser Dissertation zeige ich, wie aus Beobachtungen des schwachen Linseneffekts Informationen über den inneren Aufbau von Galaxienhaufen gewonnen werden können. Ich stelle einen neuen Ansatz vor, der nicht auf Symmetrieanahmen oder parametrischen Modellen beruht, sondern auf einer translationsinvarianten geometrischen Beschreibung anhand von Minkowski-Funktionalen aufbaut. Ein integrales Maß für die Konvergenz wird aus dem Scherungsfeld errechnet. Das Verhalten von Exkursionsmengen dieses Schätzers für verschiedene Schwellen kennzeichnet die Morphologie der Masseverteilung. Eine intrinsische Skala im Dichteprofil offenbart sich in einer Änderung der logarithmischen Steigung des ersten Minkowski-Funktionalen. Ich zeige, wie das charakteristische Rauschprofil des Dichte-Schätzers die Messung beeinflusst, und entwickle eine Strategie, die die Unterscheidung zwischen einem skalenbehafteten Profil und einem Potenzgesetz ermöglicht.

Im zweiten Teil beschäftige ich mich mit Kreuzkorrelationen zwischen dem schwachen Linseneffekt und dem integrierten Sachs-Wolfe-Effekt. Ich behandle die kosmische Scherung als dreidimensionale Observable und entwickle einen Formalismus, in dem die Kovarianz beider Signale berechnet werden kann. Für die numerische Auswertung wurde eine hocheffiziente Methode implementiert, deren Zuverlässigkeit und Leistungsfähigkeit ich in einer Fisher-Analyse demonstriere. Für einen Datensatz von der Qualität zukünftiger Beobachtungsmissionen wie beispielsweise des Euclid-Satelliten verringert die Berücksichtigung der Kreuzkorrelation zwischen den beiden Signalen den Fehler kosmologischer Parameter um zehn Prozent.

## Probing the Matter Distribution on Intermediate and Large Scales with Weak Light Deflections

Gravitational lensing can constrain the cosmic density field, its evolution and spacetime geometry. In the first part of this dissertation I demonstrate how information about the internal structure of galaxy clusters can be gained from observations of weak gravitational lensing. I present a novel approach which does not rely on symmetry assumptions or parametric models, but is instead built on a translation-invariant geometric description using Minkowski functionals. An integral measure of the convergence is constructed from the shear field. The behaviour of excursion sets of this estimator for varying thresholds characterises the morphology of the mass distribution. An intrinsic scale in the density profile manifests itself in a change of the logarithmic slope of the first Minkowski functional. I show how the characteristic noise profile of the density estimator affects the measurement and develop a strategy which permits the discrimination between a scale-rich profile and a power law.

In the second part I study cross-correlations between weak lensing and the integrated Sachs-Wolfe effect. I treat cosmic shear as a three-dimensional observable and develop a formalism in which the covariance of both signals can be calculated. For the numerical evaluation a highly efficient method was implemented, the performance and reliability of which I demonstrate in a Fisher analysis. For a data set of the quality of upcoming survey missions like the Euclid satellite, taking the cross-correlation between the two signals into account lowers the error on cosmological parameters by ten per cent.



# Contents

<b>Abstract</b>	<b>v</b>
<b>Table of Contents</b>	<b>vii</b>
<b>List of Figures</b>	<b>ix</b>
<b>List of Tables</b>	<b>x</b>
<b>1. Introduction</b>	<b>1</b>
<b>2. Cosmology</b>	<b>5</b>
2.1. The Friedmann-Lemaître-Robertson-Walker Universe . . . . .	5
2.2. The Case for Dark Energy . . . . .	8
<b>3. Gravitational Lensing</b>	<b>11</b>
3.1. Light Deflection and Image Distortion . . . . .	11
3.2. Lensing by Individual Objects . . . . .	14
<b>4. Structure Formation and Properties of Dark Matter Haloes</b>	<b>17</b>
4.1. The Growth of Density Fluctuations . . . . .	17
4.2. The Cosmic Microwave Background . . . . .	21
4.3. The Formation of Haloes . . . . .	24
<b>5. Construction of an Integral Density Estimator</b>	<b>29</b>
5.1. Available Data and Methods of Analysis . . . . .	29
5.2. Derivation of the $\zeta$ -Statistics . . . . .	31
5.3. Application . . . . .	34
5.4. Discussion . . . . .	40
<b>6. Minkowski Functionals as Measures of Galaxy Cluster Morphology</b>	<b>41</b>
6.1. Minkowski Functionals . . . . .	41
6.2. Application to the $\zeta$ -Statistics . . . . .	43
6.3. Noise . . . . .	45
6.4. Discrimination between NFW and Power Law Profiles . . . . .	51
6.5. Discussion . . . . .	53
<b>7. <i>3d</i> Cosmic Shear and the Integrated Sachs-Wolfe Effect</b>	<b>57</b>
7.1. Cosmic Shear . . . . .	57
7.2. The Integrated Sachs-Wolfe Effect . . . . .	61
7.3. Implementation . . . . .	62
7.4. Survey Characteristics . . . . .	67
7.5. Spectra and Correlations . . . . .	68
7.6. Cosmological Constraints . . . . .	70
7.7. Discussion . . . . .	77

<b>8. Conclusions</b>	<b>81</b>
<b>A. Parametrisation of Nested Curves</b>	<b>85</b>
<b>Bibliography</b>	<b>89</b>
<b>Acknowledgments</b>	<b>101</b>

# List of Figures

3.1. Illustration of the distortion induced by the convergence and the components of the shear. . . . .	14
4.1. Non-linear matter power spectrum at different redshifts, and the linear power spectrum today. . . . .	20
4.2. Angular power spectrum of the CMB temperature. . . . .	23
4.3. The NFW density profile. . . . .	26
5.1. Illustration of the geometry and nomenclature for the generalised $\zeta$ -statistics. . . . .	35
5.2. Weights for the two shear components for the $\zeta$ -statistics. . . . .	36
5.3. Weights for the first shear component for the $\zeta$ -statistics, for a smaller smoothing scale and an off-centre aperture position. . . . .	36
5.4. Noise contribution to the $\zeta$ -statistics for a $20' \times 20'$ -field and a smoothing scale of $0.6'$ . . . . .	38
5.5. Signal-to-noise ratio of the $\zeta$ -statistics as a function of the smoothing scale, for three NFW haloes. . . . .	39
6.1. The first Minkowski functional of the convergence as a function of the excursion set threshold for NFW haloes of the same mass or concentration. . . . .	43
6.2. Map and first Minkowski functional of the smoothed convergence for an NFW halo with $c = 4$ and $M = 10^{15} h^{-1} M_{\odot}$ . . . . .	45
6.3. As Fig. 6.2, but for a halo with $c = 6$ . . . . .	46
6.4. Minkowski functional of the $\zeta$ -statistics for different source densities. . . . .	46
6.5. Minkowski functional of the $\zeta$ -statistics of an empty field, illustrating the noise characteristics. . . . .	48
6.6. Measured and ideal convergence values along a single row of the map. . . . .	49
6.7. First Minkowski functional of the $\zeta$ -statistics for different variance limits. . . . .	49
6.8. Illustration of the excursion sets at different thresholds. . . . .	50
6.9. Histograms of the sizes of connected components of the excursion set at different thresholds. . . . .	51
6.10. First Minkowski functional of the largest connected component of the excursion set as a function of the threshold. . . . .	52
6.11. Comparison between the Minkowski functionals of the smoothed convergence for NFW and SIS haloes with the same Einstein radius. . . . .	53
6.12. Measured Minkowski functional compared to an SIS with the same Einstein radius. . . . .	54
7.1. Source-redshift distributions for two weak lensing surveys. . . . .	67
7.2. Weak lensing covariance for a stage IV survey, for four different multipole orders. . . . .	69
7.3. Spectrum of the iSW effect, and the cross-correlation with cosmic shear. . . . .	69
7.4. Signal-to-noise ratio as a function of the maximum multipole order for two weak lensing surveys. . . . .	70
7.5. Confidence regions for cosmological parameters derived from a stage III weak lensing survey and iSW data. . . . .	73
7.6. Confidence regions from the combination of cosmic shear with a stage III survey and the iSW effect, with and without information from cross-correlations. . . . .	74

7.7. Contributions of different angular scales to the $w_0w_0$ -element of the Fisher matrix for stage III and stage IV weak lensing experiments. . . . .	75
7.8. Confidence regions for cosmological parameters derived from a stage IV weak lensing survey and iSW data. . . . .	76
7.9. Confidence regions from a stage IV weak lensing survey and a CMB prior. . . . .	77

## List of Tables

7.1. Specifications of weak-lensing surveys. . . . .	67
7.2. Values of the cosmological parameters in the fiducial model assumed for the error forecast. . . . .	71
7.3. Marginal errors on cosmological parameters from three-dimensional weak lensing combined with an iSW experiment. . . . .	72
7.4. Marginal errors on cosmological parameters from a cosmic shear survey and the iSW effect, combined with a CMB prior. . . . .	75

# 1

## Chapter 1

---

# Introduction

Gravitational lensing is one of the most direct predictions of Einstein's general theory of relativity, which couples the curvature of spacetime to its matter and energy content. Light is deflected according to the geometric signature of the matter distribution, giving rise to the displacement, distortion and magnification of images. The deflection is sensitive only to mass, irrespective of the physical state of matter, which has made gravitational lensing one of the most important observational tools for the analysis of dark matter. As the propagation of light also probes the evolution of structures and the expansion history of the Universe, gravitational lensing can put valuable constraints on the parameters of the cosmological model. In this dissertation I develop two methods to extract information about the matter distribution from the shear pattern of galaxy images, on the one hand for individual objects and on the other hand on cosmological scales.

The first part of the dissertation is concerned with the morphology of galaxy clusters. Clusters typically contain up to a few hundred galaxies, amounting to masses of  $10^{14}$ – $10^{15} M_{\odot}$  (Voit, 2005). Baryons make up about 15 per cent of the total mass, with only a small fraction condensed into stars and the rest constituting the intracluster medium (ICM) of hot gas (Rosati et al., 2002). Much information about the mass distribution has been derived from gravitational lensing. Their high densities make galaxy clusters efficient strong lenses, producing arcs and multiple images of background galaxies (Soucail et al., 1987; Paczynski, 1987; Hammer et al., 1989; Lynds & Petrosian, 1989). The locations and shapes of arcs reveal typical features of the matter in clusters and its distribution: the high mass-to-light ratio necessary to account for observed Einstein radii suggests the existence of a dark component (Hammer & Rigaut, 1989); the curvature of arcs can only be modelled successfully if the distribution of the dark component is smoother than that of the visible light, i.e. dark matter appears to be present outside the haloes of galaxies (Bergmann et al., 1990); the thinness of arcs implies a steep density profile (Hammer, 1991; Miralda-Escude, 1992); the lack of counterarcs argues against axisymmetry (Grossman & Narayan, 1988; Kovner, 1989); and 'straight arcs' can be explained by the presence of considerable substructure (Kassiola et al., 1992). Furthermore, the existence of radial arcs requires a finite core radius (Bartelmann, 1996; Luppino et al., 1999), while their locations and abundance constrain its size (Fort et al., 1992; Mellier et al., 1993) and the central slope (Miralda-Escude, 1995; Molikawa & Hattori, 2001).

In numerical simulations dark matter haloes were found to have cuspy profiles rather than flat cores (Navarro et al., 1996, 1997; Jing, 2000), most commonly described by the Navarro-Frenk-White profile (NFW hereafter), which is flatter than isothermal in the centre, but steeper outside a 'scale radius'. Since its introduction the NFW model has proven a good match for many observations, such as Clowe et al. (2000); Clowe & Schneider (2001); Kneib et al. (2003); Mandelbaum et al. (2006). It is characterised by two parameters, the total mass and the concentration, defined as the ratio of the virial radius and the scale radius, which are not expected to be independent: the central density reflects the mean matter density of the Universe at the time of the formation of the halo. In a 'bottom-up' scenario of structure growth, typical for cold dark matter, the smallest haloes are the first to assemble and

therefore have the highest concentrations. This concentration-mass relation has been calibrated on numerical simulations (e.g. [Bullock et al., 2001](#); [Hennawi et al., 2007](#)). Until recently, the concentration parameters measured for strong lenses were on average too high ([Broadhurst et al., 2005](#); [Comerford & Natarajan, 2007](#); [Broadhurst et al., 2008](#)), apparently contradicting cold dark matter scenarios of structure formation. This ‘overconcentration problem’ has been attributed partly to a selection bias: as the efficiency of a halo as a strong lens increases with the concentration, a sample of clusters featuring arcs must be expected to favour unusually high concentrations ([Fedeli et al., 2007](#)). In addition, a lensing-selected sample preferentially contains clusters that are elongated along the line of sight ([Oguri et al., 2003](#)). Since lensing phenomena depend on the projected mass distribution, the density is overestimated for this orientation ([Miralda-Escude, 1993](#)). On the other hand, baryonic physics affect the density in cluster cores, giving rise to possible discrepancies to cold dark matter simulations. [Sand et al. \(2003\)](#) found evidence for a central slope that is even shallower than the NFW profile. Most recently, [Merten et al. \(2014\)](#) demonstrated that the concentration-mass relation of the X-ray selected CLASH cluster sample is in excellent agreement with numerical simulations.

Despite the support for shallow cores and steep outer profiles, isothermal models reproduce observations surprisingly well for many data sets in both the strong ([Smith et al., 2001](#); [Gavazzi et al., 2003](#); [Shu et al., 2008](#)) and the weak regime of lensing ([Sheldon et al., 2001](#); [Athreya et al., 2002](#)). [King & Schneider \(2001\)](#) investigated the ability to distinguish between NFW and power law profiles from shear data alone and found a strong dependence on the field size and the source density. Confidence in the discrimination was low when a simulated halo rather than an ideal NFW lens was considered ([King et al., 2001](#)).

A critical assessment of the concentration seems appropriate. The concentration parameter should be viewed as a fitting descriptor of the density field only if it is indeed well approximated by the model assumed for the calculation. Usually prejudices are imposed, such as axisymmetry or a particular parametric shape, or the location of a ‘centre’, though it is by no means obvious how this should be defined for an irregular distribution even in numerical simulations – it could be the centre of mass, for example, or the most gravitationally bound particle. In this dissertation I present a non-parametric analysis which is translation- and rotation-invariant. The mass distribution is measured by means of an integral estimator, which is calculated from weak lensing observations. A morphological characterisation based on the geometry of excursion sets of the convergence estimator is suggested. Integral geometry supplies a set of morphological descriptors in the form of the Minkowski functionals, which have the desired invariance properties. To demonstrate how the presence of an intrinsic scale in the density distribution manifests itself in the behaviour of the Minkowski functionals of excursion sets, I apply the analysis to mock data of perfect NFW haloes in an idealised observational scenario. Noise associated with the dispersion of the intrinsic ellipticities of source galaxies leads to a characteristic spatial dependence of the noise of the convergence estimator. I explain in detail how the measured Minkowski functionals are affected by noise and show how the signal may be recovered through segmentation of the excursion set. This proof of principle suggests that an NFW profile can be distinguished reliably from an isothermal model. I discuss how the simplifications under which lenses are studied here may affect results and suggest possible extensions.

The second topic of this dissertation is an extension of cosmological weak lensing measurements. Gravitational lensing by the large-scale structure (LSS hereafter) gives rise to the cosmic shear field, the statistics of which probe the matter power spectrum and its time evolution as well as spacetime geometry. A coherent shear signal across a field that does not feature known objects acting as lenses can be interpreted as a signature of weak lensing by the LSS (e.g. [Miralda-Escude, 1991](#); [Blandford et al., 1991](#); [Kaiser, 1992](#)). First detections were reported by [Schneider et al. \(1998\)](#); [Kaiser et al. \(2000\)](#); [Wittman et al. \(2000\)](#); [Van Waerbeke et al. \(2000\)](#); [Bacon et al. \(2000\)](#). The distortion of a galaxy image depends on the projected mass along the light path, and therefore varies with the direction of the line-of-sight, i.e. the position of the galaxy on the sky. If galaxy ellipticities are measured across large fields, spatial patterns can be analysed and statistics of the shear field extracted.

The sensitivity to cosmological parameters was highlighted by Villumsen (1996); Bernardeau et al. (1997); Kaiser (1998); van Waerbeke et al. (1999); Huterer (2002). In addition, the shear imprinted on a galaxy image depends on the distance of the source: the line-of-sight is longer for more remote galaxies, and the different geometric arrangement alters the lensing efficiency of foreground structures. If the shear is treated as a three-dimensional variable, it can constrain the distribution and growth of structures as well as the distance-redshift relation. Fully three-dimensional treatments were introduced by Heavens (2003) and further developed and applied by Castro et al. (2005); Heavens et al. (2006); Kitching et al. (2007, 2011); Ayaita et al. (2012); Kitching et al. (2014b). To exploit the full spatial dependence, however, adequate redshift measurements are required, which have only recently begun to be available. In absence of such data, only the statistics of the two-dimensional shear field are accessible (Jain & Seljak, 1997; Takada & Jain, 2002, 2003; Munshi & Kilbinger, 2006; Jee et al., 2013; Kilbinger et al., 2013). Observables are constructed from a projection of the lensing signal along the line-of-sight. In the course of this projection, however, information about the redshift evolution is inevitably lost. As a ‘compromise’, source galaxies may be assigned to bins according to their estimated redshifts. In each bin a conventional two-dimensional analysis can be carried out; the range of the projection, however, is much smaller, and the correlations between signals in different redshift bins put constraints on the time evolution. This stacking approach has been termed ‘tomography’ (Hu, 1999; Takada & White, 2004; Simon et al., 2004; Takada & Jain, 2004; Hollenstein et al., 2009; Kilbinger et al., 2009; Schäfer & Heisenberg, 2012; Heymans et al., 2013). Several authors have focused in particular on the potential of weak lensing to constrain dark energy (Jain & Taylor, 2003; Bernstein & Jain, 2004; Hannestad et al., 2006; Amendola et al., 2008; Huterer, 2010).

Most recently cross-correlations between the cosmic microwave background (CMB hereafter) and cosmic shear have come into focus. Like the light from distant galaxies, the CMB is deflected by the large-scale structure, leading to a remapping of the temperature distribution; in contrast to cosmic shear, only a single source plane (the surface of last scattering) is involved. Cross-correlations between two-dimensional cosmic shear maps and CMB lensing were measured for the first time by Hand et al. (2015). Troxel & Ishak (2014a) and Hall & Taylor (2014) investigated the influence of intrinsic alignments on this measurement. Kitching et al. (2014a) presented a formalism combining the three-dimensional galaxy ellipticity field and the CMB, considering the temperature, deflection and polarisation fields. They provided error forecasts for cosmological parameters based on the individual data sets and the combination. Expected constraints on the dark energy equation of state were shown to improve by 10–15 per cent when correlations between weak lensing of galaxies and the CMB deflection were considered.

In this dissertation I study cross-correlations between cosmic shear and the integrated Sachs-Wolfe effect (iSW hereafter). Photons crossing a time-evolving potential experience a net frequency shift, reflected in a small change of the CMB temperature. The effect vanishes in the linear regime of structure growth during matter domination, so that observations probe the relatively late times at which the dark energy contribution to the density becomes appreciable. This cosmological sensitivity was demonstrated by Vielva et al. (2006); Pietrobon et al. (2006); McEwen et al. (2007); Giannantonio et al. (2008); Ho et al. (2008); Giannantonio et al. (2014); Planck Collaboration (2015c). Like cosmic shear, the iSW effect traces potential wells projected along the line-of-sight, albeit with a different radial weight function, and therefore correlations between the two measurements are expected. I show how information from both effects can be combined in a single formalism, tying into the three-dimensional treatment of weak lensing. Using this approach I derive the full covariance encompassing the auto- and cross-correlations of cosmic shear modes and the iSW effect and develop an efficient implementation for the numerical calculation of the spectra.

Generally the feasibility of three-dimensional cosmic shear studies is severely limited by the large number of integrations required, in particular as many integrals have highly oscillatory kernels. This difficulty is exacerbated in a Fisher analysis, since the large covariance matrix must be calculated for many different parameter sets. Ayaita et al. (2012) developed a basis transformation for a more

efficient calculation of the covariance. I focus instead on the numerical integration itself and suggest a collocation method developed by [Levin \(1996, 1997\)](#). In order to illustrate the performance and numerical reliability of this implementation I carry out a Fisher analysis for two different lensing surveys and derive error forecasts for a cosmological model with seven parameters. I extend this implementation by the iSW auto- and cross-correlations and study how the parameter constraints improve due to the additional information.

A brief summary of the cosmological model and the theory underlying gravitational lensing is given in Chs. 2 and 3. The description of the matter distribution is established in Ch. 4. In Ch. 5, I define the density estimator for cluster lenses. The morphological analysis using Minkowski functionals is presented in Ch. 6. Chapter 7 is devoted to cosmic shear and its correlation with the integrated Sachs-Wolfe effect. In Ch. 8 I recapitulate the major findings of this dissertation.

# 2 Chapter 2

## Cosmology

Since the publication of Einstein’s general theory of relativity a century ago, cosmology has developed into a major discipline of physics, and the  $\Lambda$ CDM model is so firmly established that it is frequently called the ‘standard model’ of cosmology, in analogy to particle physics. None the less, the nature of major components is far from understood. It has long been observed that the Universe is expanding, and more recently it was determined that it does so at an increasing rate (Riess et al., 1998; Perlmutter et al., 1999). *Baryons* contribute only five per cent to the energy budget, while a non-relativistic collisionless fluid known as *cold dark matter* adds about 25 per cent; the energy density of *radiation* is negligible today. The remaining 70 per cent are attributed to the *cosmological constant*  $\Lambda$  or alternatively to *dark energy*. In the  $\Lambda$ CDM framework, space is flat. In this chapter I give a brief summary of the theoretical foundations of the cosmological model. For a comprehensive treatment, textbooks such as Peacock (2003) and Mukhanov (2005) or the review by Bartelmann (2010a) may be consulted.

### 2.1. The Friedmann-Lemaître-Robertson-Walker Universe

A profound assumption adopted by many cosmological models, including the  $\Lambda$ CDM model, is the *cosmological principle*. It states that the Universe should appear isotropic, and that it should appear so for any observer regardless of their position. This demand can be rephrased into the statement that the observable Universe should be *isotropic* and *homogeneous*. While isotropy is evidently broken by the existence of astrophysical objects, the assumption is supported when the statistics of observables are considered on scales much larger than the typical size and separation of such objects. The case for the *Copernican principle* – the assumption that our position in the Universe is by no means unique – is arguably more complex.

#### 2.1.1. The Robertson-Walker metric

In general relativity (Einstein, 1915), spacetime is described as a four-dimensional pseudo-Riemannian manifold characterised by the line element

$$ds^2 = g_{\mu\nu}dx^\mu dx^\nu. \quad (2.1)$$

$g_{\mu\nu}$  is the metric tensor. If the cosmological principle holds, the line element has the form (Robertson, 1935; Walker, 1935)

$$ds^2 = -c^2 dt^2 + a^2(t) \left[ d\chi^2 + f_K^2(\chi) (d\theta^2 + \sin^2 \theta d\phi^2) \right]. \quad (2.2)$$

The term in square brackets is the line element of the three-dimensional spatial hypersurfaces, the curvature of which may be positive, negative or vanishing as indicated by the parameter  $K$ :

$$f_K(\chi) = \begin{cases} |K|^{-1/2} \sinh|K|^{1/2}\chi & \text{if } K < 0 \\ \chi & \text{if } K = 0 \\ K^{-1/2} \sin K^{1/2}\chi & \text{if } K > 0 \end{cases} \quad (2.3)$$

$K < 0$  describes an open,  $K > 0$  a closed geometry. For  $K = 0$  space is Euclidean. The expansion of the spatial hypersurfaces with coordinate time  $t$  is quantified by the *scale factor*  $a(t)$ , normalised to  $a = 1$  at the present epoch. The assumption of isotropy can only hold for a *fundamental observer* following the mean cosmic motion, i.e. an observer whose position is constant with respect to the comoving coordinate grid  $(\chi, \theta, \phi)$  of the spatial hypersurfaces.

Einstein's *field equations* link the geometry of spacetime to its matter and energy content:

$$R_{\mu\nu} - \frac{R}{2}g_{\mu\nu} - \Lambda g_{\mu\nu} = \frac{8\pi G}{c^4}T_{\mu\nu}. \quad (2.4)$$

$R_{\mu\nu}$  is the Ricci tensor, depending on derivatives of the metric tensor up to second order; its trace is the Ricci scalar  $R$ .  $T_{\mu\nu}$  is the energy-momentum tensor, and its prefactor is set by the requirement that the field equations should reduce to Newtonian gravity in the limit of weak gravitational fields and non-relativistic motion. Lovelock's theorem (Lovelock, 1971, 1972) states that in a four-dimensional metric theory of gravity these are the most general field equations featuring partial derivatives of the metric up to second order (provided that the energy-momentum tensor is divergence-free, implying local energy conservation). The *cosmological constant*  $\Lambda$  can thus be interpreted as a geometric quantity; the physical motivation for its appearance is poor (see Sec. 2.2).

### 2.1.2. The Friedmann equations

For the Robertson-Walker line element given in Eq. (2.2) the field equations determine the dynamics of the scale factor  $a(t)$ . In homogeneous and isotropic spacetime, the energy-momentum tensor is that of a perfect fluid:

$$T_{\mu\nu} = \left(\rho + \frac{p}{c^2}\right)u_\mu u_\nu + p g_{\mu\nu}. \quad (2.5)$$

$\rho(t)$  and  $p(t)$  are the time-evolving density and pressure of the fluid; isotropy does not permit any spatial dependence.  $u^\mu = (c, 0, 0, 0)^T$  is the four-velocity of a fundamental observer, i.e. an observer for whom the spatial hypersurfaces appear isotropic. In this case the field equations (2.4) lead to the two *Friedmann equations* (Friedmann, 1922, 1924):

$$\left(\frac{\dot{a}}{a}\right)^2 = \frac{8\pi G}{3}\rho - \frac{Kc^2}{a^2} + \frac{\Lambda}{3}; \quad (2.6)$$

$$\frac{\ddot{a}}{a} = -\frac{4\pi G}{3}\left(\rho + \frac{3p}{c^2}\right) + \frac{\Lambda}{3}. \quad (2.7)$$

The expansion rate  $\dot{a}/a = H(a)$  is the *Hubble function*. Equations (2.6) and (2.7) can be combined to the *adiabatic equation*:

$$d(\rho c^2 a^3) + p da^3 = 0. \quad (2.8)$$

If a fluid is characterised by an *equation of state* of the form  $p = w\rho c^2$ , the evolution of the density can be obtained by integrating Eq. (2.8):

$$\rho(a) = \rho_0 \exp\left[-3 \int_1^a da' \frac{1+w(a')}{a'}\right] \quad (2.9)$$

or more specifically

$$\rho(a) = \rho_0 a^{-3(1+w)} \quad (2.10)$$

if  $w$  is constant.  $\rho_0$  is the density at  $a = 1$ .

Matter in the Universe can be classified as either ‘dust’, i.e. non-relativistic matter (which may be baryonic or dark), or ‘radiation’, encompassing photons and relativistic matter. In the case of dust, pressure is negligible, so that  $w = 0$  and

$$\rho(a) \sim a^{-3}, \quad (2.11)$$

which is the familiar scaling of the density with the cube of the diameter. The radiation density decreases with the fourth power of the scale factor,

$$\rho(a) \sim a^{-4} \quad (2.12)$$

( $w = 1/3$ ), reflecting the additional loss of energy due to redshift (see Sec. 2.1.3). Equation (2.6) suggests that formally curvature influences the expansion like a perfect fluid with the density  $\rho = -3Kc^2/8\pi Ga^2$  and therefore  $w = -1/3$ , while the cosmological constant is equivalent to the constant density  $\rho = \Lambda/8\pi G$  ( $w = -1$ ). Then for each component of the cosmic fluid a dimensionless *density parameter* can be defined as

$$\Omega_i(a) = \frac{8\pi G\rho_i(a)}{3H^2(a)} = \frac{\rho_i(a)}{\rho_{\text{cr}}(a)}, \quad (2.13)$$

where the subscript  $i \in \{r, m, b, \Lambda, K\}$  stands for radiation, total (non-relativistic) matter, baryonic matter, the cosmological constant or curvature. It follows from Eq. (2.6) that

$$1 = \Omega_r(a) + \Omega_m(a) + \Omega_\Lambda(a) + \Omega_K(a), \quad (2.14)$$

from which the meaning of the critical density  $\rho_{\text{cr}}(a)$  becomes clear: if the total energy density of radiation and matter plus the contribution of the cosmological constant is equal to the critical density, the Universe is spatially flat ( $K = 0$ ).

Denoting by subscript 0 the values of the Hubble rate and the density parameters today, the expansion rate can be parametrised as

$$\begin{aligned} H(a) &= H_0 \sqrt{\Omega_{r0}a^{-4} + \Omega_{m0}a^{-3} + \Omega_{\Lambda0} + (1 - \Omega_{r0} - \Omega_{m0} - \Omega_{\Lambda0})a^{-2}} \\ &= H_0 E(a). \end{aligned} \quad (2.15)$$

$H_0$ , the present value of the Hubble function, is called the *Hubble constant* and often expressed in terms of the dimensionless parameter  $h$ :

$$H_0 = 100 h \frac{\text{km}}{\text{s Mpc}}, \quad (2.16)$$

with  $h = 0.67$  the most recently measured value (Planck Collaboration, 2015b). The peculiar choice of units reflects the role of the parameter as the proportionality constant between the recession velocity of a source (measured in  $\text{km s}^{-1}$ ) and its distance (measured in Mpc).

Since the scaling of the density with the scale factor obeys a different power law for each energy form, the relative contributions to the overall energy density vary. As the radiation density drops fastest, the Universe is radiation-dominated in its earliest stage, followed by an era of matter domination (as both densities are in fact finite). *Matter-radiation equality*,  $\rho_m(a) = \rho_r(a)$ , occurs at

$$a_{\text{eq}} = \frac{\Omega_{r0}}{\Omega_{m0}}. \quad (2.17)$$

At later times curvature may take over, if the Universe is not spatially flat, and finally the cosmological constant.

The second Friedmann equation, Eq. (2.7), implies that matter and radiation slow down the expansion, whereas a cosmological constant accelerates it. As curvature behaves like a fluid with  $w = -1/3$ , it does not appear in the acceleration equation. While the recession of distant galaxies was already observed early in the 20th century (Slipher, 1917; Hubble, 1929; Hubble & Humason, 1931; Hubble, 1936), the acceleration was discovered by Riess et al. (1998) and Perlmutter et al. (1999) through measurements of the luminosity distances and redshifts of supernovae.

### 2.1.3. Redshift and distance measures

In an expanding universe, the wavelength of a photon grows as it travels from its source to an observer, so that the wavelength  $\lambda_o$  measured at the coordinate time  $t_o$  is larger than the wavelength  $\lambda_e$  upon emission at  $t_e$ . This effect is measured as the *cosmological redshift*

$$1 + z = \frac{\lambda_o}{\lambda_e} = \frac{a(t_o)}{a(t_e)}. \quad (2.18)$$

The cosmological redshift is a consequence of the Hubble flow, while motion with respect to the comoving coordinate grid leads to an additional Doppler shift.

The redshift  $z$  serves as a distance coordinate in cosmology, as it can be measured from the spectrum of a source. In dynamic, curved spacetime there is no unique way of defining a physical distance (with the dimension of a length). The two distance measures relevant for gravitational lensing are the *comoving distance* and the *angular diameter distance*.

The comoving distance  $\chi$  measures the distance between the world line of a source and a fundamental observer on a spatial hypersurface. Without loss of generality one can assume that the observer is located at the coordinate origin and observes a light ray propagating in the radial direction ( $d\theta = d\phi = 0$ ). As photon geodesics are characterised by  $ds = 0$ ,  $d\chi = -cdt/a = -cda/(\dot{a}a)$ , where the negative sign ensures that time grows towards the observer. Substituting Eq. (2.15) for the Hubble rate and transforming to a redshift integration, the comoving distance between two events at redshift  $z_1$  and  $z_2$  is given by

$$\chi(z_1, z_2) = \int_{a(z_2)}^{a(z_1)} \frac{c da}{a^2 H(a)} = \chi_H \int_{z_1}^{z_2} \frac{dz}{E(z)}. \quad (2.19)$$

In particular, the distance to a source at redshift  $z$  observed today is  $\chi(0, z)$ . In the limit  $z_2 \rightarrow \infty$ ,  $\chi(z_1, z_2)$  is the size of the *particle horizon* at redshift  $z_1$ , which is the radius of the comoving volume which is in causal contact with an observer at  $z_1$ , reflecting the finite speed of the propagation of information.  $\chi_H = c/H_0$  is the *Hubble radius* today. More generally, the *Hubble scale*  $c/H(a)$  is a characteristic scale for spacetime curvature.

The angular diameter distance creates an analogue to Euclidean geometry, where an object of the diameter  $\Delta l$  at the distance  $d$  subtends the angle  $\Delta\alpha = \Delta l/d$  (provided that the angle is small enough for the approximation  $\tan \Delta\alpha \approx \Delta\alpha$  to hold). Demanding that this relation should apply also to cosmological scales given an appropriate distance measure leads to the angular diameter distance

$$D_{\text{ang}}(z_1, z_2) = \frac{a(z_2)}{a(z_1)} f_K[\chi(z_1, z_2)] = \frac{1 + z_1}{1 + z_2} f_K[\chi(z_1, z_2)]. \quad (2.20)$$

## 2.2. The Case for Dark Energy

As mentioned in Sec. 2.1.1, Lovelock's theorem states that the most general field equation (under certain conditions) includes a cosmological constant. A finite value of  $\Lambda$  has the benefit of accounting for the accelerated expansion of the Universe, which cannot be explained by any form of matter in the standard model or even dark matter. Still the  $\Lambda$ CDM model has not gone unchallenged, with two aspects in particular the most frequently contested: interpreting the cosmological constant as the energy density of the vacuum, quantum field theories overestimate its value by about 120 orders

of magnitude (e.g. [Carroll, 2001](#)). This is a *fine-tuning problem*: if the cosmological constant is finite, why is it so much smaller than the Planck scale or indeed any fundamental energy scale? The second issue often perceived as a shortcoming is the *coincidence problem*: given the progression of dominating contributors to the energy budget, it seems fortuitous that the influence of the cosmological constant is in fact comparable to that of matter at the present time despite the rapid transition.

Attempts have been made to formulate field equations without a cosmological constant, broadly divided into two classes. *Dark energy* models stay within the framework of general relativity, but substitute a fluid with a dynamic equation of state for  $\Lambda$  in the cosmological model. The second group are *modified theories of gravity*, in which the left-hand side of the field equations (Eq. 2.4) is altered, so that a different link between geometry and energy content is constructed. Modified gravity scenarios can usually be mapped to dark energy models by adjustments to the energy-momentum-tensor. For reviews of the variety of theories, see e.g. [Straumann \(2006\)](#); [Frieman et al. \(2008\)](#); [Amendola & Tsujikawa \(2010\)](#).

Dark energy approaches offer a physical motivation for the accelerated expansion, rather than the geometric interpretation of the cosmological constant. According to Eq. (2.7), the equation of state of a fluid must be  $w < -1/3$  for  $\ddot{a} > 0$ . One solution is a homogeneous scalar field  $\phi$  with a self-interaction potential  $V(\phi)$ , known as ‘quintessence’ ([Peebles & Ratra, 1988](#); [Ratra & Peebles, 1988](#); [Wetterich, 1988](#); [Coble et al., 1997](#); [Turner & White, 1997](#)). Deriving the energy-momentum tensor from its Lagrangian and identifying the density and pressure from the components, one finds

$$w = \frac{p}{\rho c^2} = \frac{\frac{1}{2}\dot{\phi}^2 - V(\phi)}{\frac{1}{2}\dot{\phi}^2 + V(\phi)}. \quad (2.21)$$

Evidently  $w \gtrsim -1$  is negative as long as  $V(\phi) \gg \dot{\phi}^2/2$ . The equation of state is time-dependent, with  $w$  increasing as the field gains kinetic energy.

A multitude of realisations of dark energy have been developed. Current data are not sufficient to single out a preferred model. A link between observations and theories is, however, established through the phenomenological parametrisation suggested by [Chevallier & Polarski \(2001\)](#) and [Linder \(2003\)](#):

$$w(a) = w_0 + w_a(1 - a). \quad (2.22)$$

The evolution of the equation of state is described well by this form for a large variety of models; the cosmological constant is reproduced for  $w_0 = -1$  and  $w_a = 0$ . Many cosmological data sets can put constraints on the two parameters  $w_0$  and  $w_a$  and thus probe the dynamics of the equation of state.



# 3

## Chapter 3

# Gravitational Lensing

Gravitational lensing can be observed over a wide range of masses, from microlensing by planets to strong lensing by galaxy clusters and cosmological weak lensing by the large-scale structure. Light propagation in curved spacetime can be treated in general relativity in the approximation of geometric optics. In most situations the inhomogeneities giving rise to the deflection can be characterised by their Newtonian gravitational potential. Individual objects are typically thin lenses and are described by their projected surface mass distribution.

Applications range from the discovery of exoplanets to studies of the dark matter distribution on various scales and tests of cosmological models. Many reviews provide a comprehensive overview of both the theoretical foundations and the observational status, for example [Narayan & Bartelmann \(1996\)](#); [Bartelmann & Schneider \(2001\)](#); [Hoekstra et al. \(2002\)](#); [Bartelmann \(2010b\)](#); [Kneib & Narayan \(2011\)](#).

## 3.1. Light Deflection and Image Distortion

In the following I show how the general-relativistic treatment of light deflection leads to the lens equation. I introduce the fields characterising gravitational lenses and their effect on image shapes: the lensing potential; the deflection angle; the convergence, shear and reduced shear; and the magnification.

The presentation below draws heavily on the excellent reviews by [Bartelmann & Schneider \(2001\)](#) and [Bartelmann \(2010b\)](#), where much more rigorous derivations are given.

### 3.1.1. Light propagation in perturbed spacetime

The propagation of a light bundle in arbitrary spacetimes is governed by the *equation of geodesic deviation*, or Jacobi equation, which links the deformation of the cross-section of the bundle to the *optical tidal matrix*, quantifying spacetime curvature. In the following I consider homogeneous and isotropic spacetime described by a Friedmann-Lemaître-Robertson-Walker metric (see Sec. 2.1) with ‘small’ perturbations for which the following assumptions hold: the gravitational potential of the inhomogeneities is small,  $\Phi \ll c^2$ ; peculiar velocities are small,  $v \ll c$ ; and inhomogeneities are localised, i.e.  $\Phi$  varies on a scale that is small compared to the Hubble scale. Then the local neighbourhood of inhomogeneities can be approximated as flat space and the perturbed metric has the form

$$ds^2 = a^2(\eta) \left\{ - \left( 1 + \frac{2\Phi}{c^2} \right) c^2 d\eta^2 + \left( 1 - \frac{2\Phi}{c^2} \right) [d\chi^2 + \chi^2 (d\theta^2 + \sin^2 \theta d\phi^2)] \right\}, \quad (3.1)$$

where  $\eta$  is the conformal time, related to coordinate time  $t$  by  $d\eta = dt/a$ .

The optical tidal matrix can then be split up into two contributions, from the homogeneous and isotropic background on the one hand and inhomogeneities on the other. The Jacobi equation can be

brought into the following form (Bartelmann, 2010b):

$$\left(\frac{d^2}{d\chi^2} + K\right)x^i = -\frac{2}{c^2}\partial^i\Phi. \quad (3.2)$$

$(x^1, x^2)^T$  is the comoving separation between a fiducial ray in the light bundle and a closely neighbouring ray, measured perpendicular to the tangent vector to the fiducial ray;  $\chi$  is the comoving distance from the observer measured along the fiducial ray;  $K$  is the spatial curvature of the background. The derivative  $\partial^i\Phi$  is the transverse gradient of the gravitational potential, perpendicular to the fiducial ray. If the two rays enclose an angle  $(\theta^1, \theta^2)^T$  at the observer, the boundary conditions are

$$x^i\Big|_{\chi=0} = 0, \quad \frac{dx^i}{d\chi}\Big|_{\chi=0} = \theta^i. \quad (3.3)$$

Equation (3.2) is then solved by

$$x^i(\chi) = f_K(\chi)\theta^i - \frac{2}{c^2} \int_0^\chi d\chi' f_K(\chi - \chi')\partial^i\Phi[x^j(\chi'), \chi']. \quad (3.4)$$

In the *Born approximation* the integration is carried out along the unperturbed path with  $x^j(\chi') \approx f_K(\chi')\theta^j$ . Denoting by  $\chi_s$  the comoving distance to the light source and transforming from the comoving separation  $x^i$  to the angle  $\beta^i = x^i(\chi_s)/f_K(\chi_s)$ , one finds

$$\beta^i = \theta^i - \frac{2}{c^2} \int_0^{\chi_s} d\chi' \frac{f_K(\chi_s - \chi')}{f_K(\chi_s)} \partial^i\Phi[f_K(\chi')\theta^j, \chi']. \quad (3.5)$$

### 3.1.2. The lens mapping

Equation (3.5) is the *lens equation*

$$\beta^i = \theta^i - \alpha^i(\theta^j), \quad (3.6)$$

where

$$\alpha^i(\theta^j) = \frac{2}{c^2} \int_0^{\chi_s} d\chi' \frac{f_K(\chi_s - \chi')}{f_K(\chi_s)} \partial^i\Phi[f_K(\chi')\theta^j, \chi'] \quad (3.7)$$

is the *reduced deflection angle*, which can be written as the transverse gradient of the *lensing potential*

$$\phi(\theta^j) = \frac{2}{c^2} \int_0^{\chi_s} d\chi' \frac{f_K(\chi_s - \chi')}{f_K(\chi_s)f_K(\chi')} \Phi[f_K(\chi')\theta^j, \chi']. \quad (3.8)$$

Note that ‘gradient’ here refers to the derivative with respect to angular coordinates:

$$\alpha^i(\theta^j) = \frac{\partial}{\partial\theta^i}\phi(\theta^j), \quad (3.9)$$

hence the additional factor of  $f_K^{-1}(\chi')$  in the integrand.

The deflection angle  $\alpha^i$  cannot be observed because the true position of a source is not normally known. If, however,  $\alpha^i$  varies across the extent of a source, it will appear deformed. The linear variation is described by the Jacobian of the lens mapping (3.6):

$$A = \left(\frac{\partial\beta^i}{\partial\theta^j}\right) = \begin{pmatrix} 1 - \kappa & 0 \\ 0 & 1 - \kappa \end{pmatrix} - \begin{pmatrix} \gamma_+ & \gamma_\times \\ \gamma_\times & -\gamma_+ \end{pmatrix} = (1 - \kappa) \begin{pmatrix} 1 - g_+ & -g_\times \\ -g_\times & 1 + g_+ \end{pmatrix}. \quad (3.10)$$

Here  $A$  has been split up into a diagonal part proportional to the trace and a trace-free part.

In this linear approximation a circle is mapped onto an ellipse. The *convergence*  $\kappa$  quantifies the isotropic dilation of the image, while the components of the *shear tensor*  $\gamma$  describe its elongation. The inverse of the determinant of the Jacobian is the *magnification*

$$\mu = (\det A)^{-1} = [(1 - \kappa)^2 - \gamma_+^2 - \gamma_\times^2]^{-1}. \quad (3.11)$$

Convergence and shear can be expressed in terms of the lensing potential:

$$\kappa = \frac{1}{2} \left( \frac{\partial^2 \phi}{\partial(\theta^1)^2} + \frac{\partial^2 \phi}{\partial(\theta^2)^2} \right), \quad (3.12)$$

$$\gamma_+ = \frac{1}{2} \left( \frac{\partial^2 \phi}{\partial(\theta^1)^2} - \frac{\partial^2 \phi}{\partial(\theta^2)^2} \right), \quad (3.13)$$

$$\gamma_\times = \frac{\partial^2 \phi}{\partial\theta^1 \partial\theta^2}. \quad (3.14)$$

The derivation above has made use of the *flat-sky approximation*, measuring separations in Cartesian coordinates  $(\theta^1, \theta^2)$ . On scales on which the curvature of the celestial sphere becomes important, a suitable basis must be defined and derivatives are expressed in terms of the  $\delta$  operator (Newman & Penrose, 1966) and its complex conjugate  $\bar{\delta}$ :

$$\kappa = \frac{1}{2} \bar{\delta} \delta \phi, \quad \gamma = \gamma_+ + i\gamma_\times = \frac{1}{2} \delta \bar{\delta} \phi. \quad (3.15)$$

Here the complex shear  $\gamma$  has been introduced. In the flat-sky approximation,

$$\delta = \frac{\partial}{\partial\theta^1} + i \frac{\partial}{\partial\theta^2}, \quad (3.16)$$

where I have reverted back to Cartesian coordinates.

The convergence  $\kappa$  is closely related to the mass density  $\rho$ : taking the appropriate derivative of the lensing potential given in Eq. (3.8),

$$\kappa(\theta^j) = \frac{1}{c^2} \int_0^{\chi_s} d\chi' \frac{f_K(\chi_s - \chi')}{f_K(\chi_s) f_K(\chi')} \frac{\partial^2 \Phi}{\partial\theta_i \partial\theta^i} [f_K(\chi') \theta^j, \chi']. \quad (3.17)$$

*Poisson's equation* states that

$$\partial^i \partial_i \Phi = \Delta_\perp \Phi + \Delta_\parallel \Phi = 4\pi G \rho, \quad (3.18)$$

where the Laplacian has been split up into a transverse part and the derivative along the light path. The latter averages out in the line-of-sight integration (White & Hu, 2000), so that the derivative perpendicular to the light path

$$\Delta_\perp \Phi = f_K^{-2}(\chi') \frac{\partial^2 \Phi}{\partial\theta_i \partial\theta^i} \quad (3.19)$$

can safely be replaced by the three-dimensional Laplacian. Then

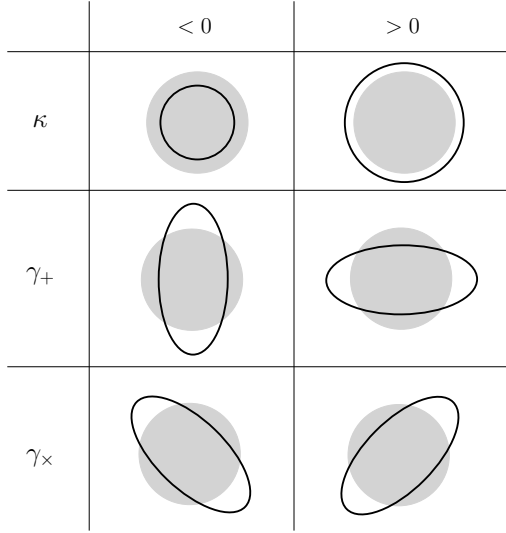
$$\kappa(\theta^j) = \frac{4\pi G}{c^2} \int_0^{\chi_s} d\chi' \frac{f_K(\chi_s - \chi') f_K(\chi')}{f_K(\chi_s)} \rho [f_K(\chi') \theta^j, \chi'], \quad (3.20)$$

i.e. the convergence is a weighted projection of the density, integrated along the unperturbed light path.

The shear tensor parametrises the elliptical distortion of an image. Writing the complex shear as  $\gamma = |\gamma| e^{2i\varphi}$ , the angle  $\varphi$  is the position angle of the elliptical image of a circle. The shear tensor is invariant under rotations of  $\pi$  and therefore has spin 2, which is intuitive, since an ellipse is mapped onto itself under such rotations. The meaning of the two components  $\gamma_+$  and  $\gamma_\times$  is illustrated in Fig. 3.1.

From the last equality in Eq. (3.10) it can be seen that the shape of an image is affected only by the *reduced shear*

$$g = \frac{\gamma}{1 - \kappa}. \quad (3.21)$$



The shear  $\gamma$  itself cannot be observed: lacking knowledge of the source size, only the distortion of the image is accessible. The invariance of observables under the rescaling  $A \rightarrow \lambda A$  is known as the *mass sheet degeneracy* (Falco et al., 1985): observations are reproduced by any mass distribution with the convergence  $\lambda\kappa + 1 - \lambda$ , which corresponds to the addition of a constant small projected surface mass density if  $\lambda$  is close to 1.

Anisotropic distortions are not limited to ellipticity, but higher derivatives are needed to quantify them. The next order, for example, leads to various types of *flexion* (e.g. Goldberg & Bacon, 2005; Bacon et al., 2006).

**Figure 3.1.:** Illustration of the distortion induced by the convergence  $\kappa$  and the components of the shear,  $\gamma_+$  and  $\gamma_\times$ . The grey circle represents the source, black contours indicate the deformed shape.

## 3.2. Lensing by Individual Objects

Certain simplifications to the above treatment can be made if a single astrophysical object gives rise to the light deflection. A light ray can be assumed to propagate along an unperturbed path from the source to the lens and from the lens to the observer, with the deflection represented by a discrete change of direction at the location of the lens, which is characterised by its two-dimensional projected surface mass density. Below I describe the lens mapping in this approximation and give the conditions under which strong lensing phenomena may be observed.

### 3.2.1. The thin lens approximation

Astrophysical objects acting as gravitational lenses are typically thin compared to the separations between the object, the source and the observer. Then the mass distribution can be projected onto the *lens plane* at the comoving distance  $\chi_d$ . With the substitution

$$\Phi[f_K(\chi')\theta^j, \chi'] \rightarrow \delta_D(\chi' - \chi_d) \int d\chi \Phi[f_K(\chi)\theta^j, \chi] \quad (3.22)$$

the lensing potential becomes

$$\phi(\theta^j) = \frac{2}{c^2} \frac{f_K(\chi_s - \chi_d)}{f_K(\chi_s)f_K(\chi_d)} \int d\chi' \Phi[f_K(\chi')\theta^j, \chi']. \quad (3.23)$$

The convergence is the scaled surface mass density

$$\kappa(\theta^j) = \frac{\Sigma(\theta^j)}{\Sigma_{\text{cr}}}, \quad (3.24)$$

where the projected surface mass density of the lens is given by

$$\Sigma(\theta^j) = \int d\chi' \rho[f_K(\chi')\theta^j, \chi'] \quad (3.25)$$

and

$$\Sigma_{\text{cr}} = \frac{c^2}{4\pi G} \frac{f_K(\chi_s)}{f_K(\chi_s - \chi_d)f_K(\chi_d)} \quad (3.26)$$

is the *critical surface mass density*, which depends on the distances between source, lens and observer.

### 3.2.2. Strong and weak lensing

Points in the lens plane where the lens mapping defined in Eq. (3.6) is singular,  $\det A = 0$ , form the *critical lines*; the corresponding source positions are the *caustics*. Images near the critical lines are highly magnified and distorted, and sources inside caustics appear as multiple images. These phenomena are collectively known as *strong lensing*. Far away from the critical lines, only *weak lensing* is observed, giving rise to small image distortions.

For axisymmetric lenses, light can only be deflected along the radial direction, i.e. towards the lens centre; similarly the shear must be tangential or radial. Denoting by  $\theta$  the angular radius measured from the lens centre and by  $\alpha$  the modulus of the deflection angle, it can be shown that

$$\alpha(\theta) = \frac{m(\theta)}{\theta}, \quad (3.27)$$

where

$$m(\theta) = 2 \int_0^\theta d\theta' \theta' \kappa(\theta') \quad (3.28)$$

is the scaled mass enclosed within the radius  $\theta$ . The determinant of the lens mapping can be written as

$$\det A(\theta) = \mu^{-1}(\theta) = \left[ 1 - \frac{m(\theta)}{\theta^2} \right] \left[ 1 - \frac{d}{d\theta} \frac{m(\theta)}{\theta} \right]. \quad (3.29)$$

The mapping is singular if the determinant vanishes, thus if

$$m(\theta) = \theta^2 \quad (3.30)$$

or

$$\frac{d}{d\theta} \frac{m(\theta)}{\theta} = 1. \quad (3.31)$$

Critical lines fulfilling the condition (3.30) or (3.31) are called *tangential* and *radial*, respectively, signifying the preferred direction of the lensing-induced distortion near these lines. Giant luminous arcs trace the tangential critical line, forming an ‘Einstein ring’ in the most spectacular cases; its radius is the *Einstein radius*. Note that Eq. (3.30) implies that the mean convergence inside the tangential critical line is unity. Thus super-critical lenses, for which  $\Sigma > \Sigma_{\text{cr}}$  somewhere, have tangential critical lines and are capable of producing multiple images (depending on the source position); note, however, that this is a sufficient, but not a necessary condition.



# 4

## Chapter 4

---

# Structure Formation and Properties of Dark Matter Haloes

In the widely accepted paradigm of *inflation* (Liddle, 1999; Langlois, 2010) the matter distribution observed today is viewed as the result of the gravitational instability of small fluctuations in the primordial density field, seeded by the quantum fluctuations of a scalar field. This ‘inflaton’ field leads to an early epoch of accelerated expansion (cf. Sec. 2.2), which can solve the *flatness problem*, explaining the vanishing spatial curvature, and the *causality problem* associated with the isotropy of the cosmic microwave background on scales larger than the particle horizon at the time of recombination. Its vacuum fluctuations are driven outside the horizon during the rapid expansion and translate into Gaussian perturbations of the gravitational potential and consequently the density. As long as overdensities are small, statistical homogeneity is preserved; in the linear theory the evolution of the density can be treated analytically using equations supplied by Newtonian fluid mechanics. Remarkably, dark matter fluctuations are amplified before the baryonic component, since the latter is coupled to the photons and radiation pressure prevents growth. Structure formation is hierarchical, with smaller objects assembling first and merging to form increasingly large structures.

In this chapter I provide an outline of the evolution of the density field in the linear regime and the description of its statistics through the power spectrum. As the cosmic microwave background is the most important probe of this spectrum, I give a brief overview of its origin and features. I summarise the most important properties of dark matter haloes in the spherical collapse model as well as numerical simulations to demonstrate the role of characteristic scales in density profiles. The theory of structure formation and CMB physics are covered in the textbooks by Dodelson (2003), Peacock (2003) and Mukhanov (2005).

## 4.1. The Growth of Density Fluctuations

On scales much smaller than those on which spacetime curvature becomes important, gravitational instability can be treated in the Newtonian framework. As the matter budget of the Universe is dominated by cold dark matter, the focus is on a collisionless, self-gravitating medium in a homogeneous and isotropic background expanding at the Hubble rate.

### 4.1.1. Gravitational instability of collisionless dark matter

Since the collision term in the Boltzmann equation vanishes in the case of collisionless dark matter, the equations governing the evolution of the matter density  $\rho$ , the gravitational potential  $\Phi$  and the velocity field  $\mathbf{v}$  have the same shape as the hydrodynamical equations describing the conservation of mass and momentum and the self-gravity of a perfect fluid with negligible pressure:

- the continuity equation:

$$\frac{\partial \rho}{\partial t} + \nabla \cdot \rho \mathbf{v} = 0; \quad (4.1)$$

- the Euler equation:

$$\frac{d\mathbf{v}}{dt} = -\nabla\Phi; \quad (4.2)$$

- the Poisson equation:

$$\Delta\Phi = 4\pi G\rho. \quad (4.3)$$

The density field is described in terms of the *density contrast*

$$\delta(\mathbf{r}, t) = \frac{\rho(\mathbf{r}, t) - \rho_{\text{bg}}(t)}{\rho_{\text{bg}}(t)}, \quad (4.4)$$

where  $\rho_{\text{bg}}(t) = \Omega_{\text{bg}}(t)\rho_{\text{cr}}(t)$  is the matter density of the homogeneous and isotropic background. To deal with the expansion, it is useful to transform to Lagrangian (comoving) coordinates. Writing  $\mathbf{r} = a\mathbf{x}$ , the velocity is  $\mathbf{v} = \dot{\mathbf{r}} = \dot{a}\mathbf{x} + a\dot{\mathbf{x}} = H(a)\mathbf{r} + a\mathbf{u}$ , where  $\mathbf{u}$  is a small velocity perturbation on top of the Hubble flow, measured in comoving coordinates.

#### 4.1.2. Linear growth

As long as the overdensity is small,  $\delta \ll 1$ , the treatment can be restricted to the first order in the perturbations. The set of equations in comoving coordinates then reads:

$$\frac{\partial}{\partial t}\delta(\mathbf{x}, t) + \nabla \cdot \mathbf{u}(\mathbf{x}, t) = 0; \quad (4.5)$$

$$\frac{\partial}{\partial t}\mathbf{u}(\mathbf{x}, t) + 2H[a(t)]\mathbf{u}(\mathbf{x}, t) = -\frac{1}{a^2}\nabla\Phi(\mathbf{x}, t); \quad (4.6)$$

$$\frac{1}{a^2}\Delta\Phi(\mathbf{x}, t) = 4\pi G\rho_{\text{bg}}(t)\delta(\mathbf{x}, t). \quad (4.7)$$

These equations can be combined into a single differential equation for the density contrast (e.g. [Wang & Steinhardt, 1998](#); [Linder & Jenkins, 2003](#)):

$$\frac{\partial^2}{\partial a^2}\delta(\mathbf{x}, a) + \frac{1}{a}\left(3 + \frac{d \ln H}{d \ln a}\right)\frac{\partial}{\partial a}\delta(\mathbf{x}, a) = \frac{3\Omega_{\text{m}}(a)}{2a^2}\delta(\mathbf{x}, a). \quad (4.8)$$

The second term, proportional to  $\partial\delta/\partial a$ , acts as a friction term and is sometimes called the ‘Hubble drag’, since it reflects the Hubble expansion counteracting the gravitative attraction.

As temporal and spatial dependence decouple in the linear regime, the density factorises:

$$\delta(\mathbf{x}, a) = D_+(a)\delta(\mathbf{x}). \quad (4.9)$$

The function  $D_+(a)$  describing the evolution is called the *growth function* and represents the growing solution of Eq. (4.8). The second solution decays with increasing  $a$  and consequently cannot describe the amplification of density perturbations. The growth function is usually normalised to  $D_+(a = 1) = 1$ . In a matter-dominated universe ( $\Omega_{\text{m}} = 1$ ), the Hubble rate is  $H(a) \sim a^{-3/2}$  (cf. Eq. 2.15), so that  $D_+(a) = a$ .

If the fluid is not collisionless, the pressure gradient  $-\nabla p/\rho$  must be added to the right-hand side of the Euler equation. Fluctuations in the pressure are related to the density perturbations through the adiabatic sound speed  $c_s^2 = \partial p/\partial \rho$ . It can then be shown that pressure support prevents the collapse of overdense regions on scales below the *Jeans length*

$$\lambda_{\text{J}} = c_s \sqrt{\frac{\pi}{G\rho_{\text{bg}}}}. \quad (4.10)$$

During the radiation-dominated era, the scaling of the Hubble function is  $H(a) \sim a^{-2}$ . The Jeans length for photons and relativistic matter is of the order of the Hubble scale  $c/H$ , so that the growth of fluctuations in the radiation density is strongly suppressed. Although radiation pressure does not affect cold dark matter, the growth of perturbations in the dark component differs from the matter-dominated regime due to the expansion rate. Equation (4.8) can be reparametrised to the form (Mészáros, 1974)

$$D_+''(y) + \frac{2+3y}{2y(1+y)}D_+'(y) - \frac{3}{2y(1+y)}D_+(y) = 0 \quad (4.11)$$

with the solution

$$D_+(y) \sim y + \frac{2}{3}, \quad (4.12)$$

where  $y = a/a_{\text{eq}}$  is the scale factor in units of the value at matter-radiation equality (cf. Eq. 2.17). While  $D_+(a) \sim a$  in the matter-dominated Universe ( $y \gg 1$ ) is recovered, growth is extremely slow during radiation domination ( $y \ll 1$ ) due to the altered expansion rate.

### 4.1.3. The power spectrum

The most common descriptor of the density field is the *power spectrum*, which is the variance of the density contrast  $\delta$  in Fourier space:

$$\langle \delta(\mathbf{k})\delta(\mathbf{k}') \rangle = (2\pi)^3 P_\delta(k) \delta^{\text{D}}(\mathbf{k} - \mathbf{k}'). \quad (4.13)$$

Here the Fourier transform is defined as follows:

$$\delta(\mathbf{k}) = \int d^3x \delta(\mathbf{x}) e^{-i\mathbf{k}\cdot\mathbf{x}}, \quad \delta(\mathbf{x}) = \int \frac{d^3k}{(2\pi)^3} \delta(\mathbf{k}) e^{i\mathbf{k}\cdot\mathbf{x}}. \quad (4.14)$$

$P_\delta(k)$  cannot depend on the orientation of the wavevector  $\mathbf{k}$  due to isotropy; as long as the density field is statistically homogeneous, there is no coupling between different modes, which is expressed by the Dirac delta distribution in Eq. (4.13). The power spectrum is the Fourier transform of the two-point correlation function:

$$P_\delta(k) = \int d^3x \langle \delta(\mathbf{r})\delta(\mathbf{r} + \mathbf{x}) \rangle e^{-i\mathbf{k}\cdot\mathbf{x}}. \quad (4.15)$$

In principle,  $P_\delta(k)$  is a function of coordinate time, reflecting the evolution of the density field, and is sometimes expressed as a function of redshift, i.e.  $P_\delta(k, z)$ . Unless a second argument is explicitly given,  $P_\delta(k)$  refers to the power spectrum at the present epoch assuming linear growth of the initial perturbations. Note that statistical homogeneity is preserved in the linear regime, so that the redshift evolution changes the amplitude of the spectrum, but not its shape. Non-linear growth, in contrast, leads to mode coupling and moves power to smaller scales as structures collapse; therefore the redshift dependence in the non-linear regime is not trivial (cf. Fig. 4.1).

The shape of the primordial spectrum is determined by the mechanism of inflation (e.g. Liddle & Lyth, 2000). Most models predict Gaussian perturbations with a scale-invariant dimensionless power spectrum

$$k^3 P_\Phi(k) \sim k^{n_s - 1}, \quad (4.16)$$

where  $n_s \simeq 1$  is the *spectral index*. According to the Poisson equation (Eq. 4.7), the scaling between Fourier modes of the density contrast and the gravitational potential is  $\delta(\mathbf{k}) \sim k^2 \Phi(\mathbf{k})$ . The initial matter power spectrum then has the shape  $P_\delta(k) \sim k^4 P_\Phi(k) \sim k^{n_s}$ , which is the *Harrison-Zel'dovich-Peebles spectrum* (Harrison, 1970; Peebles & Yu, 1970; Zel'dovich, 1972). The suppression of growth during radiation-domination (see the previous section) has not yet been considered. This is accounted for by the introduction of the *transfer function*  $T(k)$ :

$$P_\delta(k) = T^2(k) k^{n_s}. \quad (4.17)$$

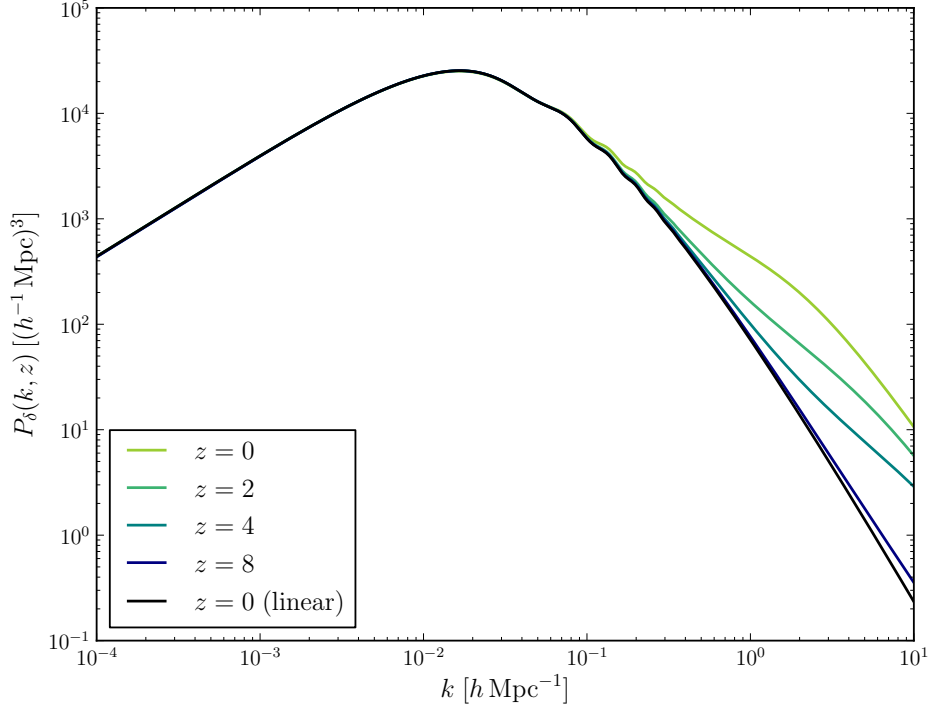


**Figure 4.1.:** Non-linear matter power spectrum  $P_\delta(k)$  at different redshifts  $z$ , and the linear power spectrum today. Spectra with  $z > 0$  have been scaled by  $D_+^{-2}[a(z)]$ .

The asymptotes of  $T(k)$  can easily be found. Let  $k_{\text{eq}}$  be the wavenumber corresponding to the Hubble scale at matter-radiation equality. The Mészáros mechanism affects only length scales smaller than the Hubble scale, and only in the radiation-dominated era. Super-horizon modes with  $k \ll k_{\text{eq}}$  experience no suppression, so that  $T(k) \simeq 1$ . On sub-horizon scales, however, the density does not evolve significantly until the end of the radiation-dominated era. As the dimensionless spectrum  $k^3 P_\delta(k)$  must then be nearly constant for  $k \gg k_{\text{eq}}$ ,  $T(k) \sim k^{-2}$  is implied. The exact form of the transfer function must take into account the transition between the radiation- and matter-dominated eras. An excellent fit was found by [Bardeen et al. \(1986\)](#):

$$T(q) = \frac{\ln(1 + 2.34q)}{2.34q} \left[ 1 + 3.89q + (16.1q)^2 + (5.46q)^3 + (6.71q)^4 \right]^{-1/4}, \quad q = \frac{k}{\Gamma h \text{ Mpc}^{-1}}. \quad (4.18)$$

$\Gamma$  is the *shape parameter*. For cold dark matter only [Bardeen et al. \(1986\)](#) gave  $\Gamma = \Omega_m h$ , but generally  $\Gamma$  is adjusted to account for the influence of baryons on the spectrum ([Sugiyama, 1995](#); [Eisenstein & Hu, 1998, 1999](#)).

In addition to the spectral index  $n_s$  and the transfer function, the amplitude of the power spectrum must be given. This is most commonly characterised by the parameter  $\sigma_8$ , which is the variance of the smoothed density field, i.e.  $\delta(\mathbf{x})$  convolved with a top hat filter of the radius  $R = 8 h^{-1} \text{ Mpc}$ :

$$\sigma_R^2 = \int \frac{k^2 dk}{2\pi^2} W^2(kR) P_\delta(k). \quad (4.19)$$

$W(x) = j_1(x)/x$  is the three-dimensional Fourier transform of the top hat filter;  $j_1(x)$  is the first spherical Bessel function.

Figure 4.1 shows the linearly evolved power spectrum today and the non-linear spectra at different redshifts, calculated using the COSMIC LINEAR ANISOTROPY SOLVING SYSTEM<sup>1</sup> (CLASS; [Blas et al., 2011](#)).

<sup>1</sup>[http://class\\_code.net](http://class_code.net)

The linear spectrum displays the asymptotic behaviour described above, with  $P_\delta(k) \sim k$  on large scales and  $P_\delta(k) \sim k^{-3}$  for the highest wavenumbers. The non-linear evolution increases the power on small scales. At  $z = 8$  only a small difference is seen, but discrepancies become significant as the non-linear growth progresses, affecting modes with  $k \gtrsim 0.1 h \text{ Mpc}^{-1}$  at  $z = 0$ .

## 4.2. The Cosmic Microwave Background

The cosmic microwave background is an important probe of the initial spectrum of perturbations, and a test of the cosmological model in general. The growth of fluctuations is homogeneous up to the release of the CMB radiation, so that the statistical structure is preserved. A number of physical effects, however, imprint characteristic signatures on the CMB spectrum. In the following I give a brief overview of the origin and properties of the CMB and the sources of these anisotropies. Comprehensive discussions can be found in [Seljak & Zaldarriaga \(1996\)](#); [Aghanim et al. \(2008\)](#); [Durrer \(2008\)](#). For measurements and detailed analyses of the data sets, see the results of the Wilkinson Microwave Anisotropy Probe (WMAP; [Bennett et al., 2013](#)) and the Planck mission ([Planck Collaboration, 2015a](#)).

### 4.2.1. Origin

In the early Universe, thermal equilibrium between nuclei, electrons and photons is maintained through Thomson scattering. In the course of the expansion, however, the plasma cools, until the temperature is low enough to permit the formation of neutral atoms. After *recombination*, photons and baryons decouple because thermal radiation is no longer absorbed, so that the photons emitted at recombination propagate (nearly) freely and are observed today as the microwave background.

As the radiation is released from a plasma in thermal equilibrium which is distributed homogeneously and isotropically according to the cosmological principle (see Sec. 2.1), its spectrum is a black-body spectrum with a single temperature  $T_{\text{rec}}$ . Note that the spectrum is Planckian despite the finite thickness of the recombination shell: radiation released towards the end of recombination is emitted from a cooler plasma, but this effect is cancelled out by the higher cosmological redshift of the photons emitted earlier. From the binding energy of hydrogen  $k_B T_{\text{rec}} \sim 13.6 \text{ eV}$  would be expected. Recombination is delayed, however, due to the high photon-to-baryon ratio, which is of the order of  $10^9$ . Using Saha's equation it can be shown that  $k_B T_{\text{rec}} \sim 0.3 \text{ eV}$ . Recombination then occurs at  $z_{\text{rec}} \sim 1100$ , placing the peak of the spectrum observed today in the microwave band, with a temperature of  $T_0 \sim 3 \text{ K}$ .

### 4.2.2. Primary anisotropies

The most pronounced structure in the observed temperature distribution of the CMB is a dipole, which is caused by the motion of the Earth relative to the rest frame of the radiation. As it does not probe physical effects on cosmological scales, it is normally subtracted.

*Primary anisotropies* are signatures of the energy density and physical effects on the surface of last scattering. The fluctuations principally reflect perturbations of the energy density at the time of decoupling. The imprint of these perturbations on the temperature pattern is marked by a number of features. The most important mechanism on large scales is the *Sachs-Wolfe effect* ([Sachs & Wolfe, 1967](#)): a photon escaping from a potential well  $\delta\Phi$  experiences a gravitational redshift. The perturbation of the metric associated with the potential fluctuation causes a time delay leading to a later emission and smaller cosmological redshift compared to the mean. Combining these two competing influences leaves a net temperature fluctuation of  $\Theta = \delta\Phi/(3c^2)$  (for the definition of the temperature contrast  $\Theta$  see Eq. 4.23 below).

On intermediate scales, *baryonic acoustic oscillations* can be observed. The mean free path of a photon is

$$\lambda = \frac{1}{n_e \sigma_T}, \quad (4.20)$$

where  $n_e$  is the number density of free electrons and  $\sigma_T$  the cross section for Thomson scattering. As long as  $\lambda$  is small, baryons and photons are tightly coupled and sound waves can propagate in the plasma, driven by the interplay between the gravitational pull of overdensities and pressure. The scale of these fluctuations is set by the *sound horizon* at the time of recombination,

$$\chi_s = \int_0^{t_{\text{rec}}} \frac{c dt}{3a \sqrt{1+R}}, \quad (4.21)$$

where  $R$  is the ratio of the momentum densities of photons and baryons. At decoupling the photon mean free path grows rapidly and oscillations cease due to the lack of pressure.

As the mean free path of the photons is finite, they can diffuse out of overdense regions, erasing fluctuations below the diffusion length

$$\lambda_D = \left( \int_0^{t_{\text{rec}}} \frac{c dt}{\lambda} \right)^{1/2} \lambda. \quad (4.22)$$

This process is called *Silk damping* (Silk, 1968).

It should be noted that anisotropies of the CMB are not limited to the temperature distribution. The differential cross section for Thomson scattering depends on the polarisation of the incoming radiation. Due to the inhomogeneities in the energy density, the infalling field is not isotropic, resulting in a linear polarisation of the scattered radiation.

### 4.2.3. Power spectrum

To study temperature fluctuations of the CMB as a function of direction  $\hat{\mathbf{n}}$ , one defines the dimensionless temperature contrast

$$\Theta(\hat{\mathbf{n}}) = \frac{T(\hat{\mathbf{n}}) - T_0}{T_0}. \quad (4.23)$$

Fluctuations are of the order of  $10^{-5}$ , in accordance with structure formation scenarios involving baryons and cold dark matter; note that higher fluctuations around  $10^{-3}$  would be expected for purely baryonic matter. The temperature contrast can be expanded in spherical harmonics:

$$\Theta(\hat{\mathbf{n}}) = \sum_{\ell, m} \Theta_{\ell m} Y_{\ell m}(\hat{\mathbf{n}}), \quad \Theta_{\ell m} = \int d\Omega \Theta(\hat{\mathbf{n}}) Y_{\ell m}^*(\hat{\mathbf{n}}), \quad (4.24)$$

leading to the power spectrum

$$\langle \Theta_{\ell m} \Theta_{\ell' m'}^* \rangle = C_\ell^{\Theta\Theta} \delta_{\ell\ell'}^K \delta_{mm'}^K, \quad (4.25)$$

where  $\delta_K$  denotes the Kronecker delta. Again statistical homogeneity and isotropy dictate that  $C_\ell^{\Theta\Theta}$  may only depend on the multipole order  $\ell$  and that there is no mode coupling. Note that the ensemble average in Eq. (4.25) cannot be calculated from a single measurement, so that the power spectrum must be estimated by

$$\hat{C}_\ell^{\Theta\Theta} = \sum_{m=-\ell}^{\ell} \frac{|\Theta_{\ell m}|^2}{2\ell + 1}. \quad (4.26)$$

The law of large numbers then dictates that the statistical uncertainty is proportional to  $(2\ell + 1)^{-1/2}$ . This *cosmic variance* decays with growing multipole order due to the increasing multiplicity.

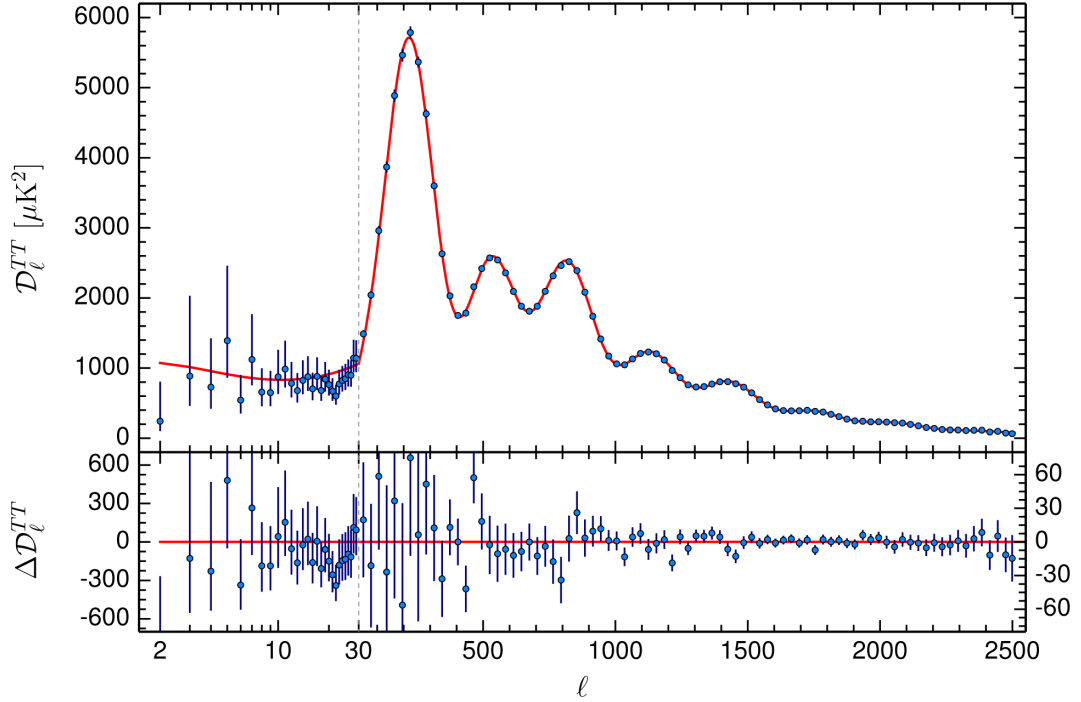


**Figure 4.2.:** Angular power spectrum of the CMB temperature, from the [Planck Collaboration \(2015b\)](#). Error bars on the data points correspond to  $1\text{-}\sigma$  uncertainties. The solid line indicates the prediction of the best-fitting  $\Lambda$ CDM model; residuals are shown in the lower panel.

Figure 4.2 shows the angular power spectrum measured by the Planck mission. The quantity  $\mathcal{D}_\ell^{TT}$  is related to the description above through

$$\mathcal{D}_\ell^{TT} = \frac{\ell(\ell+1)}{2\pi} C_\ell^{\Theta\Theta} \left( \frac{T_0}{1\ \mu\text{K}} \right)^2. \quad (4.27)$$

The spectrum is featureless up to  $\ell \simeq 100$ , the ‘Sachs-Wolfe plateau’. As super-curvature modes evolve freely up to decoupling, the scale-invariance of the initial perturbations is preserved on these scales. The comparatively large error bars reflect the cosmic variance. On intermediate scales  $100 \lesssim \ell \lesssim 1000$  the acoustic peaks dominate the spectrum. Above  $\ell \simeq 1000$  power is suppressed due to Silk damping.

#### 4.2.4. Secondary anisotropies

*Secondary anisotropies* are changes in the temperature distribution that are due to photon interactions after recombination. Massive structures along the photon path cause deflections, as detailed in Ch. 3. Since gravitational lensing is achromatic, the temperature and shape of the black-body spectrum are not affected, but as temperature fluctuations are redistributed, the change of the spatial pattern can be observed in the power spectrum; the acoustic peaks are smoothed out somewhat, and power is enhanced in the Silk damping tail of the spectrum (see e.g. the review by [Lewis & Challinor, 2006](#)). Moreover, the net gravitational redshift of photons crossing time-evolving potential wells in the foreground gives rise to the *integrated Sachs-Wolfe effect*, which is discussed in Sec. 7.2, and the *Rees-Sciama effect* in the non-linear regime of structure growth (for a recent review see [Nishizawa, 2014](#)).

Compton scattering of CMB photons off highly energetic free electrons, typically in the intracluster medium, is known as the *Sunyaev-Zel’dovich effect* ([Zel’dovich & Sunyaev, 1969](#)). For thermal electrons, photons are upscattered on average, leading to a characteristic distortion of the spectrum,

which supplies an important observational tool for the detection of galaxy clusters. Scattering off electrons in bulk flows induces a Doppler shift, the *kinetic Sunyaev-Zel'dovich effect* (Sunyaev & Zel'dovich, 1980), which changes the temperature, but preserves the Planckian shape of the spectrum.

### 4.3. The Formation of Haloes

In the mildly non-linear regime, structure formation can be treated in analytic models such as the Zel'dovich approximation (Zel'dovich, 1970). The collapse of a top hat density perturbation is the subject of the spherical collapse model. Beyond that, numerical simulations are needed to study the evolution of the matter distribution, the largest being the Millenium, Millenium-II and Millenium-XXL simulations (Springel et al., 2005; Boylan-Kolchin et al., 2009; Angulo et al., 2012), the Horizon Runs (Kim et al., 2009, 2011), the Bolshoi (Klypin et al., 2011) and MultiDark simulations (Prada et al., 2012) and the Illustris project (Vogelsberger et al., 2014).

#### 4.3.1. Spherical collapse

The spherical collapse model describes the evolution of a spherical and homogeneous overdense region in an expanding background. The growth of the sphere follows the expansion until 'turn-around', at which point it decouples and eventually collapses. In the following I sketch the evolution in a flat matter-dominated universe. This is a reasonable approximation for virialised objects observed today, as they collapse before dark energy domination and their sizes are much smaller than the curvature scale.

The expansion of the background is governed by the Friedmann equation (cf. Eqs. 2.6 and 2.15):

$$H(a) = H_0 a^{-3/2}. \quad (4.28)$$

The Newtonian equation of motion for a test particle on the surface of the sphere is

$$\ddot{R} = -\frac{GM}{R^2}, \quad (4.29)$$

where  $M$  is the mass enclosed within the sphere and  $R$  its radius; a dot denotes a time derivative. It is convenient to introduce the dimensionless coordinates

$$x = \frac{a}{a_{\text{ta}}}, \quad y = \frac{R}{R_{\text{ta}}}, \quad \tau = H_{\text{ta}} t, \quad (4.30)$$

where the subscript indicates the value of the parameter at turn-around;  $H_{\text{ta}} = H(a_{\text{ta}})$ . The mass in the overdense region is then

$$M = \frac{4\pi}{3} \rho_{\text{ta}} R_{\text{ta}}^3, \quad (4.31)$$

and the density  $\rho_{\text{ta}}$  at turn-around can be given in units of the critical density (cf. Eq. 2.13):

$$\xi = \frac{\rho_{\text{ta}}}{\rho_{\text{cr}}(a_{\text{ta}})}. \quad (4.32)$$

In this parametrisation, the two differential equations (4.28) and (4.29) become

$$x' = x^{-1/2}, \quad y'' = -\frac{\xi}{2y^2}. \quad (4.33)$$

The prime denotes the derivative with respect to  $\tau$ . The first equation implies

$$\tau = \frac{2}{3} x^{3/2}, \quad (4.34)$$

so that turn-around at  $x = 1$  occurs at the time  $\tau = 2/3$  and collapse at twice this time (for symmetry), i.e.  $\tau = 4/3$  and  $x = 2^{2/3}$ . At turn-around the radius of the sphere reaches its maximum, so that  $y' = 0$ , whereas  $y = 0$  initially at  $x = 0$ ; with these two boundary conditions the second differential equation can be solved, showing that the scaled density at turn-around is

$$\xi = \left(\frac{3\pi}{4}\right)^2. \quad (4.35)$$

The background density evolves as

$$\rho_{\text{bg}} = \rho_{\text{cr}}(a_{\text{ta}})x^{-3}, \quad (4.36)$$

while the density of the sphere follows

$$\rho = \rho_{\text{ta}}y^{-3}, \quad (4.37)$$

so that the overdensity at arbitrary times is

$$\Delta = \frac{\rho}{\rho_{\text{bg}}} = \xi \left(\frac{x}{y}\right)^3. \quad (4.38)$$

### 4.3.2. Virialisation

Collapse to a point of infinite density is clearly unphysical; instead virialisation is expected. The potential energy of a homogeneous sphere of radius  $R$  and mass  $M$  is

$$U(R) = -\frac{3GM}{5R}. \quad (4.39)$$

Since the kinetic energy vanishes at turn-around, energy conservation requires  $U(R_v) + T_v = U(R_{\text{ta}})$ , while the virial theorem states that  $U(R_v) = -2T_v$  (the subscript ‘v’ denotes values at virialisation). From  $U(R_v) = 2U(R_{\text{ta}})$  it follows that  $y = 1/2$ : the radius of the virialised sphere is half the radius at turn-around. Assuming that the halo is virialised at the collapse time  $\tau = 4/3$  with  $x = 2^{2/3}$ , according to Eq. (4.38) it reaches the overdensity

$$\Delta_v = 18\pi^2 \approx 178. \quad (4.40)$$

This is the overdensity of a virialised halo in a flat matter-dominated universe in the spherical collapse model, with respect to the mean density of the background at the time of formation.  $\Delta_v$  can be calculated numerically for more general models. [Bryan & Norman \(1998\)](#) supplied the following approximation for a flat universe with a cosmological constant:

$$\Delta_v(z) = 18\pi^2 + 82[\Omega_m(z) - 1] - 39[\Omega_m(z) - 1]^2. \quad (4.41)$$

Here the overdensity  $\Delta$  is measured with respect to the critical density  $\rho_{\text{cr}}(z)$ .

An alternative characterisation is based on linear growth. For early times (or small radii), the solution to the differential equations (4.33) may be expanded. The density contrast (see Eq. 4.4) to linear order in  $y$  is

$$\delta = \Delta - 1 = \frac{3y}{5}, \quad (4.42)$$

leading to the linearly evolved density contrast at collapse:

$$\delta_c = \frac{3}{5} \left(\frac{3\pi}{2}\right)^{2/3} \approx 1.686. \quad (4.43)$$

$\delta_c$  links the collapse of objects and linear theory of structure growth: a perturbation is expected to collapse when its density contrast scaled with the linear growth function reaches the value  $\delta_c$ .

The overdensity parameter  $\Delta$  is the basis for the definition of the *virial mass* and *virial radius* of a halo:  $r_\Delta$  is defined as the radius within which the average density is  $\Delta$  times the background density. Note that the background density may be the mean matter density or the critical density, depending on the definition; the latter is more common.  $M_\Delta$  is the enclosed mass. While virialisation is expected to lead to an overdensity  $\Delta_v$ , which depends on the cosmological model and the redshift, a widely used convention is  $\Delta = 200$ .

### 4.3.3. The Navarro-Frenk-White profile

Navarro et al. (1996) found that the density profiles of dark matter haloes in numerical simulations can be described by a ‘universal profile’ for a wide range of masses, including dwarf galaxies at the low end and clusters at the high end. This *NFW profile* has the form

$$\rho(r) = \frac{\rho_s}{\frac{r}{r_s} \left(1 + \frac{r}{r_s}\right)^2}. \quad (4.44)$$

The parameter  $r_s$  is the *scale radius*. For  $r \ll r_s$  the logarithmic slope approaches  $-1$ , whereas the density drops  $\sim r^{-3}$  at large radii. The scale radius is marked by  $d \ln \rho / d \ln r = -2$ .

An NFW halo is commonly characterised by its *concentration parameter*, the ratio of the virial radius and the scale radius:

$$c = \frac{r_{200}}{r_s}. \quad (4.45)$$

The concentration parameter is linked to the density parameter  $\rho_s$  through the requirement that the average density within  $r_{200}$  is 200 times the critical density  $\rho_{\text{cr}}$ , thus:

$$4\pi \int_0^{r_{200}} dr r^2 \rho(r) = \frac{4\pi}{3} r_{200}^3 \times 200 \rho_{\text{cr}}. \quad (4.46)$$

The integral can be solved analytically, leading to

$$\rho_s = \frac{200 \rho_{\text{cr}}}{3} \frac{c^3}{\ln(1+c) - \frac{c}{1+c}}. \quad (4.47)$$

The framework of the spherical collapse model implies that the post-collapse density, reflected in the parameter  $\rho_s$ , should be a fixed multiple of the mean matter density of the background at the time of formation, which decreases with time. Equation (4.47) then establishes a relation between the concentration and the formation time: haloes that form earlier are more concentrated. As the smallest haloes are the first to assemble, the concentration decreases with increasing mass. This *concentration-mass relation* was noted already by Navarro et al. (1996, 1997), and its form and scatter have since been studied extensively (e.g. Wechsler et al., 2002; Zhao et al., 2003; Bullock et al., 2001; Eke et al., 2001; Neto et al., 2007; Macciò et al., 2007, 2008); typically a shallow scaling of the form  $c \sim M^{-\alpha}$  with  $\alpha \sim 0.1$  is found.

It is noteworthy that other profiles have been shown to provide similar or better fits than the NFW profile, in particular the Einasto profile (Navarro et al., 2004; Hayashi & White, 2008; Gao et al., 2008; Springel et al., 2008):

$$\rho(r) = \rho_{-2} \exp \left\{ -\frac{2}{\alpha} \left[ \left( \frac{r}{r_{-2}} \right)^\alpha - 1 \right] \right\}. \quad (4.48)$$

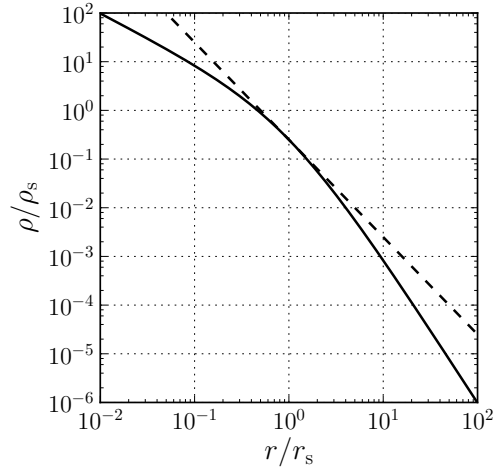


**Figure 4.3.:** The NFW density profile. The dashed line is the tangent at the scale radius with a logarithmic slope of  $-2$ .

The logarithmic slope is a power law with exponent  $\alpha$  and  $d \ln \rho / d \ln r = -2$  at  $r_{-2}$ , lacking the fixed asymptotes of the NFW profile;  $\rho_{-2} = \rho(r_{-2})$ . The parameter  $\alpha$  is typically in the range  $0.12 \leq \alpha \leq 0.25$  and increases with mass.

Irrespective of the profile family, discrepancies may be large for individual haloes due to significant amounts of substructure or triaxiality (e.g. [Jing & Suto, 2002](#)).



# 5

## Construction of an Integral Density Estimator

In this chapter I introduce the density estimator on which the geometric analysis in Ch. 6 is based. A map of the smoothed convergence is obtained by integrating over the shear field with a suitable weight function. The method is designed to maximise the use of available information.

### 5.1. Available Data and Methods of Analysis

The primary observable of weak lensing is the shear  $\gamma$ , which quantifies the anisotropic distortion of lensed images. When individual lenses are studied, the aim is usually the recovery of the mass distribution, or the surface mass density  $\kappa$ . Since both  $\gamma$  and  $\kappa$  are second derivatives of the lensing potential (or combinations thereof), it is evident that the convergence can be reconstructed from measurements of the shear. The main difficulty is the contamination due to intrinsic ellipticities. In the following I explain what measurements are typically available and how the convergence is commonly reconstructed from such data.

#### 5.1.1. Measurement of the shear

While the ellipticity of a perfect ellipse with semi-major axes  $a$  and  $b$  ( $a \geq b$ ) is defined as the ratio  $(a-b)/(a+b)$ , the isophotes of a galaxy do not necessarily conform to this description, and a different estimator is needed. Information about shape can be extracted from a brightness distribution  $I(\theta)$  in terms of its moments (Bartelmann & Schneider, 2001). Defining the centre of brightness as

$$\bar{\theta} = \frac{\int d^2\theta \theta I(\theta)}{\int d^2\theta I(\theta)}, \quad (5.1)$$

the second moments are given by

$$Q_{ij} = \frac{\int d^2\theta (\theta_i - \bar{\theta}_i)(\theta_j - \bar{\theta}_j) I(\theta)}{\int d^2\theta I(\theta)}, \quad i, j \in \{1, 2\}. \quad (5.2)$$

Other schemes than the simple weighting with  $I(\theta)$  are possible. An ellipticity parameter is derived from these moments as

$$\epsilon = \frac{Q_{11} - Q_{22} + 2iQ_{12}}{Q_{11} + Q_{22} + 2\sqrt{Q_{11}Q_{22} - Q_{12}^2}}. \quad (5.3)$$

For a perfect ellipse  $|\epsilon| = (a-b)/(a+b)$  is recovered, and the argument of the complex quantity corresponds to the position angle.

Measured ellipticities are not generally unbiased estimators of the gravitational shear field, as they are contaminated e.g. by atmospheric seeing and instrument noise. In particular, anisotropies in the point-spread function of the telescope and detector can mimic a shear signal and need to be removed. Approaches that address this difficulty include the KSB (Kaiser et al., 1995; Luppino & Kaiser, 1997) and KSB+ (Hoekstra et al., 1998) algorithms; shapelet-based methods (Refregier, 2003; Refregier & Bacon, 2003; Massey & Refregier, 2005); and parametric galaxy-fitting (e.g. Miller et al., 2007; Kitching et al., 2008a; Miller et al., 2013)

In the weak lensing approximation, the observed ellipticity  $\epsilon = \epsilon_s + \gamma$  of a galaxy image is the sum of the intrinsic ellipticity  $\epsilon_s$  of the source and the shear  $\gamma$ . All of the quantities are complex, taking the orientation of the source galaxy and the direction of the shear-induced elongation into account. The probability distribution of the intrinsic ellipticities is commonly described as either a Gaussian or a Rayleigh distribution (Viola et al., 2014); the latter corresponds to a Gaussian distribution for each component. It is characterised by the intrinsic ellipticity dispersion  $\sigma_\epsilon^2 = \langle |\epsilon_s|^2 \rangle$ , commonly estimated as  $\sigma_\epsilon \simeq 0.2\text{--}0.3$ . In the weak lensing regime the shear is typically much smaller than the intrinsic ellipticity of the source, so that it is practically impossible to extract a shear value from a single ellipticity measurement. If, however, ellipticities have also been determined for nearby galaxies, their average is a good estimator for the local shear, provided that the sources are randomly oriented. If any correlation in the ellipticities of images is exclusively caused by lensing, the expectation value of the complex ellipticity of a source vanishes,  $\langle \epsilon_s \rangle = 0$ , and a finite value of the average ellipticity indicates the presence of gravitational shear,  $\langle \epsilon \rangle = \gamma$ . This averaging can be carried out in cells on a grid, creating a two-dimensional map, or in radial bins, i.e. rings, resulting in a radial profile of the shear.

### 5.1.2. Reconstruction of the convergence

If a radial shear profile has been derived from the data, a simple way to approximate the mass distribution is parametric fitting. Given that axisymmetry has been assumed for the shear field, the density field must be axisymmetric as well. One can then choose a mass model, such as the NFW profile, and determine the best-fitting parameters by matching the shear of the model to the data. For an NFW halo, the mass and concentration (or virial radius and scale radius) can be recovered in this way. More complex models, e.g. elliptical extensions, can be adjusted to two-dimensional shear fields.

More generally, the convergence can also be reconstructed using parameter-free methods. Kaiser & Squires (1993) pointed out that the convergence is obtained from the shear via the convolution

$$\kappa(\boldsymbol{\theta}) - \kappa_0 = \frac{1}{\pi} \int d^2\theta' \Re [D^*(\boldsymbol{\theta} - \boldsymbol{\theta}')\gamma(\boldsymbol{\theta}')] \quad (5.4)$$

with the kernel

$$D(\boldsymbol{\theta}) = \frac{\theta_1^2 - \theta_2^2 + 2i\theta_1\theta_2}{|\boldsymbol{\theta}|^4}. \quad (5.5)$$

This is most easily derived in Fourier space. The unconstrained constant  $\kappa_0$  is a manifestation of the mass sheet degeneracy, which cannot be broken from shear data alone. For applications see Fahlman et al. (1994); Seitz & Schneider (1995, 1996). Bartelmann et al. (1996), Seitz et al. (1998) and Marshall et al. (2002) developed maximum-likelihood approaches to the reconstruction. Moreover, algorithms have been presented which incorporate strong lensing data (Bradač et al., 2005a,b, 2006; Cacciato et al., 2006) or even constraints from other effects such as X-ray emission, the Sunyaev-Zel'dovich effect and galaxy kinematics (Merten et al., 2009; Konrad et al., 2013; Majer et al., 2013; Sarli et al., 2014; Tchernin et al., 2015).

## 5.2. Derivation of the $\zeta$ -Statistics

I search for an estimator of the density field which has the following properties: it should permit the recovery of characteristic scales, such as the scale radius of an NFW profile; it should be based directly on observables; it should be an integral measure, designed to use as much information as possible for each point; and it should avoid prejudices. The last demand entails that assumptions about symmetries or parametric shapes should be kept at a minimum. In this section I argue that approaches developed by [Kaiser \(1995\)](#) and [Schneider & Bartelmann \(1997\)](#) meet these requirements.

### 5.2.1. Axisymmetry

[Kaiser \(1995\)](#) proposed to derive the mass inside a circular aperture from shear data as follows:

In polar coordinates  $(r, \varphi)$ , the  $\delta$ -operator has the form

$$\delta = e^{i\varphi} \left( \partial_r + \frac{i}{r} \partial_\varphi \right). \quad (5.6)$$

The convergence  $\kappa$  is then a combination of radial and angular derivatives of the lensing potential  $\psi$ :

$$\kappa = \frac{1}{2} \bar{\delta} \delta \psi = \frac{1}{2} \left( \frac{\partial^2 \psi}{\partial r^2} + \frac{1}{r} \frac{\partial \psi}{\partial r} + \frac{1}{r^2} \frac{\partial^2 \psi}{\partial \varphi^2} \right). \quad (5.7)$$

For the shear it is useful to define the tangential component  $\gamma_T$  and the cross-component  $\gamma_X$  with respect to the origin:

$$\gamma_T = -\Im \left[ \gamma e^{-2i\varphi} \right] = \frac{1}{2} \left( -\frac{\partial^2 \psi}{\partial r^2} + \frac{1}{r} \frac{\partial \psi}{\partial r} + \frac{1}{r^2} \frac{\partial^2 \psi}{\partial \varphi^2} \right), \quad (5.8)$$

$$\gamma_X = -\Re \left[ \gamma e^{-2i\varphi} \right] = \frac{1}{r^2} \frac{\partial \psi}{\partial \varphi} - \frac{1}{r} \frac{\partial^2 \psi}{\partial r \partial \varphi}. \quad (5.9)$$

A negative value of  $\gamma_T$  indicates that the distortion is aligned along the radial direction.

The first derivatives of the convergence are third derivatives of the lensing potential and can easily be expressed as linear combinations of the shear and its derivatives:

$$\partial_r \kappa = -\partial_r \gamma_T - \frac{2}{r} \gamma_T - \frac{1}{r} \partial_\varphi \gamma_X, \quad (5.10)$$

$$\partial_\varphi \kappa = -r \partial_r \gamma_X + \partial_\varphi \gamma_T - 2\gamma_X. \quad (5.11)$$

Consider now the mean convergence inside an aperture of radius  $R$ , centred on the origin:

$$\bar{\kappa}(R) = \frac{1}{\pi R^2} \int_0^{2\pi} d\varphi \int_0^R dr r \kappa(r, \varphi). \quad (5.12)$$

Integration by parts with respect to  $r$  introduces a term containing the derivative  $\partial_r \kappa$ , for which the relation (5.10) can be substituted. Eventually,

$$\bar{\kappa}(R) = \langle \kappa(R) \rangle + \langle \gamma_T(R) \rangle, \quad (5.13)$$

where the brackets denote angular averaging, i.e.

$$\langle \kappa(R) \rangle = \frac{1}{2\pi} \int_0^{2\pi} d\varphi \kappa(R, \varphi) \quad (5.14)$$

is the mean convergence around a circular loop of radius  $R$  and the analogue holds for the shear  $\gamma_T$ . Taking the derivative of Eq. (5.12), one finds

$$\begin{aligned}\partial_R \bar{\kappa}(R) &= -\frac{2}{R} \bar{\kappa}(R) + \frac{2}{R} \langle \kappa(R) \rangle \\ &= -\frac{2}{R} \langle \gamma_T(R) \rangle,\end{aligned}\quad (5.15)$$

from which one finally derives:

$$\bar{\kappa}(r < r_1) - \bar{\kappa}(r_1 < r < r_2) = \frac{2}{1 - r_1^2/r_2^2} \int_{r_1}^{r_2} d \ln r \langle \gamma_T(r) \rangle. \quad (5.16)$$

This quantity is often called the  $\zeta$ -statistics or aperture mass. Some explanations are needed here: first,  $\bar{\kappa}(r < r_1)$  is the mean convergence (or surface mass density) within a circle of radius  $r_1$ ;  $\bar{\kappa}(r_1 < r < r_2)$  is the mean convergence in an annulus with inner radius  $r_1$  and outer radius  $r_2 > r_1$ . Note that, if the  $\varphi$ -integration for the average  $\langle \gamma_T \rangle$  is taken into account, this annulus constitutes the domain of the integration. Obviously the mean surface density  $\bar{\kappa}(r < r_1)$  is proportional to the mass contained within the radius  $r_1$ . Equation (5.16) then provides a lower bound on the aperture mass: it must be no greater than the integral on the right-hand side. Moreover, the larger the control annulus from  $r_1$  to  $r_2$ , i.e. the higher the ratio  $r_2/r_1$ , the closer  $\bar{\kappa}(r_1 < r < r_2)$  will be to the mean background density, and the better the approximation of the aperture mass by the lower bound. Remarkably, the lower bound is obtained by integrating over the shear outside the aperture rather than inside, and in fact over a domain potentially much larger than the aperture.

### 5.2.2. Extension to arbitrary geometries

The approach described above provides an interesting prescription for the calculation of the mean convergence. It does not rely on symmetry assumptions or parametric models, and it is based on an (approximate) observable, at least in the weak lensing regime. In principle it is possible to construct a map of an appropriately defined convergence estimator by applying (5.16) to points on a grid, moving the aperture across the field. The size of such a map, however, would be severely limited by the demand that the field of view, i.e. the region for which shear data are available, must contain not only the aperture, but also the control annulus; otherwise the sampling of the integral required in the calculation is compromised. As established in the previous section, a large annulus comprising as large a part of the field as possible is preferable, so that a somewhat modified algorithm is needed to create a map of reasonable size. To that end, a generalisation by [Schneider & Bartelmann \(1997\)](#), which I describe in the following, proves immensely useful.

An aperture mass measure  $m$  is defined by the integral

$$m(\mathbf{x}_0) = \int d^2y w(\mathbf{y} - \mathbf{x}_0) \kappa(\mathbf{y}), \quad (5.17)$$

The weight function  $w$  may in the simplest case be a circular top hat filter. For Kaiser's  $\zeta$ -statistics (Eq. 5.16) a term reflecting the control annulus would have to be subtracted. A set of nested closed curves is parametrised as  $\hat{\mathbf{c}}(\hat{b}, \hat{\lambda})$ , where  $\hat{\lambda} \in [0, \lambda_{\max}]$  is cyclic. Roughly, the parameter  $\hat{b}$  can be thought of as picking out one of the curves, while  $\hat{\lambda}$  moves along it. It is required that the weight function  $w$  must be constant along each of these curves, i.e. it may only be a function of the parameter  $\hat{b}$ . In these coordinates the Jacobian is

$$\hat{J}(\hat{b}, \hat{\lambda}) = \frac{\partial \hat{c}_1}{\partial \hat{b}} \frac{\partial \hat{c}_2}{\partial \hat{\lambda}} - \frac{\partial \hat{c}_2}{\partial \hat{b}} \frac{\partial \hat{c}_1}{\partial \hat{\lambda}}, \quad (5.18)$$

and the area enclosed by a curve is

$$A(\hat{b}) = \int_0^{\hat{b}} d\tilde{b} \oint d\hat{\lambda} \hat{J}(\tilde{b}, \hat{\lambda}) = \frac{1}{2} \oint d\hat{\lambda} \left( \hat{c}_1 \frac{\partial \hat{c}_2}{\partial \hat{\lambda}} - \hat{c}_2 \frac{\partial \hat{c}_1}{\partial \hat{\lambda}} \right). \quad (5.19)$$

Concentric circles are an illustrative example. Arguably the most intuitive choice to label them is by their radius  $r$  and a polar angle  $\varphi$  running from 0 to  $2\pi$ . The area enclosed by one of these curves is  $A(r) = \pi r^2$ . One can parametrise the set of arbitrary nested curves to share this property, defining the new ‘radius’

$$b(\hat{b}) = \sqrt{\frac{2A(\hat{b})}{\lambda_{\max}}}. \quad (5.20)$$

Another analogy can be constructed if a new cyclic coordinate  $\lambda$  is introduced: in ordinary polar coordinates, the Jacobian is equal to the radial coordinate  $r$ . Likewise, one demands that  $J(b, \lambda) = b$ , leading to

$$\lambda(b, \hat{\lambda}) = \frac{\lambda_{\max}}{\oint d\tilde{\lambda} \hat{J}[\hat{b}(b), \tilde{\lambda}]} \int_0^{\hat{\lambda}} d\tilde{\lambda} \hat{J}[\hat{b}(b), \tilde{\lambda}]. \quad (5.21)$$

If the nested curves are in fact circles, this transform evidently parametrises them by their radius and polar angle. In the following I use the notation  $\mathbf{c}(b, \lambda) = \hat{\mathbf{c}}[\hat{b}(b), \hat{\lambda}(b, \lambda)]$ ,  $\mathbf{c}' = \partial \mathbf{c} / \partial b$ ,  $\dot{\mathbf{c}} = \partial \mathbf{c} / \partial \lambda$ . The prime symbol ‘ $\prime$ ’ and dot ‘ $\dot{\phantom{x}}$ ’ denote derivatives with respect to  $b$  and  $\lambda$ , respectively, also for other quantities. For brevity I also make use of a mapping to the complex plane and write  $C = c_1 + ic_2$ .

With the coordinate transformation

$$\mathbf{y} = \mathbf{x}_0 + \mathbf{c}(b, \lambda), \quad (5.22)$$

the integral (5.17) for the aperture mass becomes

$$m(\mathbf{x}_0) = \int db b w(b) \oint d\lambda \kappa[\mathbf{x}_0 + \mathbf{c}(b, \lambda)]. \quad (5.23)$$

Integration by parts with respect to  $b$  introduces the integral

$$W(b) = \frac{1}{b} \int_0^b d\tilde{b} \tilde{b} w(\tilde{b}) \quad (5.24)$$

and leads to

$$m(\mathbf{x}_0) = - \int db b W(b) \oint d\lambda \partial_b \kappa[\mathbf{x}_0 + \mathbf{c}(b, \lambda)], \quad (5.25)$$

provided that the weight function falls off more steeply than  $b^{-1}$  for  $b \rightarrow \infty$  and fulfils

$$\int_0^\infty db b w(b) = 0. \quad (5.26)$$

The derivative of the convergence can be written as a linear combination of derivatives of the shear, similar to (5.10):

$$\partial_b \kappa = \frac{1}{b} \mathfrak{I} \left[ (C'^2)^* \partial_\lambda \gamma - (C' \dot{C})^* \partial_b \gamma \right]. \quad (5.27)$$

The result for the aperture mass after another integration by parts is

$$m(\mathbf{x}_0) = \int db b \oint d\lambda \left\{ \left[ \frac{W(b)}{b^2} - \frac{w(b)}{b} \right] \mathfrak{I} [(C' \dot{C})^* \gamma] + \frac{W(b)}{b} \mathfrak{I} [(C' \dot{C}' - C'' \dot{C})^* \gamma] \right\}. \quad (5.28)$$

Again the aperture mass is expressed in terms of an integral over the shear, albeit with a more complicated weighting than Kaiser’s  $\zeta$ -statistics in Eq. (5.16). The latter is easily recovered when the appropriate filter  $w$  is used and  $C$  is specified to comprise a set of concentric circles. Equation (5.28) is very flexible in its application, depending on the chosen parametrisation  $C$  combined with the filter  $w$ . The only requirements are that the weight function must drop to zero fast enough (Eq. 5.26), and that  $C$  must be twice differentiable with respect to  $b$  and once with respect to  $\lambda$ ; note that this demand entails that the family of curves  $\hat{\mathbf{c}}$  must be twice differentiable with respect to both  $\hat{b}$  and  $\hat{\lambda}$ .

Finally, to generalise the  $\zeta$ -statistics introduced by Kaiser (1995) to a somewhat different geometric set-up in which the outer boundary of the control ‘annulus’ is not circular, I consider

$$\Delta\bar{\kappa} = \bar{\kappa}(b < b_1) - \bar{\kappa}(b_1 < b < b_2), \quad (5.29)$$

instead of the original quantity given in Eq. (5.16).  $\bar{\kappa}(b < b_1)$  is the mean convergence within the  $b_1$ -curve, while  $\bar{\kappa}(b_1 < b < b_2)$  is the mean convergence between  $b_1$  and  $b_2$ ; the region between two nested curves replaces the control annulus. The weight function  $w$  is then a step function, constant in each of these domains and zero elsewhere.

In order to define a convergence estimator, it is natural to retain the circular shape of the inner curve labelled  $b_1$ .  $\bar{\kappa}(b < b_1)$  is then the convergence smoothed with a circular top hat filter. This would indeed be of great interest, however, the correction term  $\bar{\kappa}(b_1 < b < b_2)$  cannot be made to vanish entirely – setting  $w(b) = 0$  for  $b > b_1$  violates the condition set in Eq. (5.26). Instead a compensated filter is required:

$$w(b) = \begin{cases} [A(b_1)]^{-1} & \text{if } b \leq b_1 \\ [A(b_2) - A(b_1)]^{-1} & \text{if } b_1 < b \leq b_2 \\ 0 & \text{if } b > b_2 \end{cases} . \quad (5.30)$$

Given that the control term  $\bar{\kappa}(b_1 < b < b_2)$  is inevitably finite, it should preferably have two properties: it should be small; and it should vary only weakly with position. In fact the latter requirement is crucial if  $\Delta\bar{\kappa}$  is to be treated as an estimator of the smoothed convergence. This can be achieved if the control annulus is much larger than the aperture. While such a set-up was impractical for the original  $\zeta$ -statistics (see Sec. 5.2.2), it can indeed be realised in the more general approach. As the nested curves need not be circular, a rectangle delineating the borders of the field of view may be chosen as the outer boundary at  $b = b_2$ ; and as they need not be concentric, this outer curve may remain fixed as the aperture moves about the field.  $\Delta\bar{\kappa}$  as defined in Eq. (5.29) is then the mean convergence within the aperture relative to the mean convergence across the rest of the field (the complement), calculated from an integral over the shear (multiplied by a weight) across the field.

An important simplification for a circular aperture was noted by Schneider & Bartelmann (1997): in such a case, it is natural that the nested curves up to the scale  $b_1$  should be concentric circles. Such a set of self-similar curves can be parametrised as  $C = bK(\lambda)$ , with the derivatives  $C' = K$ ;  $C'' = 0$ ;  $\dot{C} = b\dot{K}$ ; and  $\dot{C}' = \dot{K}$ . Given the shape of the filter (5.30), it is easy to show that the integrand of (5.28) vanishes for  $b < b_1$ , so that the integral becomes an integral over the shear in the control annulus only.

### 5.3. Application

The smoothed convergence  $\Delta\bar{\kappa}$ , defined in Eq. (5.29), can be calculated by integrating over the shear field. To determine the weight for this integration, it is necessary to construct a set of nested curves containing both a circular loop, the radius of which is the smoothing scale, and a rectangle of the size of the field of view. In the following I present a suitable parametrisation and discuss properties of the weight function, in particular the influence of noise when an estimator is derived from shear data.

#### 5.3.1. Parametrisation and weight function

The geometric set-up of the parametrisation described in the following is sketched in Fig. 5.1. I consider a rectangular field, the corners of which lie at  $\pm a/2 \pm ib/2$  in the complex plane, so that the centre is at the origin. Let  $R$  be the radius of the circular aperture and  $M = x + iy$  the position of its centre. Then a polar coordinate system with its origin at  $M$  can be defined, so that the boundary of the field is described by the closed curve  $M + s(\varphi)e^{i\varphi}$ .  $\varphi \in [-\pi, \pi]$  is the angular coordinate measured counterclockwise from the real axis, and  $s(\varphi)$  is the distance from the aperture centre to the boundary of the field measured under that angle. To preserve mirror symmetry, a new angular coordinate  $\hat{\lambda}$  is



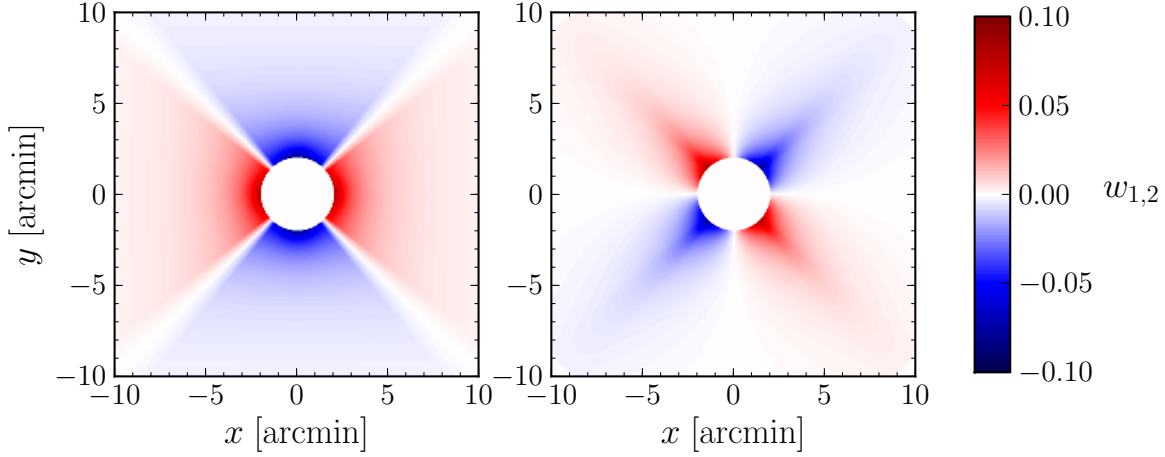


**Figure 5.2.:** Weights  $w_+$  (left) and  $w_\times$  (right) for the two shear components for the  $\zeta$ -statistics. The aperture has a radius of  $R = 2'$ .

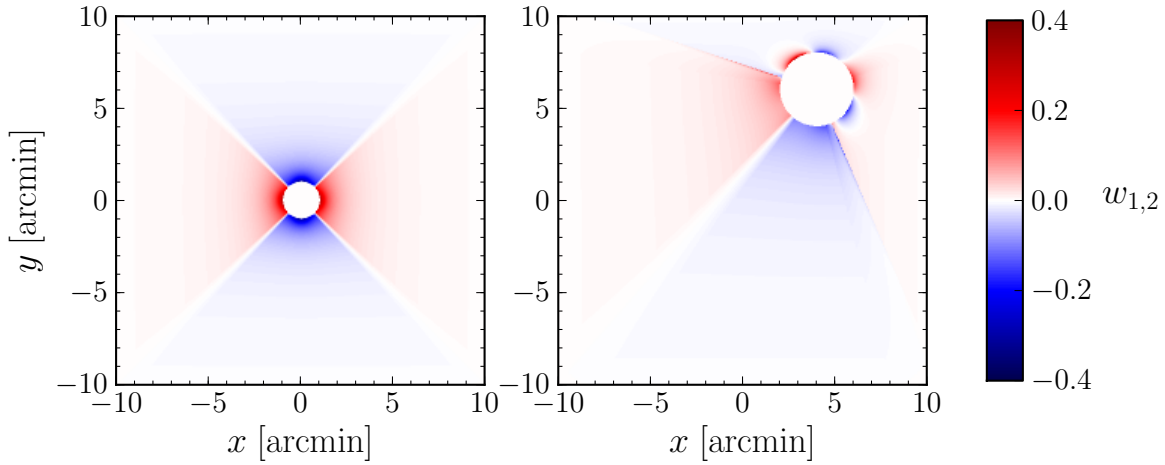


**Figure 5.3.:** Weight  $w_+$  for the first shear component for the  $\zeta$ -statistics. In the left panel, the aperture is placed in the centre and has a smoothing scale of  $R = 1'$  (compared to  $R = 2'$  in Fig. 5.2). In the right panel, the smoothing scale is  $R = 2'$  and the aperture is placed off centre at  $(x, y) = (4', 6')$ .

Given the parametrisation, the weight function for the calculation of

$$\Delta\bar{\kappa}(\mathbf{x}) = \int d^2\mathbf{y} [w_+(\mathbf{y}; \mathbf{x})\gamma_+(\mathbf{y}) + w_\times(\mathbf{y}; \mathbf{x})\gamma_\times(\mathbf{y})] \quad (5.34)$$

can be constructed. Its properties are illustrated in Figs. 5.2 and 5.3 for a square field with a side length of  $20'$ . In Fig. 5.2 the aperture is placed in the centre of the field and has a radius of  $R = 2'$ . This is somewhat larger than the smoothing scales one would typically choose to analyse data, since the scale radii of clusters are often smaller, but the structure of the weight function is the same for smaller smoothing scales and more easily visualised in the case of a large aperture.

By the design of the  $\zeta$ -statistics the weight function is always zero inside the aperture, and outside its absolute value decreases with increasing distance.  $w_+$  is symmetric under  $x \rightarrow -x$  and  $y \rightarrow -y$ , whereas exchanging  $x \leftrightarrow y$  changes the sign; the situation is reversed for  $w_\times$ , for which the diagonals are the axes of symmetry. This behaviour matches that of the shear field for an axisymmetric lens in the centre of the field, i.e. it ensures that in such a case negative values of the shear components receive a negative weight.

The steepness of the weight function depends on the aperture size and its position in the field,

as shown in Fig. 5.3 (note the different range of the colour bar). The profile is much narrower and subsequently higher for smaller smoothing scales,  $R = 1'$  in this example. Moreover, for the larger smoothing scale of  $R = 2'$  the weight function is clearly steeper when the aperture is moved close to the edges, compared to the position in the centre.

### 5.3.2. Noise

Any estimate of the quantity  $\Delta\bar{\kappa}$  derived from data will inevitably be affected by noise. First, the integrand can only be evaluated at positions where galaxies are observed; and second, shear measurements are contaminated by the intrinsic ellipticities of the sources. In the weak lensing regime, the observed ellipticity is  $\epsilon = \gamma + \epsilon^{(s)}$ . Assuming that the distribution of sources is uniform with a density  $n$ , applying (5.34) to data leads to the estimator

$$k(\mathbf{x}) = \frac{1}{n} \sum_{i=1}^N [w_{+,i}\epsilon_{+,i} + w_{\times,i}\epsilon_{\times,i}], \quad (5.35)$$

where the sum is over the positions  $\mathbf{y}_i$  of a total of  $N$  galaxies and  $w_{+,i}$  is short for  $w_+(\mathbf{y}_i; \mathbf{x})$  etc. The variance of this estimator is most easily understood if an empty field is considered, i.e.  $\gamma = 0$ . Since the expectation value of the intrinsic ellipticity vanishes,  $\langle k(\mathbf{x}) \rangle = 0$ . If ellipticities are uncorrelated,

$$\langle \epsilon_{+,i}^{(s)} \epsilon_{+,j}^{(s)} \rangle = \langle \epsilon_{\times,i}^{(s)} \epsilon_{\times,j}^{(s)} \rangle = \frac{\sigma_\epsilon^2}{2} \delta_{ij}^K, \quad (5.36)$$

leading to the variance

$$\sigma_\kappa^2(\mathbf{x}) = \langle k^2(\mathbf{x}) \rangle = \frac{\sigma_\epsilon^2}{2n} \int d^2y [w_+^2(\mathbf{y}; \mathbf{x}) + w_\times^2(\mathbf{y}; \mathbf{x})]. \quad (5.37)$$

Equation (5.37) describes how an estimate for  $\Delta\bar{\kappa}(\mathbf{x})$  varies over different realisations of the source distribution, due to discreteness and shape noise. The proportionality to the intrinsic ellipticity dispersion  $\sigma_\epsilon^2$  is hardly surprising. The factor  $n^{-1}$  is also expected, reflecting the usual scaling of Poissonian errors – the higher the source density, the better the sampling of the integrand of Eq. (5.34), and the better the approximation by the sum (5.35).

$\sigma_\kappa$  is plotted in Fig. 5.4. Again the field size is  $20' \times 20'$ . The aperture has a radius of  $R = 0.6'$ . The source density is  $n = 30 \text{ arcmin}^{-2}$  and the intrinsic ellipticity dispersion  $\sigma_\epsilon = 0.3$ . The profile is shallow with  $\sigma_\kappa \lesssim 0.05$  out to radii of about  $5'$ , but it rises sharply near the corners, reaching values above 0.4. This increase can be understood if the structure of the weight function is recalled (see Sec. 5.3.1): for points close to the borders of the field, the weight function is comparatively narrow, and the same is true for small smoothing scales (cf. Fig. 5.3). In such cases, the effective integration domain, i.e. the region where the weight function has appreciable values, is small. If the weight function is shallow, a large number of sources contributes to the sum, approximating the integral reasonably well, and as many sources are assigned a similar weight, their intrinsic ellipticities average out to some degree, suppressing the shape noise. If, however, the weight function is steep, individual sources are weighted strongly, and their ellipticities are likely to introduce considerable errors.

In summary, the following quantities influence the noise  $\sigma_\kappa$ :

- the intrinsic ellipticity dispersion: the variance is proportional to  $\sigma_\epsilon^2$ ;
- the source density: the higher  $n$ , the lower the variance;
- the aperture size: smaller values of  $R$  result in steep weight functions and a large variance;
- the field size  $(a, b)$ : the variance increases steeply near the edges of the field, in particular the corners.

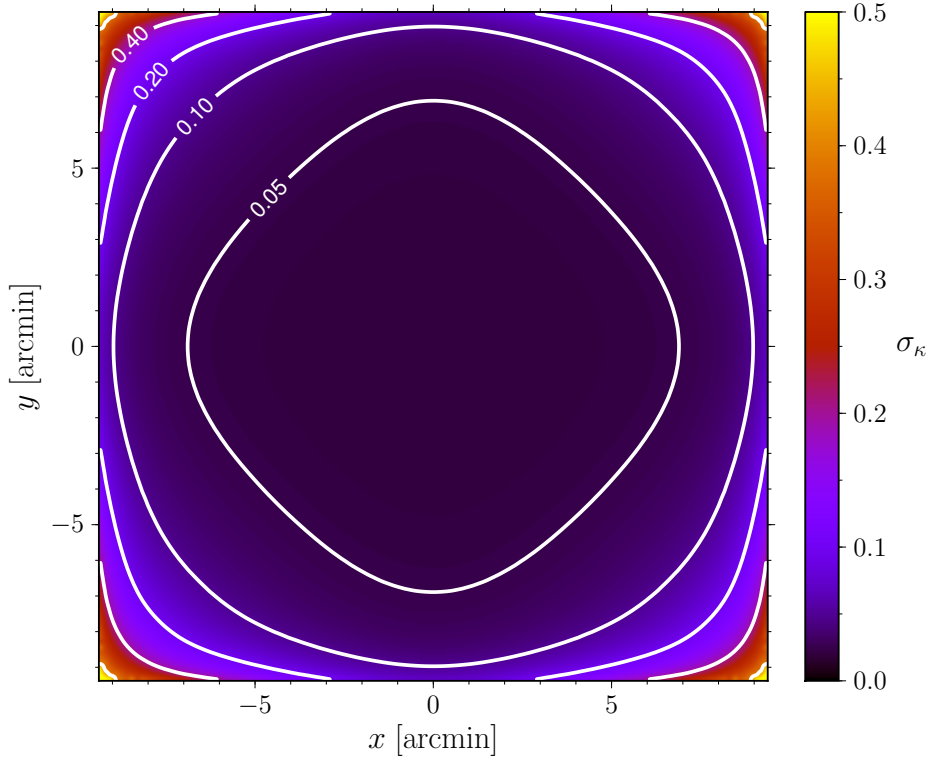


**Figure 5.4.:** Noise contribution  $\sigma_\kappa$  to the  $\zeta$ -statistics for a  $20' \times 20'$ -field and a smoothing scale of  $R = 0.6'$ .

The variance is always highest close to the borders of the field, so it is preferable if any regions of interest are well inside the field, avoiding the noisy edges. It should be noted that the larger effective integration domains associated with shallower weight profiles necessarily introduce strong correlations in the convergence estimates of nearby points.

### 5.3.3. The smoothing scale

Recalling the definition of the convergence estimator  $\Delta\bar{\kappa}$  in Eq. (5.29), it would be desirable to make the aperture ‘as small as possible’ in order to avoid smoothing out features in the true convergence field and to limit the variations of the mean convergence in the control annulus. It should be noted that even for extremely small smoothing scales, the resolution of the  $\Delta\bar{\kappa}$ -map is still limited by the source density. If the grid constant of the map is much smaller than the mean distance between galaxies, the summation in Eq. (5.35) will be over the same set of sources for neighbouring points, with only a slight change in the weight function. Features in the underlying density field can hardly be resolved reliably on these scales. On the other hand, the previous section has shown that lowering the aperture size raises the noise level.

In Fig. 5.5 the two competing influences on the signal-to-noise ratio are illustrated. I compare the maximum of the smoothed convergence  $\Delta\bar{\kappa}$ , which is the value at the centre of the lens, to the expected noise level  $\sigma_\kappa(0)$  (see Eq. 5.37) in the centre of field and denote by  $\Sigma = \Delta\bar{\kappa}(0)/\sigma_\kappa(0)$  the signal-to-noise ratio. As the variance profile is shallow in the central region,  $\Sigma$  is an appropriate measure even if the lens is positioned off the centre.  $\Delta\bar{\kappa}(0)$  and  $\Sigma$  are plotted for three different NFW haloes, which all have the same mass of  $M = 10^{15} h^{-1} M_\odot$ , but different concentrations ( $c = 2, 4, 6$ ); the lens and source redshifts are  $z_d = 0.3$  and  $z_s = 2.0$ , respectively. In addition, the noise for a square field of  $20'$  side length is shown. Smoothing scales between  $1''$  and  $60''$  are considered.

The signal is largest for the highest concentration, as the lensing efficiency of a halo increases with the concentration. Similarly, the signal would increase with the mass and the source redshift and

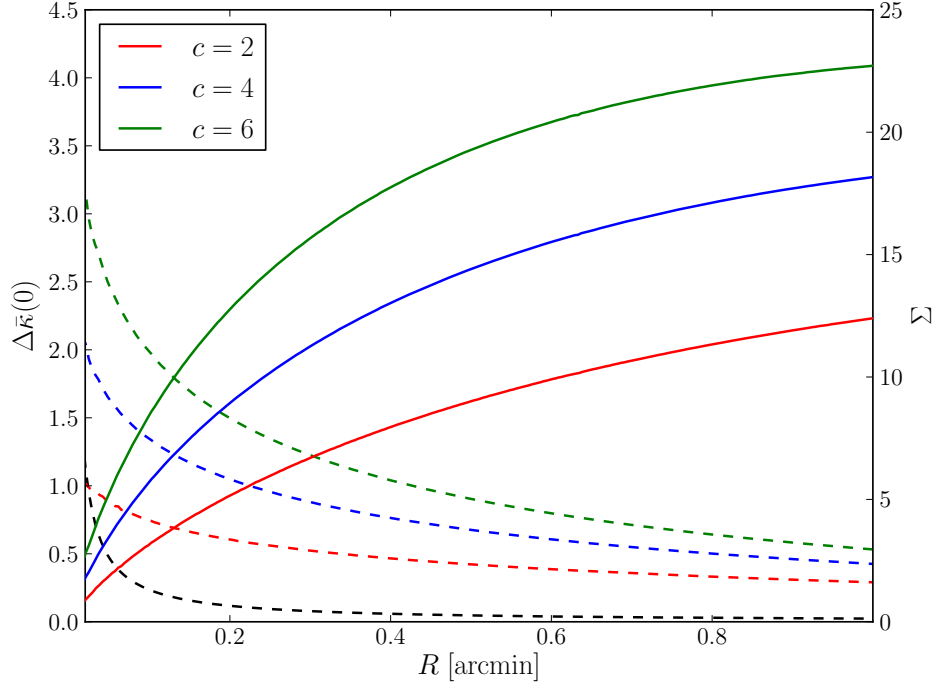


**Figure 5.5.:** Signal-to-noise ratio  $\Sigma$  of the  $\zeta$ -statistics as a function of the smoothing scale  $R$ , for three NFW haloes. Coloured dashed lines show the value of the signal  $\Delta\bar{\kappa}(0)$  at the lens centre, which coincides with the centre of the field. The expected noise level at the same location is plotted as the black dashed line. Solid lines indicate the ratio of the two quantities.

depend also on the lens redshift. With increasing aperture size the noise term drops more quickly than the signal, so that the signal-to-noise ratio rises, but it flattens off at the largest radii. Note that this definition of  $\Sigma$  does not reflect the potential of the measurement in recovering a characteristic scale. The halo with  $c = 6$ , for example, has a scale radius of  $\theta_s = 79''$ , and consequently the smoothing scale should be much smaller than  $1'$  in spite of the high signal-to-noise ratio  $\Sigma$ . On the other hand, very small apertures with  $R \lesssim 10''$  should be avoided, as the signal-to-noise ratio is low even in the centre and will deteriorate with increasing distance due to the drop in the lensing signal and the rise of the noise.

There is a natural choice for the aperture size: provided that strong lensing phenomena such as arcs are observed, the smoothing scale can be set to the Einstein radius  $\theta_E$ . The main advantage is the following: for an axisymmetric lens, the average convergence within the Einstein radius is unity,

$$\frac{2}{\theta_E^2} \int_0^{2\pi} d\varphi \int_0^{\theta_E} d\theta \theta \kappa(\theta) = 1 \quad (5.38)$$

(cf. Eq. 3.30). Obviously this holds only if the values of the convergence and of the Einstein radius both refer to the same source redshift; unlike the convergence, the size of the Einstein radius cannot be scaled up to more distant source planes by a multiplicative function of the redshift alone, since its growth also depends on the mass distribution of the lens. For a strong lens that is not axisymmetric, [Bartelmann \(1995\)](#) showed that the mean convergence in the region enclosed by the tangential critical line is less than unity. According to Eq. (5.38),  $\Delta\bar{\kappa} < 1$  everywhere, since the mean convergence within the aperture cannot be larger than unity if the aperture radius is the Einstein radius, and the mean convergence in the control annulus is positive. This inequality is of course likely to be broken by noise, but it can aid in understanding the effects of noise and in devising strategies to combat its influence.

## 5.4. Discussion

I have shown how the  $\zeta$ -statistics introduced by Kaiser (1995) and generalised by Schneider & Bartelmann (1997) can be applied to a rectangular field. This implementation permits the construction of a map of the convergence smoothed with a compensated top hat filter. For each point of the map, the smoothed convergence is the difference of the mean convergence inside a circular aperture at that position and the mean convergence across a ‘control annulus’ consisting of the rest of the field, and it is calculated by integrating over the shear in the control annulus. I have derived expressions for the integral kernel weighting the shear. The resolution of the map is limited by the smoothing scale and the source density. While the signal improves as the aperture is tightened, the noise increases. I have argued that the Einstein radius is a good choice for the smoothing scale.

Two simplifications should be noted, both concerning the description of the shear data. First, I have assumed that the shear signal originates from a single source plane, i.e. that all lensed galaxies have the same redshift. Provided that all redshifts are known to an accuracy that is high compared to the variation of the shear with redshift, this is not a severe problem, as shear values can be rescaled to a common redshift using a function which only depends on the lens redshift and cosmological parameters (see Bartelmann & Schneider, 2001, sec. 4.3.2). The noise estimate, however, will be affected.

Second, I have treated the shear as an approximate observable, equal to the expectation value of the ellipticity, with additive contaminations reflecting the intrinsic shapes of the sources. I have assumed that ellipticities can be fed into the  $\zeta$ -statistics or its generalisation, with the intrinsic ellipticities averaging out to some degree depending on the weight function. Strictly this is only valid in the weak lensing limit. The integration domain is the entire field, and therefore strong lensing data are included, unless the aperture masks the strong lensing region. In the strong lensing regime, the expectation value of the ellipticity is the reduced shear:

$$\langle \epsilon \rangle = g = \frac{\gamma}{1 - \kappa}. \quad (5.39)$$

$\gamma$  itself can therefore only be measured in the limit  $\kappa \ll 1$ . The transformation between intrinsic and observed ellipticities is not an addition (e.g. Seitz & Schneider, 1997). As the  $\zeta$ -statistics and its generalisation are designed as integrals over  $\gamma$ , applying them to measured ellipticities without any correction can introduce errors. Note, however, that the steepness of the weight function entails that the effective integration domain is generally considerably smaller than the field, so that large parts of the map will not be affected, even if strongly lensed images are omitted entirely; similarly, if lensed images close to the centre are obscured by the brightest cluster galaxy, the sampling of the integrand may be insufficient only for a few aperture positions which place a strong weight on the affected region. A possible strategy to avoid errors associated with the distinction between shear and reduced shear could be an iterative scheme; as such an implementation is far from simple, it would be a starting point for future work. Since this dissertation is intended to be a proof of concept focusing on a geometric characterisation, I assume in the following that data can be processed in such a way that the  $\zeta$ -statistics can be obtained from measurements with a noise profile similar to the above description.

# 6

## Chapter 6

# Minkowski Functionals as Measures of Galaxy Cluster Morphology

In this chapter I apply Minkowski functionals to excursion sets of the convergence field. Such an analysis has the benefit of being translation- and rotation-invariant. It is not necessary to identify a centre, and axisymmetry is not assumed, so that this approach should be well suited to irregular mass distributions.

I provide a short overview of the definition of Minkowski functionals and their applications in cosmology. To illustrate how a characteristic scale in a density distribution manifests itself in Minkowski functionals, I study simple examples. I predict the expected behaviour of the Minkowski functionals of the convergence estimator introduced in Ch. 5. In order to probe the effects of noise, I construct mock data and discuss the discrepancies to ideal measurements on different scales. I also demonstrate how contaminations of the signal may be avoided, permitting the discrimination between a scale-rich density profile and a power law.

## 6.1. Minkowski Functionals

Minkowski functionals are integral morphological measures that characterise the geometry and topology of spatial patterns. Here I use them to characterise the thresholded convergence field of a cluster lens.

### 6.1.1. Excursion sets

Given a map of the convergence or a related estimator, the excursion set  $E(\kappa_0)$  for a threshold  $\kappa_0$  is defined as the set of all points where the value of the estimator surpasses the threshold:

$$E(\kappa_0) = \{\mathbf{x} | \kappa(\mathbf{x}) \geq \kappa_0\}. \quad (6.1)$$

It can easily be visualised as the region or union of regions enclosed by the contours of equal density  $\kappa_0$ . Excursion sets shrink monotonically as the threshold is raised; the speed of this decrease reflects the steepness of the underlying distribution of values. This relation is familiar from topographic maps, where closely spaced contour lines indicate a steep slope, while larger distances between nested contours imply a shallower relief. For the convergence field of a spherical halo, the excursion set is obviously always a circle. Noisy measurements cannot be expected to conform to this symmetry – noise may cause a connected region to break up, or add additional, disconnected regions to the excursion set. Thus statistics of the density field are encoded in the morphology of its excursion sets.

### 6.1.2. Definition and properties of Minkowski functionals

The mathematical background of Minkowski functionals and their role in integral geometry is explored in detail in [Mecke et al. \(1994\)](#). Here I only sketch important properties that are relevant to the application described below.

Hadwiger's theorem ([Hadwiger, 1957](#)) states that any additive, translation- and rotation-invariant and conditionally continuous functional in  $d$  dimensions is a linear combination of the  $d+1$  Minkowski functionals. Then in two dimensions there are three Minkowski functionals, labelled  $M_0$ ,  $M_1$  and  $M_2$ , which 'specify the content, shape and connectivity of spatial sets' ([Mecke et al., 1994](#)). The first Minkowski functional is the area, the second the boundary length and the third the Euler characteristic (closely linked to the genus).

Consider two domains  $U$  and  $V$ . As Minkowski functionals are additive, the Minkowski functional of the union  $U \cup V$  is

$$M_\alpha(U \cup V) = M_\alpha(U) + M_\alpha(V) - M_\alpha(U \cap V) \quad (\alpha = 0, 1, 2). \quad (6.2)$$

In particular, if  $U$  and  $V$  are disjoint ( $U \cap V = \{\}$ ),  $M_\alpha(U \cup V) = M_\alpha(U) + M_\alpha(V)$  is simply the sum of the Minkowski functionals of the constituents. Furthermore, let  $g$  be a translation or rotation. Then

$$M_\alpha(gU) = M_\alpha(U) \quad (\alpha = 0, 1, 2), \quad (6.3)$$

i.e. the Minkowski functional does not depend on position or orientation.

In the case of excursion sets, the first two Minkowski functionals can be illustrated as the area enclosed by a contour and its length. The third functional is somewhat less intuitive; a very rough description is that it compares the number of components to the number of holes.

Examples of applications of Minkowski functionals in statistical physics were provided by [Mecke \(2000\)](#). Several authors have demonstrated their importance for the analysis of random fields in cosmology. Unlike the power spectrum, the statistical properties encoded in the Minkowski functionals are not restricted to the two-point correlation function. Information from higher orders can otherwise only be accessed through measurements of the bispectrum, trispectrum etc. As the Minkowski functionals of Gaussian random fields can be calculated analytically (e.g. [Schmalzing & Buchert, 1997](#)), non-Gaussian signatures can be extracted ([Pratten & Munshi, 2012](#)). [Kerscher et al. \(1997\)](#) used Minkowski functionals to characterise a cluster catalogue and found evidence for a cosmological constant; similarly, [Matsubara & Szalay \(2001\)](#) and [Hikage et al. \(2003\)](#) studied the clustering of galaxies in the Sloan Digital Sky Survey, and [Blake et al. \(2014\)](#) measured the distance-redshift relation using the topology of the large-scale structure as a standard ruler. Minkowski functionals have also been applied to the weak lensing field, e.g. by [Matsubara & Jain \(2001\)](#); [Sato et al. \(2001\)](#); [Shirasaki et al. \(2012\)](#); [Petri et al. \(2013\)](#) and [Kratochvil et al. \(2012\)](#), who pointed out the power of Minkowski functionals to constrain the dark energy equation of state. Another important application has been the detection of non-Gaussianities in the CMB, e.g. by [Winitzki & Kosowsky \(1998\)](#); [Schmalzing & Gorski \(1998\)](#); [Novikov et al. \(1999\)](#); [Schmalzing et al. \(2000\)](#); [Hikage et al. \(2006, 2008\)](#); [Matsubara \(2010\)](#).

### 6.1.3. Predictions for the NFW profile

For haloes with spherically symmetric density distributions like the NFW profile or the isothermal sphere model, the calculation of the Minkowski functionals is simple. The convergence is a strictly decreasing function of the radius. Consequently, the excursion set for any threshold  $\kappa_0$  is a circle the radius  $\theta_0$  of which is defined by  $\kappa(\theta_0) = \kappa_0$ . The first Minkowski functional, the area, is therefore  $M_0(\kappa_0) = \pi\theta_0^2$ , and the second is the perimeter of the circle, i.e.  $M_1(\kappa_0) = 2\pi\theta_0$ . The third Minkowski functional is of no great interest here, but for completeness I note that the Euler characteristic of a disk is unity.

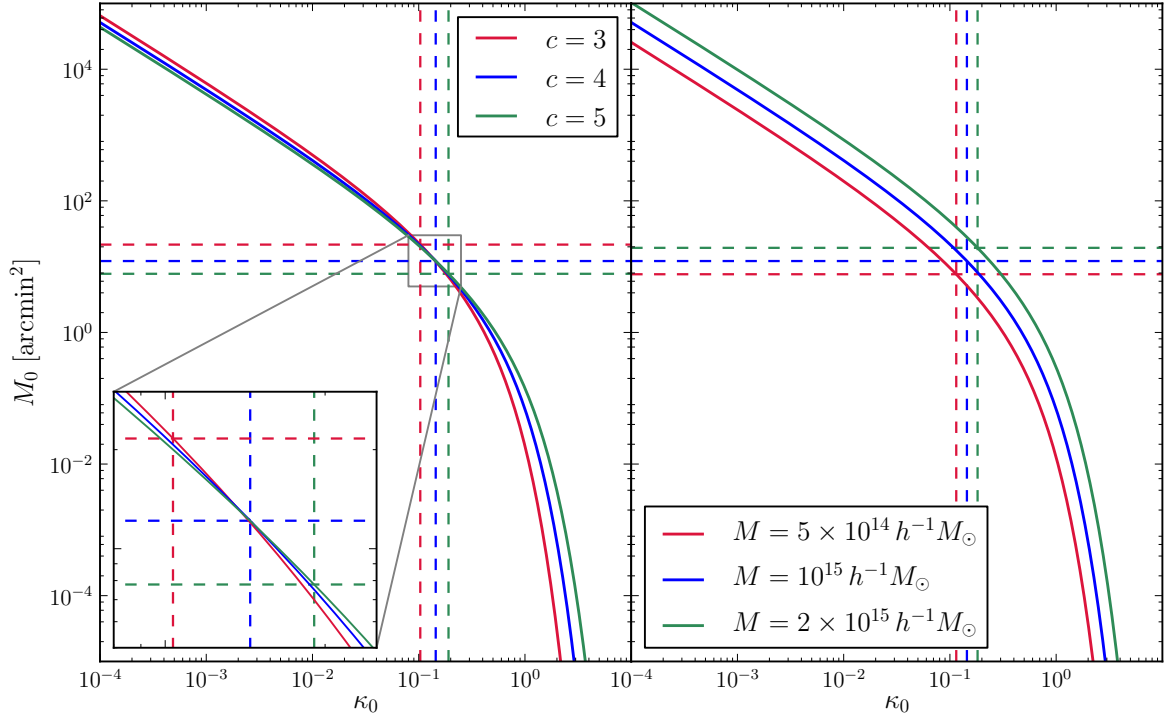


**Figure 6.1.:** The first Minkowski functional  $M_0$  of the convergence as a function of the excursion set threshold  $\kappa_0$  for NFW haloes of the same mass ( $M = 10^{15} h^{-1} M_\odot$ ; left panel) or concentration ( $c = 4$ ; right panel), respectively. For each halo the dashed lines of the same colour indicate the values corresponding to the scale radius  $r_s$ , i.e.  $\kappa_0 = 2/3\kappa_s$  and  $M_0 = \pi r_s^2$ .

Examples for the first Minkowski functional in the case of NFW haloes are shown in Fig. 6.1, from which it is evident that  $\ln M_0(\ln \kappa_0)$  is a concave function. For low thresholds  $\kappa_0 \ll \kappa_s$ , corresponding to radii much larger than the scale radius, the logarithmic slope is nearly constant, with  $d \ln M_0 / d \ln \kappa_0 \rightarrow -1$  for  $\kappa_0 \rightarrow 0$ . As  $\kappa_0$  increases, however, the curves begin to drop more steeply, reaching a value of  $d \ln M_0 / d \ln \kappa_0 \rightarrow -5/3$  at the scale radius ( $\kappa_0 = 2/3\kappa_s$ ), irrespective of the profile parameters. At a fixed mass, the behaviour is similar at low thresholds, but the point at which the slope begins to decrease visibly depends on the concentration – the higher the concentration, the smaller the scale radius, and the higher the threshold  $\kappa_0$  at which the steeper decrease sets in. If the concentration is kept fixed, an increase in the mass raises the value of  $M_0$  for all thresholds.

## 6.2. Application to the $\zeta$ -Statistics

The approach described in the previous section is applied to the smoothed convergence  $\Delta \bar{\kappa}$  introduced in Ch. 5. I aim to test if an intrinsic characteristic scale of a simple mass distribution can be recovered from lensing data. To that end, I generate mock measurements for NFW haloes.

### 6.2.1. Generation of mock data

I create a source distribution as follows: the source density is set to  $n = 30 \text{ arcmin}^{-2}$ , typical for ground-based telescopes, and galaxies are distributed uniformly across a square field of  $20'$  side length. Similar or larger field sizes in the range  $20' - 30'$  are achieved e.g. by the Suprime-Cam on the Subaru telescope (Miyazaki et al., 2002) or the Large Binocular Cameras (Giallongo et al., 2008). The virial radii of galaxy clusters are typically of the order of  $1 - 2 h^{-1} \text{ Mpc}$ , corresponding to  $5' - 10'$  at a redshift of  $z = 0.3$ , so that most clusters are well contained in such a field of view. To account for shape noise,

intrinsic ellipticities are assigned to the sources. The absolute value  $|\epsilon_s|$  is drawn from a Rayleigh distribution,

$$p(|\epsilon_s|) d\epsilon_s = \frac{2|\epsilon_s|}{\sigma_\epsilon^2 [1 - \exp(-1/\sigma_\epsilon^2)]} \exp\left(-\frac{|\epsilon_s|^2}{\sigma_\epsilon^2}\right) d\epsilon_s, \quad (6.4)$$

restricted to  $|\epsilon_s| \in [0, 1]$ . The dispersion is set to  $\sigma_\epsilon = 0.3$ . A random position angle  $\alpha$  is drawn from a uniform distribution on the interval  $[0, \pi]$ . The intrinsic ellipticity is  $\epsilon_s = |\epsilon_s|e^{2i\alpha}$  in the complex notation.

A redshift of  $z_d = 0.3$  is chosen for the lens and all sources are assumed to be at the same redshift of  $z_s = 2.0$ . The ellipticity of the lensed image is calculated by adding the shear  $\gamma$  (see Sec. 5.4 for the limitations of this approach). Expressions for the convergence and shear of the NFW profile were derived by Bartelmann (1996) and Wright & Brainerd (2000):

$$\kappa(x) = \frac{2\kappa_s}{x^2 - 1} [1 - f(x)], \quad (6.5)$$

$$\gamma_T(x) = \kappa(x) - \frac{4\kappa_s}{x^2} \left[ \ln \frac{x}{2} + f(x) \right], \quad (6.6)$$

where

$$f(x) = \begin{cases} \frac{2}{\sqrt{x^2-1}} \arctan \sqrt{\frac{x-1}{x+1}} & \text{if } x > 1 \\ \frac{2}{\sqrt{1-x^2}} \operatorname{artanh} \sqrt{\frac{1-x}{1+x}} & \text{if } x < 1 \\ 1 & \text{if } x = 1 \end{cases}. \quad (6.7)$$

The dimensionless radius  $x = \theta/\theta_s$  is the distance  $\theta$  from the lens centre divided by the angular scale  $\theta_s$  corresponding to the scale radius. The cross-component  $\gamma_X$  of the shear vanishes. The two components of the shear in a Cartesian coordinate system, or the real and imaginary parts in the complex plane, are

$$\gamma_+ = -\gamma_T \cos 2\phi, \quad \gamma_\times = -\gamma_T \sin 2\phi, \quad (6.8)$$

where  $\phi$  is the azimuthal angle measured with respect to the lens centre.

The resulting catalogue of galaxy positions and image ellipticities is then used as the input for the  $\zeta$ -statistics.

## 6.2.2. Examples

I choose to study two NFW haloes as examples. Both have the same mass of  $M = 10^{15} h^{-1} M_\odot$ ; the concentrations are  $c = 4$  and  $c = 6$ , respectively. I construct maps of the smoothed convergence  $\Delta\bar{\kappa}$  as outlined in Sec. 5.3. The smoothing scale is the Einstein radius for each halo. For a source redshift of  $z_s = 2.0$  these are  $\theta_E = 14.6''$  for  $c = 4$  and  $\theta_E = 26.9''$  for  $c = 6$ . I calculate the convergence on a grid of  $400 \times 400$  pixels – this is somewhat arbitrary, as the resolution is in fact limited by the mean distance between sources and the smoothing scale, which are both considerably larger than the diameter of a pixel in this case.

I compute the first Minkowski functional by identifying and counting the pixels in which  $\Delta\bar{\kappa}$  exceeds the threshold for the excursion set. For comparison I also derive theoretical predictions: I use a fast Fourier transform to calculate the convolution of the convergence of the lens, given by Eq. (6.5), with the filter from Eq. (5.30), constructing a noise-free map of the same size and resolution as the mock measurements, for which I also calculate the first Minkowski functional. These predictions differ somewhat from the examples given in Sec. 6.1.3: first, they characterise the smoothed convergence field, so the excursion set is empty for thresholds  $\kappa_0 \geq 1$ ; second, while the plots shown in Fig. 6.1 display the asymptotic behaviour  $d \ln M_0 / d \ln \kappa_0 \rightarrow -1$  for  $\kappa_0 \rightarrow 0$ , the predicted Minkowski functional for  $\Delta\bar{\kappa}$  flattens off at low thresholds because it is bounded by the field size – once the circles grow too

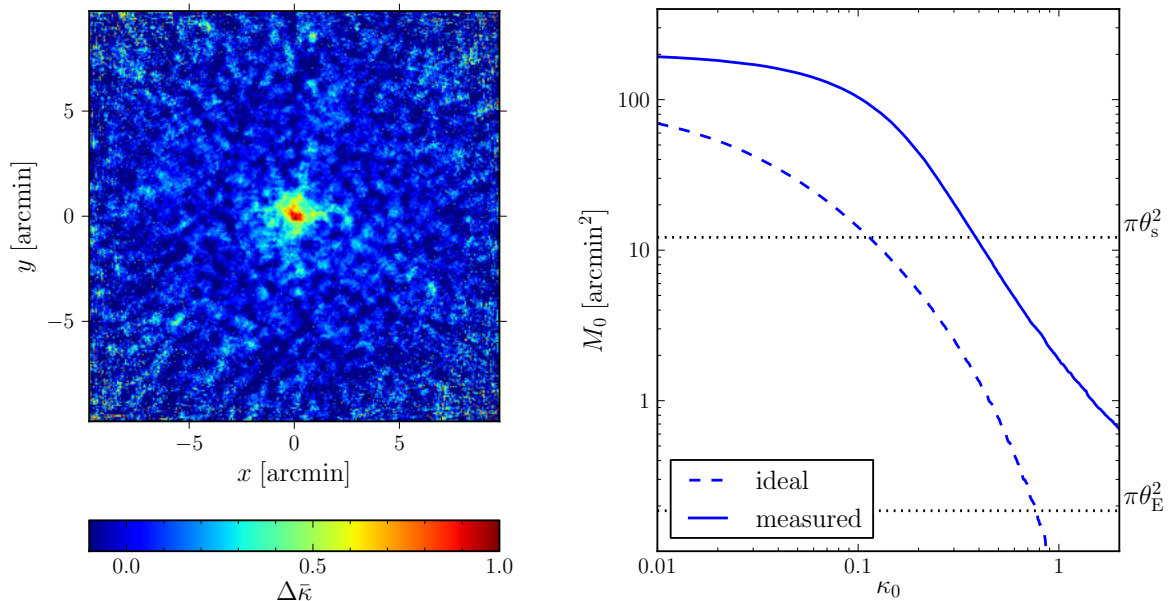


**Figure 6.2.:** Map and first Minkowski functional of the smoothed convergence  $\Delta\bar{\kappa}$  for an NFW halo with  $c = 4$  and  $M = 10^{15} h^{-1} M_{\odot}$ .

large to be fully contained in the square field, the logarithmic slope decreases (by absolute value) until the curve plateaus when the excursion set is simply the entire field.

Maps of the smoothed convergence and the measured and predicted Minkowski functionals are shown in Figs. 6.2 and 6.3. The difference in the correlation length can clearly be seen: for the larger aperture radius, i.e. the halo with  $c = 6$ , the map appears smoother, as if ‘blurred’, compared to the grainy structure in the case  $c = 4$ . As predicted in Sec. 5.3.2, the outskirts are most strongly affected by noise. For  $c = 6$ , this region is restricted mostly to the corners, whereas correlations dominate across most of the field, but for  $c = 4$ , outliers can be found much closer to the centre.

The Minkowski functionals are consistently overestimated in both examples. Moreover, the curves are not concave. The deviations are stronger for the smaller concentration. I discuss their origins in the next section.

## 6.3. Noise

Considerable discrepancies exist between the measured Minkowski functional derived from mock data and the ideal curve predicted from the density profile of the lens. In the following I demonstrate how these deviations arise and suggest strategies to minimise the contamination.

### 6.3.1. Tests

Before discussing in detail how noise affects the measurement on different scales, I perform a simple test to verify the validity of the approach in general.

The shot noise vanishes in the limit  $n \rightarrow \infty$ . I construct source distributions with higher galaxy densities to test this limit. The results are shown in the left panel of Fig. 6.4. While the agreement between the curves improves with an increasing number of sources, discrepancies remain even for  $n = 1000 \text{ arcmin}^{-2}$ . Next I set the intrinsic ellipticities to zero ( $\sigma_{\epsilon} = 0$ ), so that any remaining noise is exclusively due to the spatial distribution of the galaxies. The right panel of Fig. 6.4 shows that the ideal curve is reproduced much better in this case, even for  $n = 30 \text{ arcmin}^{-2}$ .

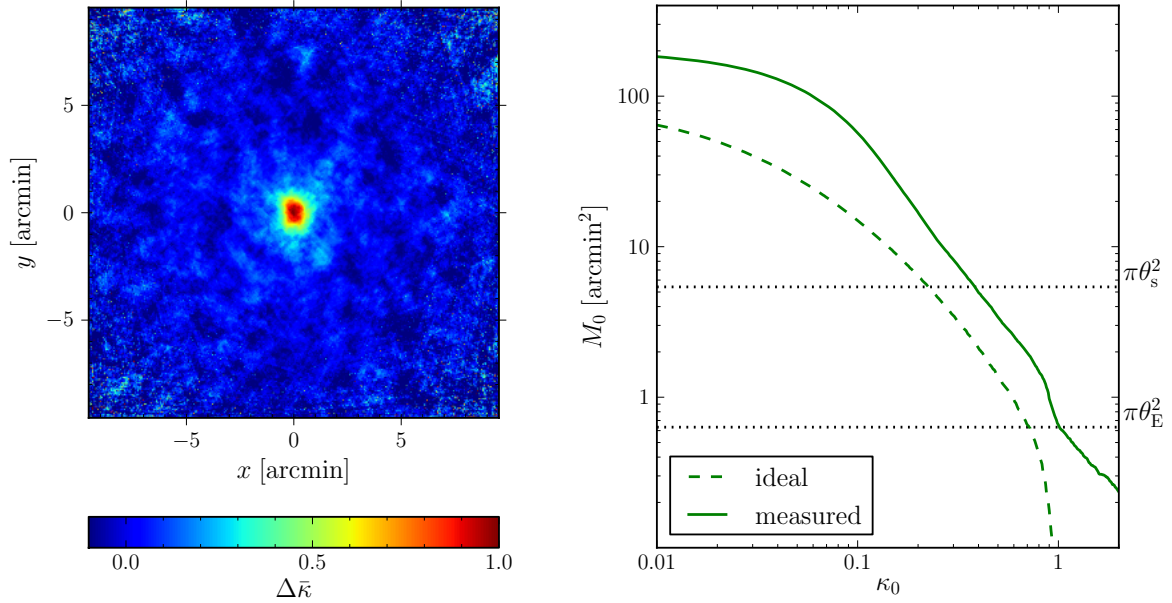


Figure 6.3.: As Fig. 6.2, but for a halo with  $c = 6$ .

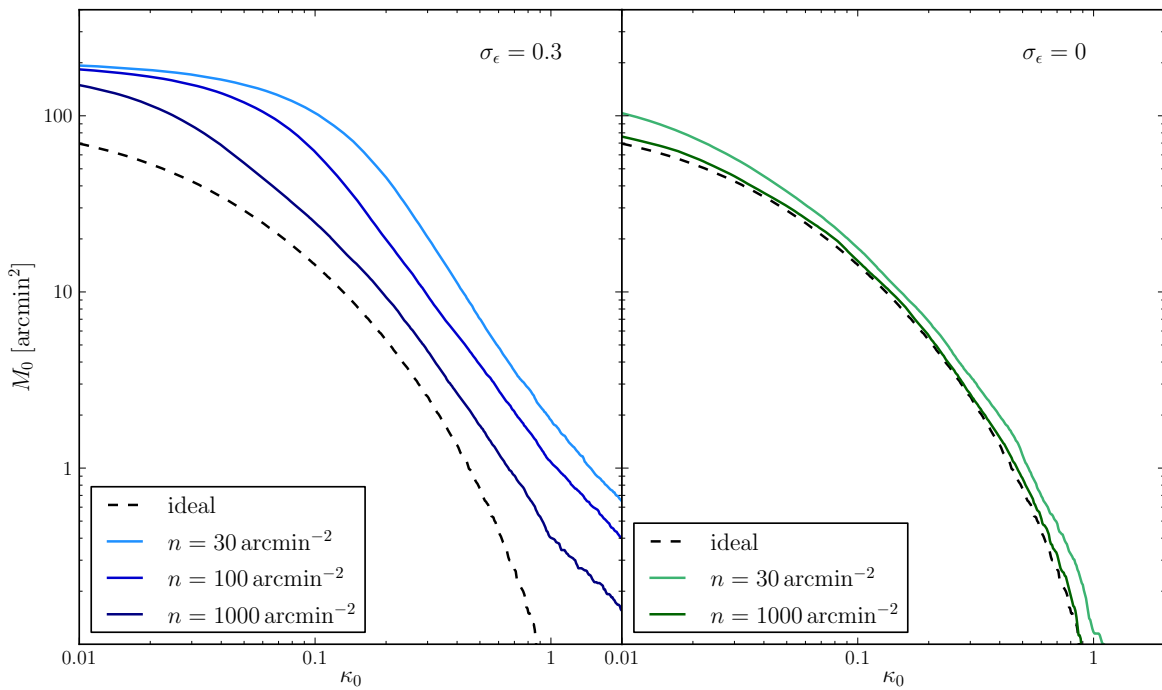


Figure 6.4.: Minkowski functional  $M_0(\kappa_0)$  of the  $\zeta$ -statistics for different source densities  $n$ . The right panel illustrates a simulated measurement with spherical rather than elliptical sources.

The behaviour of a noisy curve can to some extent be predicted theoretically. The Minkowski functional is the number of pixels above the threshold  $\kappa_0$  and can be written as a sum over the Heaviside function at the grid points:

$$M_0(\kappa_0) = \sum_{i=1}^N \Theta [k(\mathbf{x}_i) - \kappa_0]. \quad (6.9)$$

A prefactor could be inserted depending on the normalisation. The Heaviside function reflects that the Minkowski functional is calculated simply by comparing pixel values to the threshold and counting. If  $M_0(\kappa_0)$  is averaged over a sufficiently large number of realisations of the source distribution, the result should be the expectation value

$$\langle M_0(\kappa_0) \rangle = \sum_{i=1}^N \langle \Theta [k(\mathbf{x}_i) - \kappa_0] \rangle. \quad (6.10)$$

$\langle \Theta [k(\mathbf{x}_i) - \kappa_0] \rangle$  is the probability that  $k(\mathbf{x}_i) > \kappa_0$ ; as the measurement  $k(\mathbf{x}_i)$  is the sum of the true value  $\Delta\bar{k}(\mathbf{x}_i)$  and a spurious contribution  $\delta(\mathbf{x}_i)$ , this can be re-interpreted as the probability that  $\delta(\mathbf{x}_i) > \kappa_0 - \Delta\bar{k}(\mathbf{x}_i)$ . The statistical distribution of the errors  $\delta(\mathbf{x}_i)$  depends on the aperture position  $\mathbf{x}_i$ . I assume for simplicity that it is Gaussian with the variance  $\sigma_\kappa^2(\mathbf{x}_i)$  given by Eq. (5.37). Neighbouring pixels are evidently strongly correlated, but as the calculation of the covariances is numerically expensive, I neglect them for this demonstration of the noise structure. In this approximation, the probability for a measurement to surpass the threshold is given by a complementary error function:

$$\langle \Theta [k(\mathbf{x}_i) - \kappa_0] \rangle = \frac{1}{2} \operatorname{erfc} \left[ \frac{\kappa_0 - \Delta\bar{k}(\mathbf{x}_i)}{\sqrt{2}\sigma_\kappa(\mathbf{x}_i)} \right]. \quad (6.11)$$

The evaluation of this expression at all grid points permits the construction of a predicted curve. If  $\Delta\bar{k}(\mathbf{x})$  is set to zero everywhere, the result characterises the noise. Figure 6.5 demonstrates that the noise contribution is symmetric, i.e. positive and negative deviations are equally likely. At  $\kappa_0 = -1.0$  the excursion set comprises almost the entire field, and conversely it is almost empty for  $\kappa_0 = +1.0$ , indicating that such high deviations are unlikely given the noise profile. The Minkowski functional is a shallow function for  $\kappa_0 \lesssim -0.2$  and  $\kappa_0 \gtrsim 0.2$ , with a steep drop between these thresholds. This agrees with the observations of Sec. 5.3.2: the noise level is almost constant at this order of magnitude across much of the field and rises sharply only near the corners.

### 6.3.2. Noise at high and low Thresholds

I have argued in Sec. 5.3.3 that  $\Delta\bar{k} < 1$  must hold if the smoothing scale equals the Einstein radius of the lens. This condition is obviously violated in Figs. 6.2 and 6.3: the Minkowski functional  $M_0(\kappa_0)$  is still finite at  $\kappa_0 = 2$ . As the behaviour at such high thresholds can only be due to noise, it is not itself relevant for the analysis. Yet it is reasonable to strive to understand it, rather than exclude these thresholds altogether, since the same source of noise is likely to affect the results also at somewhat lower values of  $\kappa_0$ . Looking at the convergence maps in Figs. 6.2 and 6.3, it seems likely that isolated pixels close to the edges of the field are the main contributors. While the actual density in the outskirts is very low, the steep increase of the variance towards the borders results in a large number of outliers.

The large variations close to the borders also manifest themselves in the positive bias of the measured Minkowski functional at very low thresholds. Without noise, the excursion set area at  $\kappa_0 = 0.01$  is roughly 15–20 per cent of the field. As the convergence profile is marked by very low values and a very shallow slope at large distances from the lens centre,  $\Delta\bar{k}$  is small or even slightly negative across much of the field, and the ideal excursion set comprises only a relatively small central region even for low  $\kappa_0$ . The measured curve begins at nearly 50 per cent (200 arcmin<sup>2</sup>) of the field at  $\kappa_0 = 0.01$ . The same can be observed in a predicted curve based on Gaussian noise for each pixel (cf. Fig. 6.7). At first this may seem surprising, since at least in the case of a Gaussian positive and negative errors are

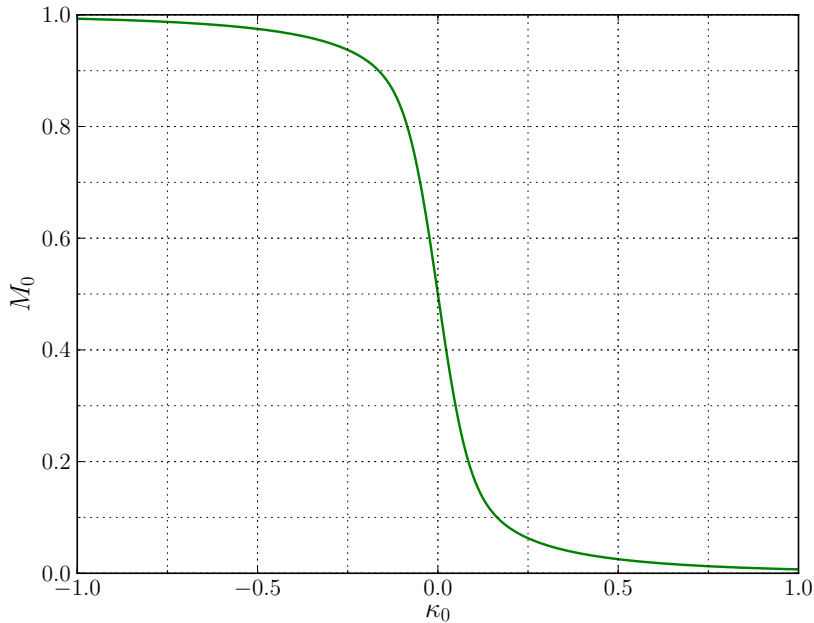


**Figure 6.5.:** Minkowski functional  $M_0$  of the  $\zeta$ -statistics of an empty field, illustrating the noise characteristics. The smoothing scale of  $\theta_E = 26.9''$  is the Einstein radius of an NFW halo with  $M = 10^{15} h^{-1} M_\odot$  and  $c = 6$ . The Minkowski functional is given as a fraction of the total field size, which is  $400 \text{ arcmin}^2$ .

equally likely and the contributions to the Minkowski functional might be expected to average out. To understand this bias, it is helpful to consider the ideal and measured values along a single scan of the map, close to the centre of the lens (Fig. 6.6); note the strong correlations between neighbouring measurements. The ideal profile is mostly flat, with a sharp peak in the centre. At low thresholds (e.g.  $\kappa_0 = 0.02$  in Fig. 6.6),  $\Delta\bar{\kappa} < \kappa_0$  for much of the scan, but the difference is very small. It is thus very likely that noise will add pixels to the excursion set, especially since the variance is highest towards the edges. On the other hand, the section with  $\Delta\bar{\kappa} > \kappa_0$  is quite narrow; the profile is steep and the variance low, so that it is unlikely that pixels will be removed from the excursion set due to noise contributions. Thus on average the net effect of noise is the growth of the excursion set at low thresholds. The bias decreases once the difference between  $\kappa_0$  and the convergence level in the shallow parts is large compared to the typical variance.

These two discrepancies are not difficult to remove: as little information can be gained from the density profile at these large radii, a simple solution is to restrict the convergence map to a region smaller than the field covered by the shear catalogue. This is demonstrated in Fig. 6.7 (left panel): pixels in which the variance  $\sigma_\kappa$  exceeds a limit are excluded from the calculation of the Minkowski functional. This masking strategy means that the field is effectively cut along a contour line of equal variance (cf. Fig. 5.4). The agreement between measured and ideal curves is improved immensely for  $\kappa_0 \gtrsim 0.2$ , but strong deviations remain for the lower thresholds. These cannot be reduced in this approach: the most restrictive variance limit in Fig. 6.7 is  $\sigma_{\max} = 0.1$ , and Fig. 5.4 shows that this cut-off already rules out a considerable fraction of the field. Due to the shallow noise profile at this level, lowering the limit further reduces the size of the usable field enormously and eventually interferes with the signal.

### 6.3.3. Noise at the scale radius

A notable feature in the measured curves, which persists when the regions close to the borders are excluded, is the rather abrupt approach of the measured curve to the ideal, occurring roughly at  $\kappa_0 \sim 0.2$ . This can also be observed in the behaviour predicted from Eq. (6.11): the curve in the right panel

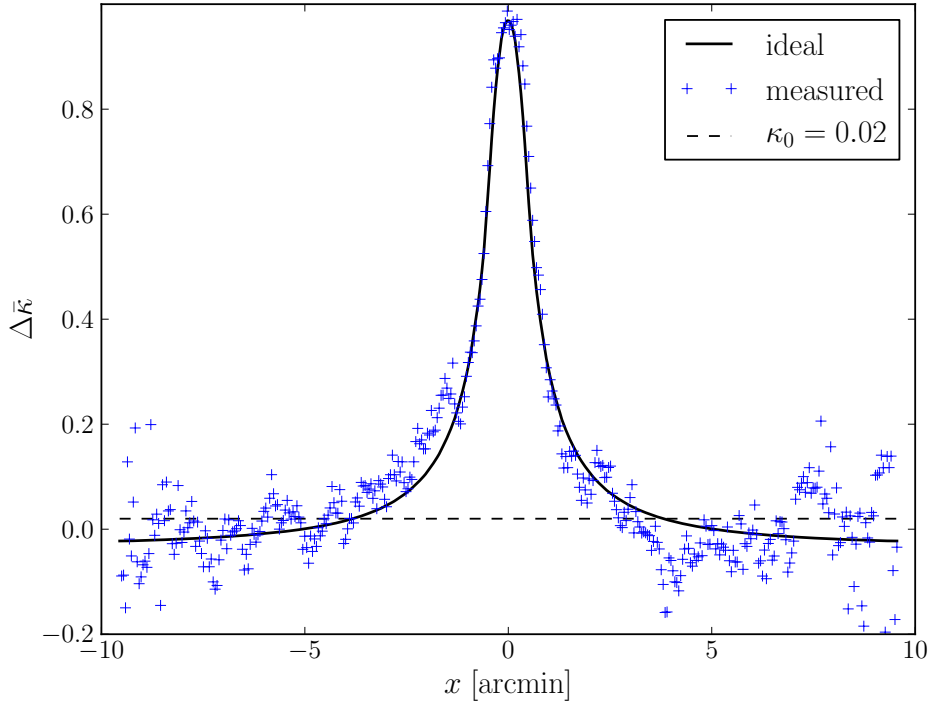


**Figure 6.6.:** Measured and ideal convergence values along a single row of the map for the  $c = 6$  halo. The dashed line represents an excursion set threshold: the first Minkowski functional measures the number of points above this line.

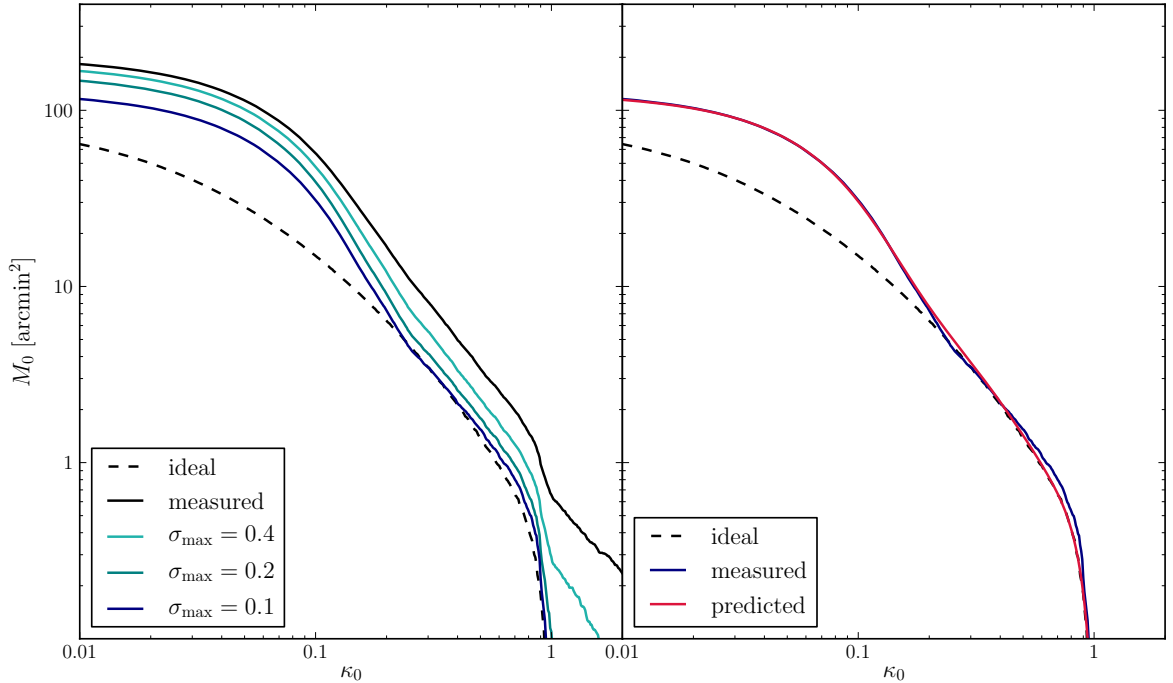


**Figure 6.7.:** First Minkowski functional  $M_0(\kappa_0)$  of the  $\zeta$ -statistics for different variance limits. The expected variance is calculated for each grid point and pixels with  $\sigma_\kappa > \sigma_{\max}$  are excluded. The solid black line is the measurement without any variance cuts. The dashed line illustrates an ideal (noise-free) measurement. In the right panel,  $\sigma_{\max} = 0.1$ ; the expectation value for a noisy measurement is plotted in red. The lens is an NFW halo with  $c = 6$  and  $M = 10^{15} h^{-1} M_\odot$ .

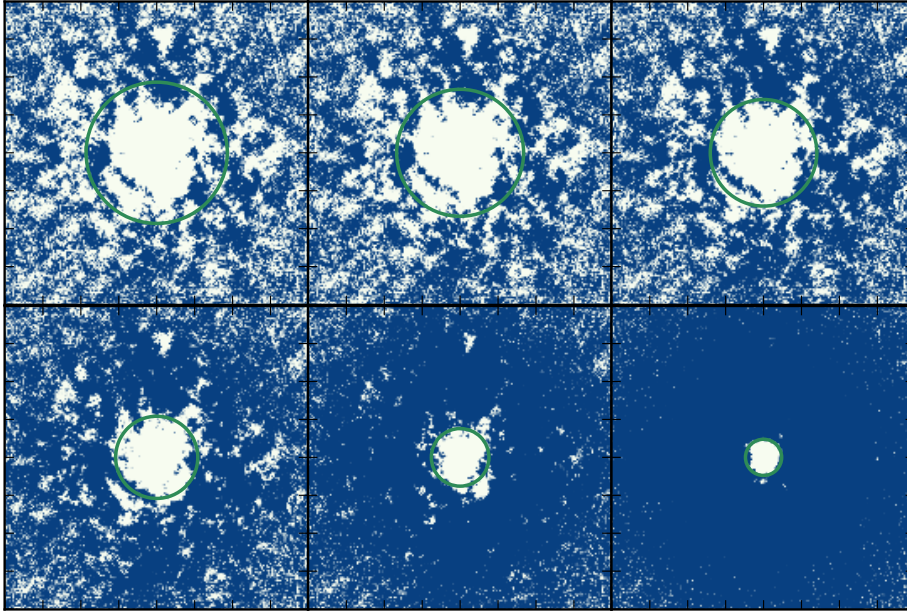


**Figure 6.8.:** Illustration of the excursion sets at different thresholds  $\kappa_0$ , from top left to bottom right:  $\kappa_0 = 0.008$ ;  $\kappa_0 = 0.016$ ;  $\kappa_0 = 0.032$ ;  $\kappa_0 = 0.064$ ;  $\kappa_0 = 0.128$ ;  $\kappa_0 = 0.256$ . The green circle in each image marks the circumference of the ideal excursion set of the NFW halo ( $c = 6$ ,  $M = 10^{15} h^{-1} M_\odot$ ) at the same threshold.

of Fig. 6.7 shares the most striking features of the measured curves: the overestimation of  $M_0$  at the lowest thresholds, and a relatively steep drop of the measured curve towards the ideal.

To illustrate the evolution of the excursion set at these thresholds, I plot the thresholded convergence field of the halo with  $c = 6$  in this range in Fig. 6.8. It is notable that the excursion sets for the lower thresholds consist of several larger regions as well as many isolated pixels and small groups, the latter found particularly close to the edges. This is consistent with the observations about the correlation length made in Sec. 5.3.2. As the threshold is raised, isolated pixels and pixels on the boundaries of connected regions disappear, but the general structure remains similar. Between  $\kappa_0 = 0.032$  and  $\kappa_0 = 0.128$ , however, the connected regions shrink substantially – the drop of the Minkowski functional marks this sharp decrease. Finally, for  $\kappa_0 = 0.256$  the excursion set matches the expected disk of the underlying NFW profile quite well, apart from the remaining isolated pixels in the outskirts.

Based on this behaviour, a reduction of the noise contribution at intermediate thresholds seems achievable through segmentation. Given the excursion set for a fixed threshold, I identify connected regions and determine their size. Two pixels are classified as connected if they share an edge, but not if only their corners touch – the latter definition of connectivity would generally increase component size and decrease the number of connected regions, which is unwanted. Figure 6.9 shows histograms of the component size for different thresholds. The distribution is extremely steep (note the logarithmic ranges) – by far the most components consist of only a few or even a single pixel, whereas the number of large regions is much lower. This reflects the high number of isolated pixels and small groups observed in Fig. 6.8.

The difference between the largest region and the next in size is generally substantial. It is easy to guess, and to check, that the largest region is always the one in, or closest to, the lens centre. A slight offset may occur at very high thresholds, when the excursion set is very small and noise may cause a slight shift away from the true centre, but it is extremely unlikely that the size of regions that do not include the peak of the signal exceeds that of the central component due to the correlated noise profile. As the size of the largest component should be a much better estimator of the ideal value of the Minkowski functional than the measure of the full excursion set, I ignore all smaller regions and plot

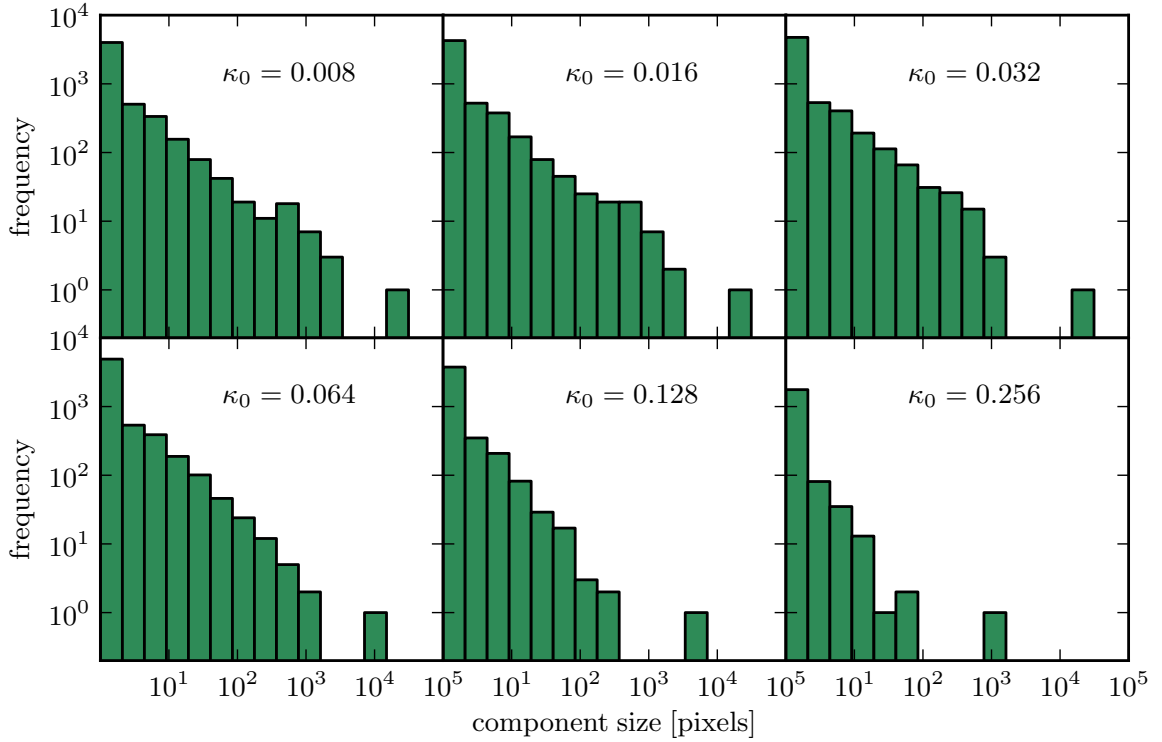


**Figure 6.9.:** Histograms of the sizes of connected components of the excursion set at different thresholds  $\kappa_0$ .

the resulting Minkowski functional in Fig. 6.10. The agreement between the measured values and the ideal curve is indeed much better, in particular at the relatively high thresholds at which the influence of the scale radius becomes evident.

## 6.4. Discrimination between NFW and Power Law Profiles

In the previous section I have developed a strategy to reduce noise contributions to the measured Minkowski functionals. In the following I apply this strategy to probe if a density distribution marked by a characteristic scale can reliably be distinguished from a scale-free profile.

### 6.4.1. Gravitational lensing by a power law profile

For a halo with a spherically symmetric density distribution  $\rho(r) \sim r^{-a}$ , the convergence and shear fields are naturally also described by power laws:

$$\kappa(\theta) = \frac{4-a}{4} \left( \frac{\theta}{\theta_E} \right)^{-a/2}, \quad |\gamma|(\theta) = \frac{a}{4} \left( \frac{\theta}{\theta_E} \right)^{-a/2}. \quad (6.12)$$

As for any axisymmetric mass distribution, the shear is tangential. A lens is characterised solely by its Einstein radius  $\theta_E$  and the exponent  $a$ . A specific instance is the singular isothermal sphere (SIS), which has the density

$$\rho(r) = \frac{\sigma_v^2}{2\pi G r^2}, \quad (6.13)$$

i.e.  $a = 2$ . The SIS model reproduces the flat rotation curves observed in galaxies, but it is frequently used to describe the mass distributions of dark matter haloes also on other scales, including galaxy

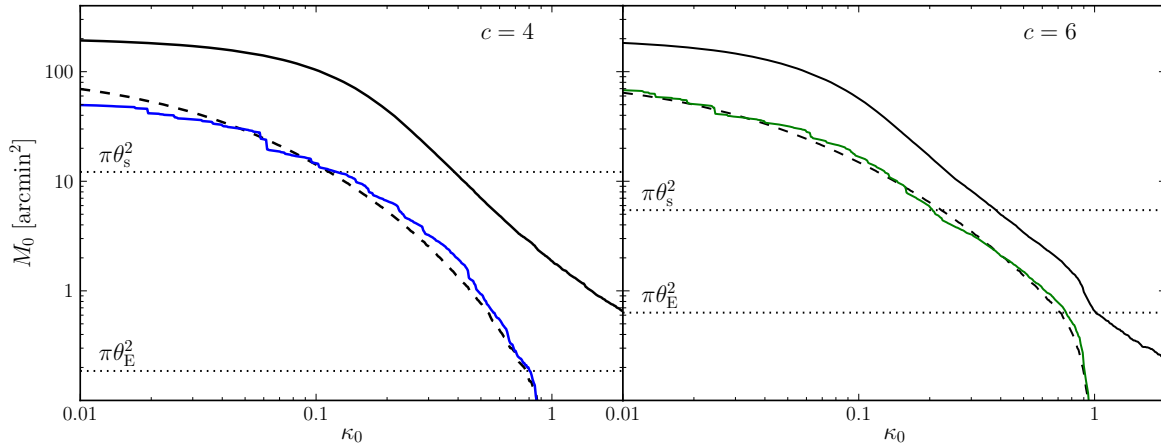


**Figure 6.10.:** First Minkowski functional  $M_0$  of the largest connected component of the excursion set as a function of the threshold  $\kappa_0$ . Solid black lines indicate the original measurements (before segmentation; cf. Figs. 6.2 and 6.3), dashed lines the ideal results. The mass of both haloes is  $M = 10^{15} h^{-1} M_\odot$ .

clusters.  $\sigma_v$  is the velocity dispersion of the stars or cluster members, respectively. The NFW profile has the same logarithmic slope of  $-2$  at its scale radius, but it is shallower than the SIS at small radii and steeper at large radii.

The left panel of Fig. 6.11 shows the ideal Minkowski functionals of  $\Delta\bar{\kappa}$  for the NFW halo with  $c = 4$  and an SIS which has the same Einstein radius of  $\theta_E = 14.6''$ . Due to the power law profile, the SIS curve has a constant slope of  $-2$  almost up to the smoothing scale. Both curves share the same bounds, with the excursion set approaching the field size for very small thresholds  $\kappa_0$  and shrinking rapidly for  $\kappa_0 \rightarrow 1$ , but between these limits the behaviour is clearly different. This is illustrated in the right panel of Fig. 6.11, where the distance between the two curves is plotted as function of the threshold; as the Minkowski functional is plotted on a logarithmic scale, this distance measures the ratio of the quantities. The location of the maximum depends on the concentration, moving to higher  $\kappa_0$  as  $c$  increases, whereas the height of the peak decreases. The Minkowski functional of the NFW halo is higher than its SIS counterpart by a factor of approximately 2 for  $c = 5$  and more than 10 for  $c = 3$ . This rise in significance with increasing concentration can be attributed to the growing ratio of the scale radius to the Einstein radius - the smoothing scale is smaller and the characteristic difference in the slope of the density distribution can be observed over a wider range of radii. Based on the agreement between measured and ideal Minkowski functionals demonstrated in Fig. 6.10, the size of this gap suggests that an NFW halo can be distinguished from a power law model in spite of noise contributions to the excursion set.

## 6.4.2. Statistics

Given a set of shear data, consider the null hypothesis that the underlying mass distribution follows a power law, or specifically the SIS profile. One can test this hypothesis by comparing the measured Minkowski functional to the  $M_0$ -characteristic of a singular isothermal sphere which reproduces the observed Einstein radius. An ideal measurement would lead to a curve like those shown in Fig. 6.11, but actual results will be contaminated by noise. Figure 6.10 shows that measured Minkowski functionals are less smooth than the predicted curves. Such fluctuations result in additional peaks of the ratio and a potential shift of the maximum.

To estimate the scatter I generate mock measurements of both the  $c = 4$  NFW halo and an SIS with  $\theta_E = 14.6''$  for 100 realisations of the source distribution. At each threshold  $\kappa_0$  I calculate the mean and the standard deviation. The results are shown in Fig. 6.12. As the measured Minkowski functional is compared to the ideal value for an SIS profile, the ratio should be unity in the case of the

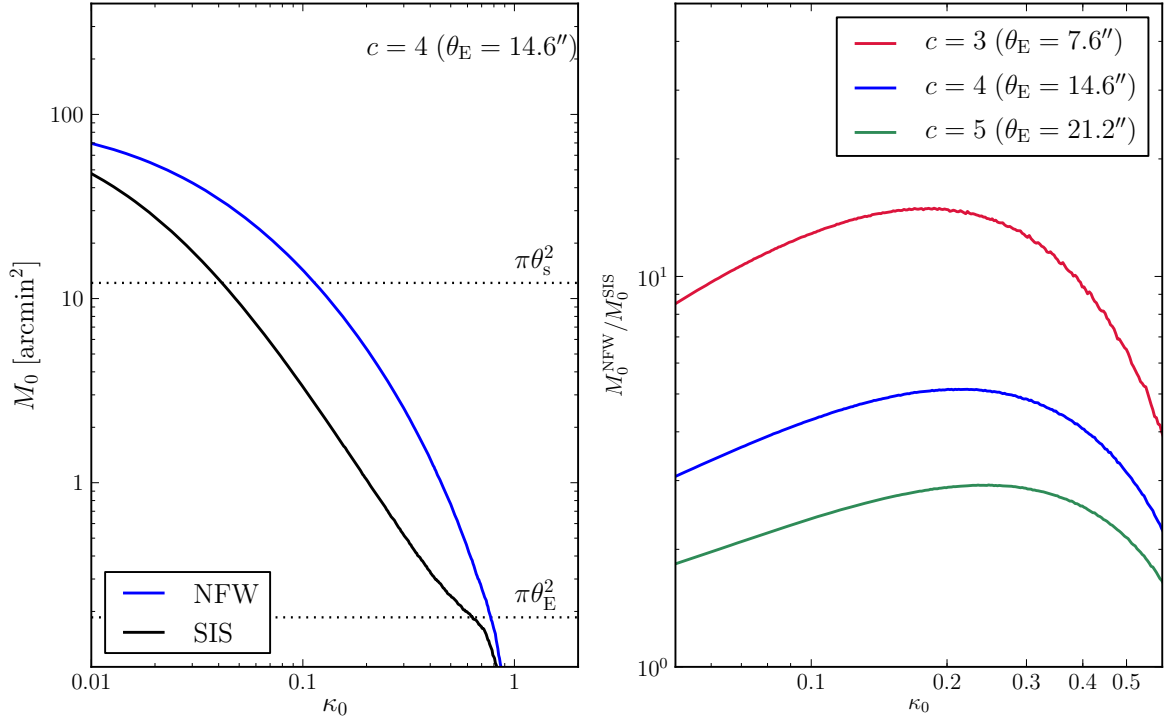


**Figure 6.11.:** Comparison between the Minkowski functionals of the smoothed convergence for NFW and SIS haloes with the same Einstein radius. The left panel shows  $M_0(\kappa_0)$  for NFW and SIS models with  $\theta_E = 14.6''$ . In the right panel, the ratio of the Minkowski functionals for both profiles is plotted for three different Einstein radii.

power law data. In the presence of noise, however, the Minkowski functional is overestimated for both profiles. Despite the scatter, it is clearly possible to distinguish between the two profiles, as the shaded areas representing the standard deviations do not even overlap. Moreover, the variance is remarkably small compared to the difference between curves for different concentrations ( $c = 3, 4, 5$  are shown). This suggests that even a quantitative analysis could be possible, classifying lenses according to the behaviour of the Minkowski functionals.

## 6.5. Discussion

I have presented an integral, translation-invariant analysis of the morphology of a galaxy cluster. The density field is described by the smoothed convergence introduced in Ch. 5. The first Minkowski functional measures the area of the excursion set of this estimator as a function of the threshold. An intrinsic scale in the mass distribution manifests itself in a change of the logarithmic slope of this function. In order to extract such a signature, understanding the influence of noise on the measurement is crucial. Due to the characteristic noise profile of the  $\zeta$ -statistics, the outskirts of the field are most strongly affected. The Minkowski functional is overestimated at all thresholds. I have demonstrated which features of the noise structure are responsible for this effect depending on the range of the threshold. Segmentation is a very effective strategy for noise removal: if only the largest component of the excursion set is measured, the agreement between predictions and results derived from mock data is remarkably good.

Based on this proof of principle, a much larger sample of lenses should be considered, including a wider range of masses, concentrations and redshifts. Asymmetric distributions are typically in tension with the prejudices this approach has been designed to avoid. Therefore less highly symmetric shapes would be worth investigating, such as elliptical extensions of spherical profiles or dark matter haloes

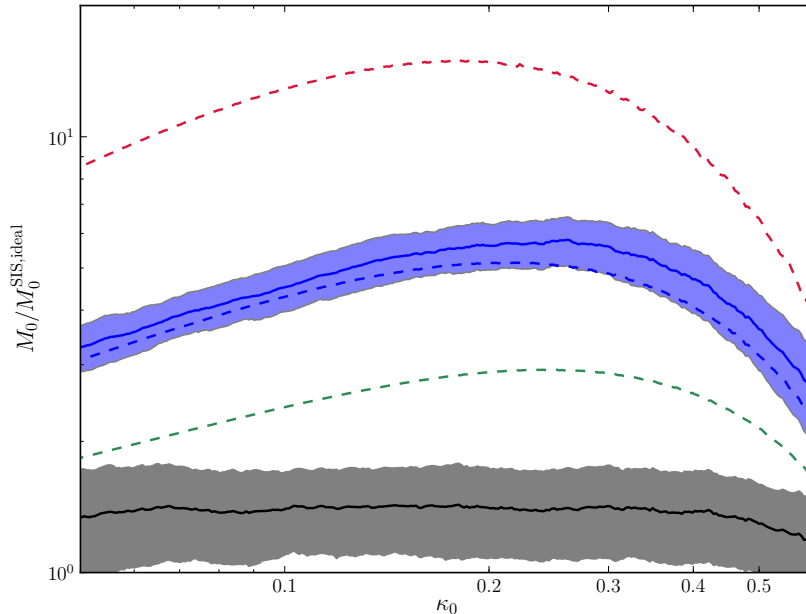


**Figure 6.12.:** Measured Minkowski functional  $M_0(\kappa_0)$  compared to an SIS with the same Einstein radius. Solid lines indicate mock measurements of an NFW (blue) and SIS (black) lens averaged over 100 realisations. Shaded areas correspond to  $\pm 1$  standard deviation. Dashed lines illustrate ideal values for NFW haloes with  $c = 3$  (red),  $c = 4$  (blue) and  $c = 5$  (green) ( $M = 10^{15} h^{-1} M_\odot$ ).

in numerical simulations. The influence of asymmetry and substructure on parameter recovery from weak lensing has been investigated for analytic lens models: Clowe et al. (2004) performed NFW fits to simulated lenses with varying line-of-sights and found a small dispersion. King et al. (2001) demonstrated that the presence of substructure increases this dispersion weakly and introduces only a small offset even when the amplitude is raised to extreme levels (compared to the original simulation). As the method presented here minimises assumptions about symmetry or smoothness, it has the potential to characterise irregular distributions beyond a best-fitting analytic profile. While only the first Minkowski functional has been studied in this chapter, the full set of three descriptors could be applied in the case of more complex morphologies.

A possible contamination of the weak lensing signal, which I have not considered here, is the projection of large-scale structures in the foreground onto the lens plane. Metzler et al. (1999) predicted a positive bias of a few tens of per cent for mass estimates, and Hoekstra (2003) showed that errors on best-fitting NFW parameters approximately double. The influence of such line-of-sight projections on the Minkowski functionals of the  $\zeta$ -statistics could be the subject of a future study.

Strong-lensing data can play a crucial role in constraining the inner density profile of a cluster lens (e.g. Hammer, 1991; Miralda-Escude, 1992; Fort et al., 1992; Mellier et al., 1993; Miralda-Escude, 1995; Molikawa & Hattori, 2001). It would therefore be interesting to develop an extension of the approach presented here which takes advantage of such information as the locations of multiple images and giant arcs and their shapes. Parametric models derived from strong lensing observations are error-prone, as the positions and morphologies of arcs are particularly susceptible to substructure and deviations from axisymmetry: if ellipticity and asymmetry are not taken into account, a gross overestimation of the cluster mass (Bartelmann, 1995; Hattori et al., 1998; Gavazzi, 2005; Meneghetti et al., 2007a) and misrepresentations of the central slope (Bartelmann & Meneghetti, 2004; Meneghetti et al., 2007b; Morandi et al., 2010) may result. Combining constraints from weak and strong lensing whilst maintaining translation- and rotation-invariance could be an important step towards a reliable characterisation of cluster geometry.

I have shown that an analysis of the first Minkowski functional can reliably distinguish between an

NFW halo and a singular isothermal sphere, provided that the Einstein radius has been measured. If the density of a gravitational lens follows a power law, the logarithmic slope of the Minkowski functional is constant. Deviations from this behaviour, which can be characterised by the Einstein radius of the lens and the power law exponent, are evidence of a characteristic scale and can be identified even in noisy measurements, in particular if the scale radius is much larger than the smoothing scale. Here I have compared the measured characteristic only to a single power law model, assuming that the slope is fixed at the isothermal value and the Einstein radius is known from observations; the measured change of the logarithmic slope is so pronounced that it seems likely that arbitrary power laws can be excluded, though the confidence is expected to decrease when the slope is allowed to vary. The measured Minkowski functional only needs to be tested against power laws which reproduce the data, including strong lensing, reasonably well. Given this prior, the promising results of Sec. 6.4 suggest that the discrimination between profile families is indeed possible.



# 7

Chapter 7

## 3d Cosmic Shear and the Integrated Sachs-Wolfe Effect

In this chapter I study cosmological weak lensing and its cross-correlation with the integrated Sachs-Wolfe effect. Cosmic shear is treated as a three-dimensional variable, requiring a careful numerical implementation. To that end, I focus on the efficient calculation of integrals with oscillatory kernels. Covariances of weak lensing and the iSW effect are presented for two observational scenarios. The fast implementation permits a Fisher analysis, from which I forecast errors on seven cosmological parameters.

### 7.1. Cosmic Shear

The term ‘cosmic shear’ is commonly used to refer to gravitational lensing of background galaxies by the large-scale structure. In contrast to studies of weak lensing by individual haloes of galaxies or galaxy clusters, which typically aim to constrain the mass or the density profile of the object, the focus lies on the statistical properties of the distribution of matter in the Universe.

The shear tensor, describing the distortions, is defined as the second  $\delta$ -derivative of the lensing potential (cf. Eq. 3.15),

$$\gamma(\chi, \hat{\mathbf{n}}) = \frac{1}{2} \delta\delta\phi(\chi, \hat{\mathbf{n}}), \quad (7.1)$$

where the lensing potential  $\phi(\chi, \hat{\mathbf{n}})$  is a weighted projection of the gravitational potential (cf. Eq. 3.8):

$$\phi(\chi, \hat{\mathbf{n}}) = \frac{2}{c^2} \int_0^\chi d\chi' \frac{\chi - \chi'}{\chi\chi'} \Phi(\chi, \hat{\mathbf{n}}). \quad (7.2)$$

Here spatial flatness has been assumed, and the integration is carried out in Born’s approximation, i.e. along the unperturbed light path. The weight function  $(\chi - \chi')/(\chi\chi')$  quantifies the influence of geometry: the efficiency of a gravitational lens, like that of an optical lens, is determined by the distances between source, lens and observer, implying that observed variations with redshift will be sensitive to the cosmological model. In addition, as the shear is linked to the tidal field of the gravitational potential, it probes the matter distribution in the Universe. Cosmic shear therefore provides two handles on cosmological parameters: through the matter power spectrum, and through the distance-redshift relation.

#### 7.1.1. Expansion of spin fields in three dimensions

In order to analyse the power of cosmic shear on different radial and angular scales, a suitable expansion into modes characterised by wavenumbers is necessary. Variations in the shear are observed depending on the distance  $\chi$  of the source and its position  $\hat{\mathbf{n}}$  on the sky. Thus modes are described

by a radial wavenumber  $k$  and two angular wavenumbers  $\ell$  and  $m$ ; the latter are integers and specify the degree and order of one of the spherical harmonic functions  $Y_{\ell m}(\hat{\mathbf{n}})$ , which make up the basis for the expansion on the sky. For the radial degree of freedom, the spherical Bessel functions  $j_\ell(kx)$  (Abramowitz et al., 1988) provide a suitable basis, defining the continuous wavenumber  $k$ . In the case of non-vanishing curvature, hyperspherical Bessel functions should be substituted.

A scalar quantity  $f(\chi, \hat{\mathbf{n}})$  may now be expanded as follows:

$$f(\chi, \hat{\mathbf{n}}) = \sqrt{\frac{2}{\pi}} \int k^2 dk \sum_{\ell m} f_{\ell m}(k) j_\ell(k\chi) Y_{\ell m}(\hat{\mathbf{n}}). \quad (7.3)$$

The coefficients  $f_{\ell m}(k)$  are given by the inverse of this transform:

$$f_{\ell m}(k) = \sqrt{\frac{2}{\pi}} \int \chi^2 d\chi \int d\Omega f(\chi, \hat{\mathbf{n}}) j_\ell(k\chi) Y_{\ell m}^*(\hat{\mathbf{n}}). \quad (7.4)$$

The prefactor of  $\sqrt{2/\pi}$  arises from the orthogonality relation for the spherical Bessel functions,

$$\int_0^\infty d\chi \chi^2 j_\ell(k\chi) j_\ell(k'\chi) = \frac{\pi}{2k^2} \delta^D(k - k'). \quad (7.5)$$

The transform (7.3) is suitable for scalars like the lensing potential  $\phi$ , the gravitational potential  $\Phi$  and the density contrast  $\delta$ . It may also be applied to each component of the shear  $\gamma_{+, \times}$ . It is, however, more elegant to introduce a set of basis functions that share the spin properties of the field that is to be expanded. By this means the expansion coefficients are scalars, while the behaviour of the tensor under transformations is encoded in the basis functions. The spin-weighted spherical harmonics  ${}_s Y_{\ell m}(\hat{\mathbf{n}})$  (Newman & Penrose, 1966) are the natural choice. As the derivative  $\bar{\delta}$  acts as a spin-raising operator, they are defined as

$${}_s Y_{\ell m} = \sqrt{\frac{(\ell - s)!}{(\ell + s)!}} \bar{\delta}^s Y_{\ell m}. \quad (7.6)$$

This description encompasses the scalar spherical harmonics for  $s = 0$  and generally defines fields of spin  $s$ . The derivative  $\bar{\delta}$  and its complex conjugate  $\delta$  raise and lower the spin by one, respectively:

$$\begin{aligned} \bar{\delta}({}_s Y_{\ell m}) &= +\sqrt{(\ell - s)(\ell + s + 1)} {}_{s+1} Y_{\ell m}, \\ \delta({}_s Y_{\ell m}) &= -\sqrt{(\ell + s)(\ell - s + 1)} {}_{s-1} Y_{\ell m}. \end{aligned} \quad (7.7)$$

Like the standard spherical harmonics, the spin-weighted spherical harmonics are orthonormal,

$$\int d\Omega {}_s Y_{\ell m}(\hat{\mathbf{n}}) {}_s Y_{\ell' m'}^*(\hat{\mathbf{n}}) = \delta_{\ell\ell'}^K \delta_{mm'}^K. \quad (7.8)$$

Since the shear is a spin-2 field, the appropriate transform is

$$\gamma_{\ell m}(k) = \sqrt{\frac{2}{\pi}} \int \chi^2 d\chi \int d\Omega \gamma(\chi, \hat{\mathbf{n}}) j_\ell(k\chi) {}_2 Y_{\ell m}^*(\hat{\mathbf{n}}). \quad (7.9)$$

### 7.1.2. Signal

Weak lensing data consist of the shear  $\gamma(z, \hat{\mathbf{n}})$  measured at discrete positions, each described by a redshift  $z$  and angular coordinates  $\hat{\mathbf{n}} = (\theta, \varphi)^T$ . An estimate for the amplitude  $\gamma_{\ell m}(k)$  of a mode may then be obtained by dividing three-dimensional space into cells and approximating the volume integral (7.9) by a sum. This estimate depends on the spatial distribution of sources. In addition, redshifts are generally measured photometrically and therefore prone to errors, which is taken into

account by parametrising the distribution of the photometric redshifts  $z_p$  around the true redshift  $z$ . Thus the expected signal is

$$\bar{\gamma}_{\ell m}(k) = \sqrt{\frac{2}{\pi}} \int dz \frac{n_z(z)}{4\pi} \int dz_p p(z_p|z) j_\ell [k\chi^0(z_p)] \int d\Omega \gamma(z, \hat{\mathbf{n}}) {}_2Y_{\ell m}^*(\hat{\mathbf{n}}). \quad (7.10)$$

Here  $n_z(z)$  is the source distribution:  $n_z(z) dz$  is the number of sources in the redshift interval  $[z, z + dz]$ . The source density governs how strongly data from different distances contribute to the overall signal; through this term, the survey depth influences the results. I have assumed that angular variations are negligible, so that the number of sources per steradian and redshift interval is well approximated by the mean  $n_z(z)/(4\pi)$  across the sky. Note that, by adopting a uniform source density, the influence of incomplete sky coverage is ignored. To recognise fully the effects of a finite field, a suitable window function  $W(\hat{\mathbf{n}})$  representing the actual angular distribution of data should be added. In the simplest case, this could be a top hat filter corresponding to a rectangular field of view. For a formalism which deals with such inhomogeneous sampling, see [Heavens \(2003\)](#).

The conditional probability distribution function  $p(z_p|z)$  quantifies the expected errors in the photometric redshift:  $p(z_p|z)$  is the probability that the photometric redshift  $z_p$  is assigned to a source at the true redshift  $z$ . Note that the expansion is based on the measured (photometric) redshift, which enters into the spherical Bessel function  $j_\ell[k\chi^0(z_p)]$ , whereas the observed shear signal  $\gamma(z, \hat{\mathbf{n}})$  originates from the true redshift. I follow [Heavens et al. \(2006\)](#) in denoting with  $\chi^0(z)$  the comoving distance converted from redshift  $z$  in a fiducial cosmology. This is necessary because the analysis of the data based on the transform (7.9) requires the comoving distance to the source, whereas the available distance information is restricted to redshifts. A set of cosmological parameters must then be assumed to carry out the conversion. These parameters are distinct from those describing the true underlying cosmology giving rise to the shear, and their values are not varied when the Fisher matrix is constructed.

According to Eqs. (7.1) and (7.2), the estimator (7.10) is linked to modes of the gravitational potential. Applying the expansion (7.3) to  $\Phi(\chi, \hat{\mathbf{n}})$  and taking derivatives according to (7.7) yields the expression

$$\gamma(\chi, \hat{\mathbf{n}}) = \sqrt{\frac{2}{\pi}} \frac{1}{c^2} \int_0^\chi d\chi' \frac{\chi - \chi'}{\chi\chi'} \int dk k^2 \sum_{\ell m} \sqrt{\frac{(\ell+2)!}{(\ell-2)!}} \Phi_{\ell m}(k; \chi') j_\ell(k\chi') {}_2Y_{\ell m}(\hat{\mathbf{n}}). \quad (7.11)$$

In spite of the transform from position space to wavenumbers, the comoving distance  $\chi$  appears in the parametrisation of the gravitational potential  $\Phi_{\ell m}(k; \chi)$ , reflecting its time evolution: since the density contrast and the gravitational potential change as structures grow, the expansion coefficient for a given mode depends on time. Thus the cosmic time for which the expansion of the field is performed needs to be specified, and it is here denoted by the corresponding comoving distance  $\chi$ .

The gravitational potential  $\Phi_{\ell m}(k; \chi)$  can be linked to the density contrast  $\delta_{\ell m}(k; \chi)$  using Poisson's equation,

$$\Phi_{\ell m}(k; \chi) = -\frac{3\Omega_m H_0^2}{2k^2 a(\chi)} \delta_{\ell m}(k; \chi), \quad (7.12)$$

and a relation between the amplitude of a shear mode and the matter distribution can be established:

$$\bar{\gamma}_{\ell m}(k) = -\frac{3\Omega_m}{4\pi^2 \chi_H^2} \sqrt{\frac{(\ell+2)!}{(\ell-2)!}} \int dz n_z(z) \int dz_p p(z_p|z) j_\ell [k\chi^0(z_p)] \int_0^{\chi(z)} d\chi' \frac{\chi - \chi'}{\chi\chi'} \int dk' \delta_{\ell m}(k'; \chi') j_\ell(k'\chi'). \quad (7.13)$$

From Eq. (7.13) it is evident that the harmonic coefficients  $\bar{\gamma}_{\ell m}(k)$  have vanishing expectation values; however, information is contained in their covariance  $\langle \bar{\gamma}_{\ell m}(k) \bar{\gamma}_{\ell' m'}(k') \rangle$ . The statistics of the cosmic

shear field are linked to the density field and its evolution. On small scales, where clustering becomes important, analytic descriptions fail and properties of the matter distribution are uncertain. In the linear regime, however, the Gaussian nature of the initial fluctuations is maintained and second-order statistics, such as the power spectrum  $P_\delta(k)$ , provide a complete (statistical) description. As the density field is statistically homogeneous and isotropic, its covariance matrix in harmonic space is diagonal:

$$\langle \delta_{\ell m}^0(k) \delta_{\ell' m'}^0(k') \rangle = \frac{P_\delta^0(k)}{k^2} \delta^D(k - k') \delta_{\ell \ell'}^K \delta_{mm'}^K. \quad (7.14)$$

Here  $\delta_{\ell m}^0(k)$  denotes the amplitude of a given mode evolved linearly to the present epoch. The restriction to linear structure formation also permits the calculation of correlations of the form

$$\langle \delta_{\ell m}(k; \chi) \delta_{\ell' m'}(k'; \chi') \rangle. \quad (7.15)$$

Note that the expansion coefficients  $\delta_{\ell m}(k; \chi)$  and  $\delta_{\ell' m'}(k'; \chi')$  here refer to different epochs, denoted by  $\chi$  and  $\chi'$ . The covariance thus cannot generally be expressed in terms of the matter power spectrum  $P_\delta(k; \chi)$ , which describes the statistics of the density fluctuations on a fixed spatial hypersurface. In the linear regime, however, growth is homogeneous, i.e. the scaling of the density contrast with the growth function is uniform on all scales:

$$\delta_{\ell m}(k; \chi) = D_+[a(\chi)] \delta_{\ell m}^0(k). \quad (7.16)$$

The covariance (7.15) can then be traced to the linear power spectrum today, and the full result for the covariance of cosmic shear modes is

$$\langle \bar{\gamma}_{\ell m}(k) \bar{\gamma}_{\ell' m'}(k') \rangle = \frac{9\Omega_m^2}{16\pi^4 \chi_H^4} \frac{(\ell + 2)!}{(\ell - 2)!} \int d\tilde{k} \frac{P_\delta^0(\tilde{k})}{\tilde{k}^2} G_\ell(k, \tilde{k}) G_{\ell'}(k', \tilde{k}) \delta_{\ell \ell'}^K \delta_{mm'}^K. \quad (7.17)$$

Here I have introduced the following functions:

$$G_\ell(k, k') = \int dz n_z(z) F_\ell(z, k) U_\ell(z, k'), \quad (7.18)$$

$$F_\ell(z, k) = \int dz_p p(z_p|z) j_\ell[k\chi^0(z_p)], \quad (7.19)$$

$$U_\ell(z, k) = \int_0^{\chi(z)} d\chi' \frac{\chi - \chi'}{\chi\chi'} \frac{D_+[a(\chi')]}{a(\chi')} j_\ell(k\chi'). \quad (7.20)$$

As a consequence of isotropy, the covariance does not depend on the multipole order  $m$ . In addition, there is no coupling between multipoles of different  $\ell$ , as is evident from the appearance of the Kronecker delta  $\delta_{\ell \ell'}^K$ . This is no longer strictly true if the finite field of view is taken into account: if angular integrations cannot be carried out across the full sky, or, differently put, if statistical isotropy is broken by the absence of data across parts of the sky, the orthogonality of the spherical harmonics does not prevent mixing of  $\ell$ -modes. Moreover, if the field of view is not square, results will differ between different zonal wavenumbers  $m$  even for fixed  $\ell$ . Coupling of radial modes always occurs due to the lensing weight function, the redshift errors and the redshift-dependence of the source distribution.

### 7.1.3. Noise

The weak lensing formalism is based on the assumption that the observed ellipticity  $\epsilon$  of a galaxy is the sum of the shear  $\gamma$  and its intrinsic ellipticity  $\epsilon_s$ . The intrinsic shapes of source galaxies are therefore a source of noise, given by

$$\langle \bar{\gamma}_{\ell m}(k) \bar{\gamma}_{\ell' m'}(k') \rangle_{\text{SN}} = \frac{\sigma_\epsilon^2}{2\pi^2} \int dz n_z(z) j_\ell[k\chi^0(z)] j_{\ell'}[k'\chi^0(z)] \delta_{\ell \ell'}^K \delta_{mm'}^K. \quad (7.21)$$

$\sigma_\epsilon$  is the intrinsic ellipticity dispersion, defined by  $\langle |\epsilon_s|^2 \rangle = \sigma_\epsilon^2$ ; I assume a value of  $\sigma_\epsilon = 0.3$  (cf. Heavens, 2003). This expression for the noise holds only if the intrinsic ellipticities of galaxies are uncorrelated, i.e. in absence of intrinsic alignments (see Sec. 7.7).

## 7.2. The Integrated Sachs-Wolfe Effect

The Sachs-Wolfe effect is one of the sources of anisotropy in the cosmic microwave background. It is a consequence of the gravitational redshift of photons emitted from, or crossing, potential wells. Variations in the energy density across the last scattering surface cause a primary anisotropy of the CMB, called simply the Sachs-Wolfe effect (Sachs & Wolfe, 1967). The integrated Sachs-Wolfe (iSW) effect, in contrast, arises as CMB photons propagate through time-evolving gravitational potentials. The difference between the blueshift experienced by a photon entering a gravitational well and the redshift of the exiting photon results in a net frequency change (e.g. Hu & Sugiyama, 1994). The sum of these frequency changes along the entire path of the photon causes a temperature shift, which varies with direction according to the evolution of structures along the particular line-of-sight. Since only the integrated frequency change can be observed, the effect contains no distance information and is analysed only in terms of angular modes.

### 7.2.1. Measurement

Unlike the Sunyaev-Zel'dovich effect, the iSW effect does not lead to distortions of the CMB spectrum. To disentangle the fluctuations despite their small magnitude, the cross-correlation between the CMB temperature and a suitable tracer is measured (Cooray, 2002). Such a quantity should mark the potential wells, which give rise to the frequency shifts. Detections have been based on the X-ray background (Boughn & Crittenden, 2004; Gaztañaga et al., 2006), the galaxy density in various filters (Fosalba et al., 2003; Padmanabhan et al., 2005; Vielva et al., 2006; McEwen et al., 2007; Rassat et al., 2007; Giannantonio et al., 2008) and the distributions of radio sources (Boughn & Crittenden, 2004; Pietrobon et al., 2006; Raccanelli et al., 2008) and quasars (Giannantonio et al., 2006). Recently the iSW effect was measured from CMB data alone through the cross-correlation of temperature and lensing maps (Planck Collaboration, 2015c). Observations are limited to large scales, as the power spectrum of the gravitational potential is proportional to  $k^{-4}P_\delta(k)$  and thus falls off like  $k^{-7}$  on small scales (cf. Sec. 4.1.3); moreover, potential wells associated with small objects do not evolve significantly during the time it takes for a photon to cross them. Measurements are therefore affected by cosmic variance.

### 7.2.2. Signal and noise

The relative temperature change due to the integrated Sachs-Wolfe effect is given by the integral

$$\tau(\hat{\mathbf{n}}) = \frac{2}{c^3} \int_0^{\chi_H} d\chi \frac{\partial}{\partial \eta} \Phi[\chi(\eta), \hat{\mathbf{n}}]. \quad (7.22)$$

Here the derivative is taken with respect to conformal time  $\eta$ ; it can be reparametrised using  $d\eta = dt/a = da/a^2 H(a)$ . One can transform from position space to modes  $\Phi_{\ell m}(k; \chi)$  by (7.3) and use Poisson's equation to introduce the density contrast  $\delta_{\ell m}(k; \chi)$ , leading to the following expression for the amplitude of the iSW effect:

$$\tau_{\ell m} = -\sqrt{\frac{2}{\pi}} \frac{3\Omega_m}{\chi_H^3} \int_0^{\chi_H} d\chi a^2 E(a) \int dk \frac{\partial}{\partial a} \left[ \frac{\delta_{\ell m}(k; \chi)}{a} \right] j_\ell(k\chi). \quad (7.23)$$

For  $E(a) = H(a)/H_0$  see Eq. (2.15). In this equation,  $a$  always denotes the scale factor corresponding to the comoving distance  $\chi$  acting as the integration variable. It is obvious that the iSW effect cannot arise during the matter-dominated epoch: in an Einstein-de-Sitter universe with  $\Omega_m = 1$ , the growth of overdensities is proportional to the scale factor,  $\delta \sim a$ , across all scales (cf. Sec. 4.1.2). For the derivative to be finite, a significant contribution to the energy density must be due to radiation, curvature, the cosmological constant or dark energy. Given that the Universe appears to be flat and that matter-radiation equality occurs before decoupling, the observed iSW effect must reflect the comparatively

recent rise in the dark energy contribution. It should therefore be an excellent probe for the equation of state of dark energy (e.g. [Scranton et al., 2003](#); [Nolta et al., 2004](#); [Cabr e et al., 2006](#); [Vielva et al., 2006](#); [McEwen et al., 2007](#)).

In the linear regime of structure formation the derivative appearing in the iSW signal (7.23) is simplified:

$$\frac{\partial}{\partial a} \frac{\delta_{\ell m}(k; \chi)}{a} = \delta_{\ell m}^0(k) \frac{\partial}{\partial a} \frac{D_+(a)}{a}. \quad (7.24)$$

In this approach, the results for the auto-covariance of the iSW effect and the cross-covariance with cosmic shear are as follows:

$$\langle \tau_{\ell m} \tau_{\ell' m'} \rangle = \frac{9\Omega_m^2}{2\pi\chi_H^4} \int dk \frac{P_\delta^0(k)}{k^2} W_\ell^2(k) \delta_{\ell\ell'}^K \delta_{mm'}^K, \quad (7.25)$$

$$\langle \bar{\gamma}_{\ell m}(k) \tau_{\ell' m'} \rangle = \frac{9\Omega_m^2}{8\pi^2\chi_H^4} \sqrt{\frac{2(\ell+2)!}{\pi(\ell-2)!}} \int d\tilde{k} \frac{P_\delta^0(\tilde{k})}{\tilde{k}^2} G_\ell(k, \tilde{k}) W_\ell(\tilde{k}) \delta_{\ell\ell'}^K \delta_{mm'}^K, \quad (7.26)$$

with

$$W_\ell(k) = \frac{2}{\chi_H} \int_0^{\chi_H} d\chi E(a) \left[ a \frac{\partial}{\partial a} D_+(a) - D_+(a) \right] \Big|_\chi j_\ell(k\chi). \quad (7.27)$$

As the iSW effect manifests itself in changes in the CMB temperature, the noise term is simply given by the CMB spectrum itself,  $C_\ell^{\Theta\Theta}$ . Since there are no correlations between the temperature fluctuations and the shape noise of weak lensing, no noise term needs to be added to the cross-covariance.

For the full set of iSW and cosmic shear data, the covariance matrix for a given  $\ell$ -mode then has the following structure:

$$C_\ell(k_1, k_2) = \begin{pmatrix} \langle \tau_{\ell m}^2 \rangle & \langle \tau_{\ell m} \bar{\gamma}_{\ell m}(k_2) \rangle \\ \langle \bar{\gamma}_{\ell m}(k_1) \tau_{\ell m} \rangle & \langle \bar{\gamma}_{\ell m}(k_1) \bar{\gamma}_{\ell m}(k_2) \rangle \end{pmatrix}. \quad (7.28)$$

The complete covariance matrix includes all  $\ell$  and is a block diagonal matrix with the entries  $C_\ell(k_1, k_2)$ .

## 7.3. Implementation

Two aspects of the numerical implementation of the 3d cosmic shear and iSW signals deserve attention here: the fast computation of integrals, especially those with oscillatory kernels, and the inversion of ill-conditioned matrices.

### 7.3.1. Levin integration

In the description of the iSW and weak lensing signals, several integrals of the forms

$$I_1[h] = \int_{z_1}^{z_2} dz h(z) j_\ell[k\chi(z)] \quad (7.29)$$

or

$$I_2[h] = \int_{z_1}^{z_2} dz h(z) j_\ell[k_1\chi(z)] j_\ell[k_2\chi(z)] \quad (7.30)$$

appear. Rather than redshift integrals, they can be rewritten with the comoving distance (cf. Eq. 2.19) as the integration variable:

$$I_1[h] = \frac{1}{\chi_H} \int_{\chi(z_1)}^{\chi(z_2)} d\chi E[z(\chi)] h[z(\chi)] j_\ell(k\chi); \quad (7.31)$$

$$I_2[h] = \frac{1}{\chi_H} \int_{\chi(z_1)}^{\chi(z_2)} d\chi E[z(\chi)] h[z(\chi)] j_\ell(k_1\chi) j_\ell(k_2\chi). \quad (7.32)$$

Solving these integrals numerically is somewhat challenging. The spherical Bessel functions are highly oscillatory, in particular for large  $k$  or  $\ell$ . When a large number of zero-crossings occurs in the interval  $[\chi(z_1), \chi(z_2)]$ , the result of simple quadrature rules will generally be inaccurate unless an enormous number of points is used to sample the integrand adequately. Such an approach is evidently time-consuming, and when many different combinations of  $\ell$  and  $k$  must be considered, it is not feasible.

In the following I sketch an alternative method, presented by Levin (1996, 1997). It is applicable to integrals of the form

$$I[F] = \int_a^b dx F^T(x) w(x) = \int_a^b dx \langle F, w \rangle(x), \quad (7.33)$$

where  $F(x) = [F_1(x), \dots, F_d(x)]^T$  and  $w(x) = [w_1(x), \dots, w_d(x)]^T$  are vectors of functions, for which the second equality of Eq. (7.33) defines a scalar product  $\langle, \rangle$ , and the functions  $w_i(x)$ ,  $i = 1, 2, \dots, d$ , but not  $F_i(x)$ , are rapidly oscillatory across the integration domain. In addition, a matrix of functions  $A(x)$  is defined such that the derivatives of  $w(x)$ , denoted by  $w'(x)$ , fulfil

$$w'(x) = A(x)w(x). \quad (7.34)$$

The components  $A_{iq}(x)$  should not be highly oscillatory. I show below how such a matrix can be found for the particular cases given in Eqs. (7.31) and (7.32).

The Levin formalism is designed to construct a vector  $p(x)$  which serves to approximate the integrand by

$$\langle p, w \rangle' = \langle p' + A^T p, w \rangle \approx \langle F, w \rangle. \quad (7.35)$$

The first equality is achieved by applying the Leibniz rule for derivatives and Eq. (7.34), with  $\langle p, Aw \rangle = \langle A^T p, w \rangle$ . Once such a vector has been found, the integral in Eq. (7.33) can be approximated by

$$I[F] \approx \int_a^b dx \langle p, w \rangle'(x) = \langle p, w \rangle(b) - \langle p, w \rangle(a). \quad (7.36)$$

A suitable approximation is defined by demanding that both terms should be equal,  $\langle p, w \rangle' = \langle F, w \rangle$ , at  $n$  collocation points  $x_j$ ,  $j = 1, 2, \dots, n$ . Generally the requirement

$$\langle p' + A^T p - F, w \rangle(x_j) = 0, \quad j = 1, 2, \dots, n, \quad (7.37)$$

means that the vector  $p' + A^T p - F$  must be orthogonal to  $w$  at the points  $x_j$ . One possibility to achieve this is by specifying that it should be the null vector:

$$p'(x_j) + A^T(x_j)p(x_j) = F(x_j), \quad j = 1, \dots, n. \quad (7.38)$$

In order to find a vector  $p$  which has this property one chooses a set of  $n$  linearly independent and differentiable basis functions  $u_m(x)$  and writes each component  $p_i(x)$  as a linear combination:

$$p_i(x) = c_i^{(m)} u_m(x), \quad i = 1, \dots, d; \quad m = 1, \dots, n. \quad (7.39)$$

The Einstein notation is used, i.e. summation over repeated indices ( $m$  in this case) is implied. Equation (7.38) then leads to the following linear system of equations for the  $d \times n$  coefficients  $c_i^{(m)}$ :

$$c_i^{(m)} u_m'(x_j) + A_{qi} c_q^{(m)} u_m(x_j) = F_i(x_j), \quad i, q = 1, \dots, d; \quad j, m = 1, \dots, n. \quad (7.40)$$

Levin (1996) provided examples for the application of this algorithm to several oscillatory kernels. The performance varies somewhat depending on the integrand, but accuracies below  $10^{-6}$  can often be achieved with less than 10 collocation points.

As suggested by Levin (1996), I use equidistant collocation points

$$x_j = a + (j-1) \frac{b-a}{n-1}, \quad j = 1, \dots, n, \quad (7.41)$$

and choose the  $n$  lowest-order polynomials as basis functions:

$$u_m(x) = \left( \frac{x - \frac{a+b}{2}}{b-a} \right)^{m-1}, \quad m = 1, \dots, n. \quad (7.42)$$

Note that the polynomials with  $m > 1$  and the derivatives with  $m > 2$  share the root  $x = (a+b)/2$ , which should not be used as a collocation point, as otherwise the linear system of equations will be singular. The factor  $1/(b-a)$  is included for numerical reasons: if  $b \gg 1$  or  $b \ll 1$ , the values of polynomials of different order may differ by several orders of magnitude, and ensuring that  $|u_m(x)| \leq 1$  across the integration domain helps to regulate the range of the coefficients of the linear system of equations in Eq. (7.40) and thus the condition of the corresponding matrix.

In order to identify suitable vectors  $w$  for the integrals (7.31) and (7.32), I consider the following recurrence relations for the spherical Bessel functions (Abramowitz et al., 1988):

$$\begin{aligned} j'_\ell(x) &= j_{\ell-1}(x) - \frac{\ell+1}{x} j_\ell(x), \\ j'_{\ell-1}(x) &= -j_\ell(x) + \frac{\ell-1}{x} j_{\ell-1}(x). \end{aligned} \quad (7.43)$$

Rewriting these relations in the form  $w' = Aw$ , it is immediately obvious that

$$w(\chi) = \begin{pmatrix} j_\ell(k\chi) \\ j_{\ell-1}(k\chi) \end{pmatrix}, \quad A(\chi) = \begin{pmatrix} -\frac{\ell+1}{x} & k \\ -k & \frac{\ell-1}{x} \end{pmatrix} \quad (7.44)$$

is a suitable choice for the integral (7.31), with  $F(\chi) = \{E[z(\chi)]h[z(\chi)], 0\}^T$ . It is easy to verify that neither the entries of the matrix  $A$  nor the integral kernels  $F$  appearing in my calculations are rapidly oscillatory.

For integrals of the type (7.32), four-dimensional vectors are needed:

$$w(\chi) = \begin{pmatrix} j_\ell(k_1\chi)j_\ell(k_2\chi) \\ j_{\ell-1}(k_1\chi)j_\ell(k_2\chi) \\ j_\ell(k_1\chi)j_{\ell-1}(k_2\chi) \\ j_{\ell-1}(k_1\chi)j_{\ell-1}(k_2\chi) \end{pmatrix}, \quad A(\chi) = \begin{pmatrix} -\frac{2(\ell+1)}{x} & k_1 & k_2 & 0 \\ -k_1 & -\frac{2}{x} & 0 & k_2 \\ -k_2 & 0 & -\frac{2}{x} & k_1 \\ 0 & -k_2 & -k_1 & \frac{2(\ell-1)}{x} \end{pmatrix}. \quad (7.45)$$

Similarly,  $F(\chi) = \{E[z(\chi)]h[z(\chi)], 0, 0, 0\}^T$ .

I implement this algorithm in an iterative scheme based on bisection, which is beneficial in cases in which the non-oscillatory component of the integrand has a narrow peak (compared to the width of the interval of the integration). The error of the integration in each subinterval is estimated as the difference between the approximation with  $n$  collocation points and the result for  $n/2$  points. In each step the interval with the largest estimated error is bisected. The iteration terminates when one of the following criteria is met: the number of subintervals exceeds a fixed maximum; the length of all

subintervals is less than a fixed minimum; the integration is classed as successful. For the last criterion, the current approximation is compared to that of the previous iteration step, and if the difference is less than the tolerance, the result is accepted. The second criterion reflects machine precision and is necessary to avoid scenarios in which the limits of a subinterval are ‘too close’ numerically. I use eight collocation points and a maximum of 16 subintervals. As the integral  $G_\ell(k_1, k_2)$  in Eq. (7.18) does not contain an oscillatory kernel, it is solved using a composite Simpson rule.

Redshift integrations run from  $z_{\min} = 10^{-4}$  to  $z_{\max} = 4$ . This upper limit is sufficient for the surveys described below given the drop in the source distribution at much lower redshifts, even when it is convolved with the probability distribution of the photometric redshift errors.

The limits of the distance integrals generally correspond to these values. For integrations using the Levin method, however, I further constrict the domain as follows: for  $\ell \gg 1$ , the behaviour of the spherical Bessel functions  $j_\ell(x)$  is marked by a sharp rise around  $x \sim \ell$ , with  $j_\ell(x) \ll 1$  for  $x \ll \ell$  and the characteristic oscillatory behaviour for  $x > \ell$ . I integrate only from  $\chi_\epsilon$  with  $|j_\ell(k\chi)| < \epsilon$  for  $\chi < \chi_\epsilon$  and a small threshold  $\epsilon$ . If  $\chi_\epsilon$  is larger than the upper limit of the integral, no integration is carried out and the integral is set to zero. The value  $\chi_\epsilon$  depends on both  $\ell$  and  $k$ . I use CLASS to calculate the spherical Bessel functions as well as the linear matter power spectrum. The value of the argument at which the function  $j_\ell(x)$  first crosses a given threshold is easily accessible, permitting a very fast calculation of the integral limit  $\chi_\epsilon$ .

### 7.3.2. Numerical integration through matrix multiplication

Despite the remarkable reduction in computing time achieved by Levin integration, the calculation of the covariance remains numerically expensive, and it is advisable to keep the number of operations as low as possible. To that end, some care is required to avoid the repeated calculation of integrals which appear multiple times in the calculation (see Eqs. 7.17–7.20, 7.25–7.27). The conversion between the redshift  $z$  and the comoving distance  $\chi(z)$  (Eq. 2.19) and the solution of the differential equation (4.8) for the growth function  $D_+(a)$  can be tabulated and interpolated. Many of the more complex integrations, however, depend on the wavenumbers  $\ell$  and  $k$ . All entries of the covariance matrix have the form

$$C_\ell(k_1, k_2) = \int d\tilde{k} \frac{P_\delta^0(\tilde{k})}{\tilde{k}^2} I_\ell(\tilde{k}, k_1, k_2), \quad (7.46)$$

where the kernel  $I_\ell(k, k_1, k_2)$  depends on which of the auto- or cross-correlations is considered. Let  $n_k$  be the number of modes  $k_i$  in the calculation, so that the full covariance matrix of weak lensing and the iSW effect  $C_\ell$  is a  $(n_k + 1) \times (n_k + 1)$ -matrix (cf. Eq. 7.28). The  $k$ -integral in Eq. (7.46) can be approximated by the sum

$$C_\ell(k_i, k_j) \approx \sum_{a=1}^{n_i} \Delta\tilde{k}_a \frac{P_\delta^0(\tilde{k}_a)}{\tilde{k}_a^2} I_\ell(\tilde{k}_a, k_i, k_j). \quad (7.47)$$

Here  $n_i$  grid points with the values  $\tilde{k}_a$  and the spacings  $\Delta\tilde{k}_a$  are used for the integration. Equations (7.17)–(7.20) and (7.25)–(7.27) show that the covariance matrix can be written as the matrix product

$$C_\ell = B_\ell B_\ell^\top, \quad (7.48)$$

where  $B_\ell$  has the dimensions  $(n_k + 1) \times (n_i + 1)$  and the form

$$B_\ell = \begin{pmatrix} 0 & \mathbf{v}_\ell^\top \\ 0 & M_\ell \end{pmatrix}. \quad (7.49)$$

The vector  $\mathbf{v}_\ell$  must fulfil  $\mathbf{v}_\ell^\top \mathbf{v}_\ell = \langle \tau_{\ell m}^2 \rangle$ , thus

$$\mathbf{v}_\ell(\tilde{k}_a) = \frac{3\Omega_m}{\sqrt{2\pi}\chi_H^2} \frac{W_\ell(\tilde{k}_a)}{\tilde{k}_a} \sqrt{P_\delta^0(\tilde{k}_a)\Delta\tilde{k}_a}. \quad (7.50)$$

Similarly one finds

$$M_\ell(k_i, \tilde{k}_a) = \frac{3\Omega_m}{4\pi^2\chi_H^2} \sqrt{\frac{(\ell+2)!}{(\ell-2)!}} \frac{G_\ell(k_i, \tilde{k}_a)}{\tilde{k}_a} \sqrt{P_\delta^0(\tilde{k}_a)\Delta\tilde{k}_a}. \quad (7.51)$$

This approach permits an efficient calculation of the  $k$ -integrals. The spacing  $\Delta\tilde{k}_a$  need not be equal to the spacing of the lensing modes between which the covariances are calculated, nor the range. For the low multipoles, at which the iSW signal is included, the accuracy for a given number of points is typically better if grid points are logarithmically equidistant.

### 7.3.3. Singular modes

Due to the steep increase of the spherical Bessel functions  $j_\ell(k\chi)$  close to  $k\chi \sim \ell$ , the lensing signal is very weak for the smallest radial wavenumbers  $k$ , and the entries of the covariance matrix cover many orders of magnitude. As the matrix may be very close to singular, the inversion can be difficult numerically. For this reason, I discard the weakest modes based on a singular value decomposition. To that end, the covariance matrix  $C$  is factorised as

$$C = UWV^T, \quad (7.52)$$

where  $U$  and  $V$  are symmetric matrices and  $W$  is a diagonal matrix containing the singular values  $w_i$ . If  $C$ , and therefore  $W$ , is invertible, the inverse  $W^{-1}$  is a diagonal matrix with the entries  $1/w_i$  and  $C^{-1} = VW^{-1}U^T$ . If, however,  $C$  contains singular modes, the pseudoinverse (or Moore-Penrose inverse)  $W^+$  can be calculated, setting the diagonal entries to 0 rather than  $1/w_i$  if  $w_i = 0$ . To remove also modes with negligibly small signals, I apply this treatment to all singular values with  $w_i < \epsilon$ , where  $\epsilon$  is a threshold representing machine precision. The resulting matrix  $\tilde{W}^+$  is used to find the pseudoinverse

$$\tilde{C}^+ = V\tilde{W}^+U^T. \quad (7.53)$$

Additional care must be taken when the covariance includes iSW data. The iSW signal is typically about 18 orders of magnitude smaller than the maximum of the weak lensing power, and if the approach described above were carried out for the full covariance matrix, the iSW mode would generally be discarded. Therefore I use a block-wise inversion. For the combined data sets, the covariance matrix has the shape

$$C_\ell = \left( \begin{array}{c|c} t & x^T \\ \hline x & S \end{array} \right), \quad (7.54)$$

where the scalar  $t$  stands for the iSW auto-covariance,  $x$  is a vector representing the cross-covariance, and  $S$  is the cosmic shear covariance matrix. In such a case the inverse is given by (Koecher, 1992)

$$C_\ell^{-1} = \left( \begin{array}{c|c} \frac{1}{\alpha} & -\frac{x^T S^{-1}}{\alpha} \\ \hline -\frac{S^{-1}x}{\alpha} & S^{-1} + \frac{S^{-1}xx^T S^{-1}}{\alpha} \end{array} \right), \quad (7.55)$$

where  $\alpha = t - x^T S^{-1}x \neq 0$ .  $S^{-1}$  will be replaced by  $\tilde{S}^+$ , calculated from a singular value decomposition as described above. This treatment ensures that the inversion is numerically stable despite the vastly different orders of magnitude of the signals.

**Table 7.1.:** Specifications for stage III and stage IV weak lensing surveys: the median redshift  $z_m$ ; the source density  $n_0$ ; the error in photometric redshifts,  $\sigma(z) = \sigma_z(1+z)$ ; the field size  $\Omega_{\text{sky}}$ .

Stage	$z_m$	$n_0$ [arcmin $^{-2}$ ]	$\sigma_z$	$\Omega_{\text{sky}}$ [deg $^2$ ]
III	0.7	12	0.05	5,000
IV	0.9	40	0.03	20,000

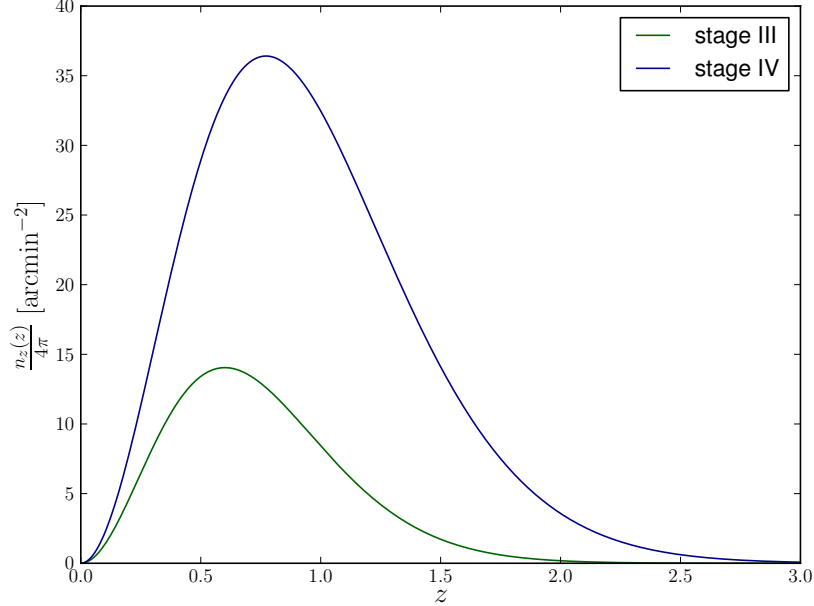


**Figure 7.1.:** Source-redshift distributions  $n_z(z)$  for two weak lensing surveys.

## 7.4. Survey Characteristics

I consider two weak lensing surveys. In the framework of the Dark Energy Task Force (DETF) (Albrecht et al., 2006) these represent research stages III and IV. Parameters entering the description of the signal are listed in Table 7.1. The specifications for the stage III experiment are based on the design of the ground-based Dark Energy Survey (DES) (The Dark Energy Survey Collaboration, 2005), while the parameter choice for the stage IV survey follows the goals for the upcoming space-based Euclid mission (Laureijs et al., 2011). In the following I refer to these survey designs either by their stage or as ‘DES-like/Euclid-like’.

For the source distribution I follow Baugh & Efstathiou (1993) and choose the shape

$$n_z(z) = 6\pi n_0 \left(\frac{1.412}{z_m}\right)^3 z^2 \exp\left[-\left(\frac{1.412z}{z_m}\right)^{3/2}\right]. \quad (7.56)$$

$z_m$  is the median redshift of the survey. The distribution is normalised to match the observed redshift-integrated source density  $n_0$ . It is not cut off at a minimum and/or maximum redshift; as the number of sources close to the redshift limits is very small, the influence on the results is negligible.

Redshift errors are assumed to be Gaussian,

$$p(z_p|z) = \frac{1}{\sqrt{2\pi}\sigma(z)} \exp\left[-\frac{(z_p - z)^2}{2\sigma^2(z)}\right], \quad (7.57)$$

with a redshift-dependent dispersion (Ilbert et al., 2006)

$$\sigma(z) = \sigma_z(1+z). \quad (7.58)$$

This description does not include a bias, though it can easily be added by modifying the Gaussian accordingly. Catastrophic outliers are not considered. For a discussion of the photometric accuracy in weak lensing tomography, see [Abdalla et al. \(2008\)](#).

Some care must be taken in choosing the maximum wavenumbers. The description presented here is only valid for modes which evolve in the linear regime; moreover, [Merkel & Schäfer \(2013\)](#) showed that the relative contribution of intrinsic alignments to the covariance increases with the multipole order. Realising that the linear approximation clearly breaks down when the density contrast reaches  $\delta \sim 1$ , one can estimate the scale on which the variance of the smoothed density field is unity (e.g. [Peacock & Dodds, 1996](#); [Smith et al., 2003](#)) and find the corresponding wavenumber  $k_{\text{nl}}$ , which is about  $0.3 h \text{ Mpc}^{-1}$  today and grows with redshift (cf. also [Fig. 4.1](#)). Limber's approximation ([Limber, 1953, 1954](#)) establishes a link to multipole orders  $\ell$ : if an observable is projected onto the sphere with a narrow weight function centred on the radius  $R$ , the multipole  $\ell$  of the angular spectrum reflects the three dimensional power at  $k \simeq \ell/R$ . Given a survey depth of the order of  $1\text{--}2 h^{-1} \text{ Gpc}$  I restrict the analysis to  $\ell_{\text{max}} = 1000$ , avoiding the uncertainties of non-linear growth and limiting the numerical expense, and include 500 radial modes up to  $k_{\text{max}} = 1 h^{-1} \text{ Mpc}$ ; while the evolution may be mildly non-linear for the smallest radial modes, the main contribution to the highest multipole  $\ell_{\text{max}}$  comes from somewhat lower  $k$ -values (cf. [Heavens, 2003](#); [Castro et al., 2005](#)). The iSW signal is added for multipoles up to  $\ell = 40$ ; from the results in [Planck Collaboration \(2014a\)](#) and [Planck Collaboration \(2015c\)](#) it is evident that contributions from smaller scales are negligible.

## 7.5. Spectra and Correlations

The weak lensing covariance is illustrated in [Fig. 7.2](#), which shows the signal for the Euclid-like survey for the multipoles  $\ell = 10, 30, 100, 300$ . The height of the maximum decreases with increasing multipole order, while the width increases, reflecting the mode coupling on smaller scales. As expected, the location of the peak moves to larger  $k$  – this is the behaviour that leads to the Limber approximation.

The angular power spectrum of the iSW effect is shown in the left panel of [Fig. 7.3](#). As expected, the signal is largest at the lowest multipoles. Since the temperature spectrum of the CMB is nearly flat on these large scales (cf. [Fig. 4.2](#)), the signal-to-noise ratio also decreases.

To illustrate the cross-correlations, I also calculate Pearson's correlation coefficient

$$r_{\ell}(k) = \frac{\langle \tau_{\ell m} \bar{\gamma}_{\ell m}(k) \rangle}{\sqrt{\langle \tau_{\ell m}^2 \rangle \langle \bar{\gamma}_{\ell m}^2(k) \rangle}}. \quad (7.59)$$

It follows from the Cauchy-Schwarz inequality that  $-1 \leq r_{\ell}(k) \leq 1$ . A value of  $r = 1$  indicates a perfect linear correlation between the two variables; a common interpretation is that in this case all data points in a sample lie on a straight line. This is also true if  $r = -1$ , but the slope of the line is negative. A vanishing correlation coefficient implies that there is no linear correlation. If the correlation coefficient is positive, deviations of both variables from the mean tend to have the same sign, whereas opposite signs lead to a negative correlation coefficient.

Values of the correlation coefficient  $r_{\ell}(k)$  for cosmic shear and the iSW effect are plotted in the right panel of [Fig. 7.3](#). Note that the negative sign mainly reflects the definition of the temperature fluctuation associated with the iSW effect and is of no great interest here: as the expectation values of both observables vanish, negative deviations do not correspond to weak signals. Finite correlations clearly exist between the two signals. In the limit  $kR \ll \ell$  (where  $R$  again stands for the survey depth)  $r_{\ell}(k)$  is close to  $-1$ , implying that corresponding lensing modes contain little independent information compared to the multipole  $\ell$  of the iSW effect. For  $kR \gg \ell$ , in contrast, correlations nearly vanish: cosmic shear modes with large radial wavenumbers probe small scales and are therefore only weakly correlated with the iSW signal, which is restricted to the low multipoles. Given this cross-correlation profile, independent information can be gained from the combination of the two data sets, in particular from the low multipoles.

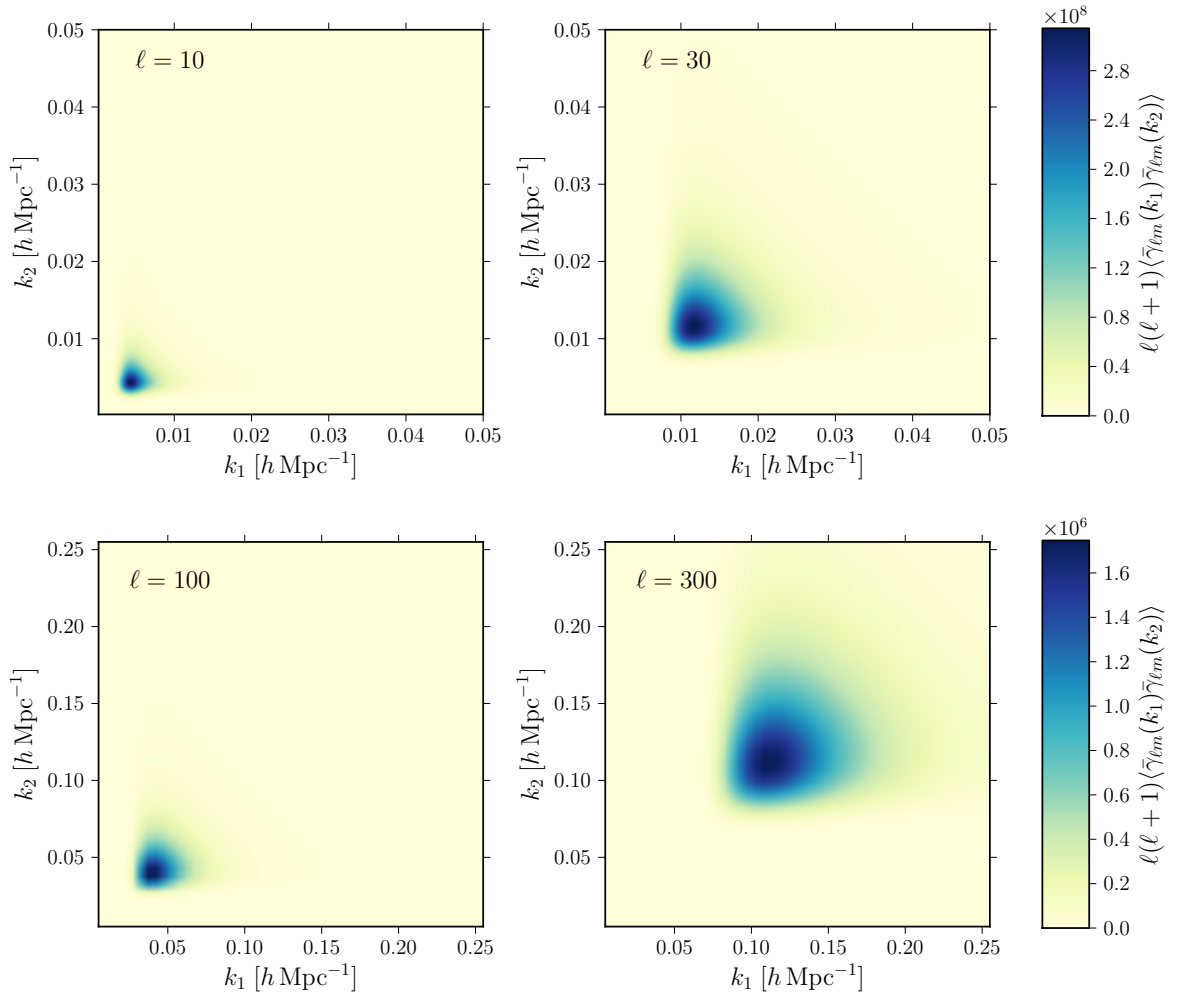


**Figure 7.2.:** Weak lensing covariance  $\langle \bar{\gamma}_{\ell m}(k_1) \bar{\gamma}_{\ell m}(k_2) \rangle$  for a stage IV survey, for four different multipole orders. Note the different ranges.

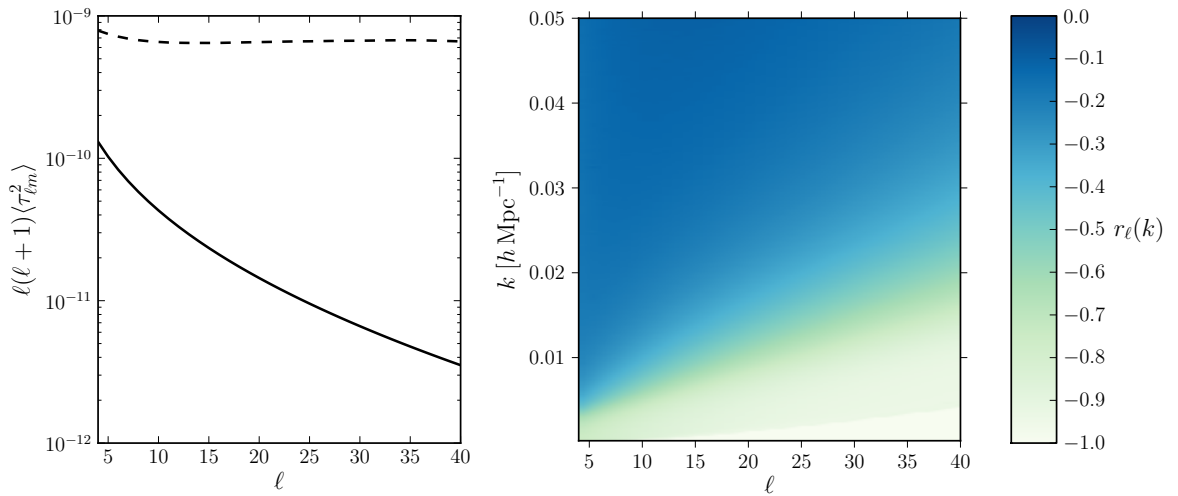


**Figure 7.3.:** Spectrum of the iSW effect (left), and the cross-correlation with cosmic shear (right). The solid line indicates the signal, the dashed line the noise.  $r_\ell(k)$  is the Pearson correlation coefficient.

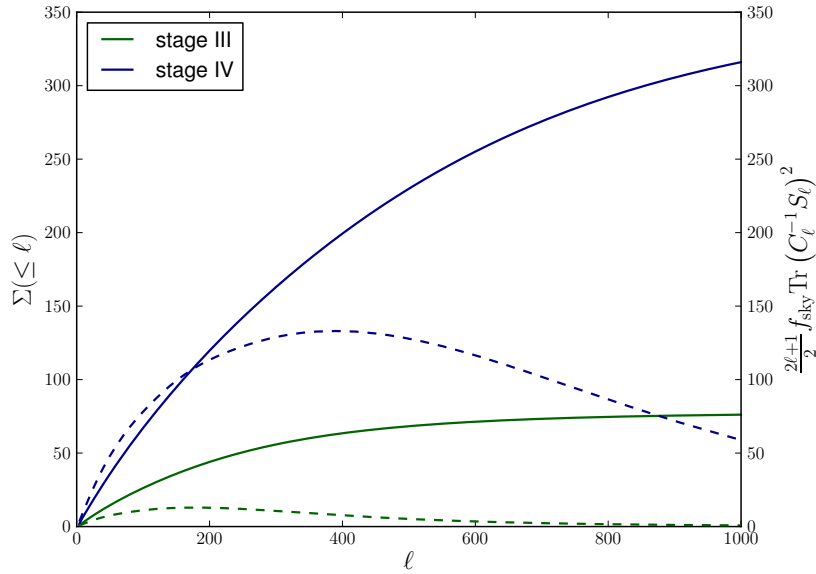


**Figure 7.4.:** Signal-to-noise ratio as a function of the maximum multipole order  $\ell$  for two weak lensing surveys. Solid lines show the cumulative signal-to-noise ratio  $\Sigma(\leq \ell)$ . The dashed lines illustrate the contributions of individual modes.

The signal-to-noise ratio can be estimated as

$$\Sigma^2 = f_{\text{sky}} \sum_{\ell} \frac{2\ell + 1}{2} \text{Tr}(C_{\ell}^{-1} S_{\ell})^2. \quad (7.60)$$

The choice of this estimator is motivated by the Fisher matrix approach; see Sec. 7.6.1 below.  $S_{\ell}$  denotes the noise-free covariance matrix. The sky coverage  $f_{\text{sky}} = \Omega_{\text{sky}}/(4\pi)$  reflects the reduced information content of a limited field compared to a full-sky survey. I plot the result for both surveys in Fig. 7.4, using the shorthand notation  $\Sigma(\leq \ell)$  for the cumulative signal-to-noise ratio up to the maximum multipole order  $\ell$ , which corresponds to truncating the sum in Eq. (7.60) at this value. I also plot the summands to illustrate the contributions of individual  $\ell$ -modes. The overall signal-to-noise ratios up to the maximum multipole order  $\ell_{\text{max}} = 1000$  differ roughly by a factor of 4. This is close to the scaling of Poisson noise with the square root of the number of sources, which is proportional to the field size  $\Omega_{\text{sky}}$  (or sky coverage  $f_{\text{sky}}$ ) and the projected source density  $n_0$ . The exact result reflects additional differences, such as the shape of the source distribution for different depths and the distribution of photometric redshifts. For the realisation of a stage III survey considered here, the cumulative signal-to-noise ratio flattens off considerably already at  $\ell \approx 600$ , whereas it is still rising at  $\ell = 1000$  for the Euclid-like survey. This suggests that an appropriate treatment of higher modes, taking difficulties such as non-linearities and intrinsic alignments into account, could lead to a significant gain in information.

## 7.6. Cosmological Constraints

For the error forecast I consider seven cosmological parameters: the matter density parameter  $\Omega_m$ ; the amplitude of density fluctuations  $\sigma_8$ ; the dark energy equation of state parametrised by  $w_0$  and  $w_a$ , with  $w(a) = w_0 + w_a(1 - a)$ ; the baryon density parameter  $\Omega_b$ ; the spectral index  $n_s$  of the matter power spectrum; and the Hubble parameter  $h$ . A  $\Lambda$ CDM-model is chosen as the fiducial cosmology, hence  $w_0 = -1$  and  $w_a = 0$ . The values of the remaining parameters are listed in Table 7.2; they are the intermediate results of the Planck mission, published in Planck Collaboration (2014b).

**Table 7.2.:** Values of the cosmological parameters in the fiducial model assumed for the error forecast.

$\Omega_m$	$\sigma_8$	$w_0$	$w_a$	$\Omega_b$	$n_s$	$h$
0.314	0.834	-1.00	0.00	0.0486	0.962	0.674

### 7.6.1. The Fisher matrix approach

The Fisher matrix formalism provides error forecasts for parameter estimation problems. Assuming a Gaussian distribution for the data and a Gaussian posterior for the parameters, the Fisher matrix contains lower limits on the variances and covariances of the parameters for a given experimental design. [Vogeley & Szalay \(1996\)](#) and [Tegmark et al. \(1997\)](#) were among the first to present applications in cosmology; since then, Fisher analyses have been carried out for many different observations and cosmological models. I outline the approach in the following.

Let  $\mathbf{d}$  be a set of data and  $\theta$  the parameters characterising a model, the values of which are to be determined from the data. An uninformative prior is assumed for the parameters,  $p(\theta) = \text{const.}$  Then Bayes's theorem links the likelihood  $L$  of the data  $\mathbf{d}$  conditional upon the model to the posterior distribution of  $\theta$  given  $\mathbf{d}$ :  $p(\theta|\mathbf{d}) \sim p(\mathbf{d}|\theta) = L$ . Values of  $\theta$  can be obtained by maximizing the likelihood  $L$  in parameter space. To estimate the errors, a Taylor expansion of the log-likelihood about the maximum up to second order is carried out. As the first derivatives vanish at the peak, the two remaining terms are a constant and the Hessian, i.e. the matrix of second derivatives. The Fisher matrix is the ensemble average of the Hessian:

$$F_{\alpha\beta} = - \left\langle \frac{\partial^2 \ln L}{\partial \theta_\alpha \partial \theta_\beta} \right\rangle. \quad (7.61)$$

It acts as the inverse covariance matrix of the parameters, and error bounds for individual parameters can easily be derived from its entries: the error in a model parameter  $\theta_\alpha$  is  $\Delta\theta_\alpha \geq (F_{\alpha\alpha})^{-1/2}$  if all other parameters are known. For the marginal error, i.e. marginalising over all parameters but  $\theta_\alpha$ , the inverse of the Fisher matrix must be considered; in this case,  $\Delta\theta_\alpha \geq (F^{-1})_{\alpha\alpha}^{1/2}$ . The Cramér-Rao inequality ([Rao, 1945](#); [Cramér, 1974](#)) states that these are the minimum errors that can be obtained from the experiment given the information content of the data.

If the likelihood surface is Gaussian in parameter space, or well approximated by a Gaussian, the log-likelihood has the form

$$2 \ln L = \text{const.} - \det C - (\mathbf{d} - \boldsymbol{\mu})^T C^{-1} (\mathbf{d} - \boldsymbol{\mu}), \quad (7.62)$$

and the Fisher matrix can be calculated from the covariance matrix and its derivatives ([Tegmark et al., 1997](#)):

$$F_{\alpha\beta} = \frac{1}{2} \text{Tr} \left[ C^{-1} C_{,\alpha} C^{-1} C_{,\beta} + C^{-1} (\boldsymbol{\mu}_{,\alpha} \boldsymbol{\mu}_{,\beta}^T + \boldsymbol{\mu}_{,\beta} \boldsymbol{\mu}_{,\alpha}^T) \right], \quad (7.63)$$

where  $\boldsymbol{\mu}$  is the vector of expectation values and  $C = \langle (\mathbf{d} - \boldsymbol{\mu})(\mathbf{d} - \boldsymbol{\mu})^T \rangle$  is the covariance matrix of the data. The subscript  $_{,\alpha}$  denotes the derivative with respect to parameter  $\theta_\alpha$ . Note that Fisher matrices for two independent experiments can simply be added to obtain the information in both data sets.

The Fisher information matrix misrepresents errors and degeneracies if the likelihood close to the maximum deviates strongly from a Gaussian. [Wolz et al. \(2012\)](#) compared error forecasts from a Fisher analysis to the results of Monte Carlo sampling of the likelihood for several cosmological probes including cosmic shear tomography, considering stage III and stage IV weak lensing surveys with similar specifications to the scenarios presented here. Good agreement was found between the full likelihood contours and the ellipses in the Gaussian approximation. More generally the Fisher approach was shown to be suitable for observables which trace structure formation in addition to the distance-redshift relation. Since three-dimensional weak lensing and the integrated Sachs-Wolfe effect satisfy this condition, these findings justify a Fisher analysis.

**Table 7.3.:** Marginal 1- $\sigma$  errors on cosmological parameters from three-dimensional weak lensing (3dWL) combined with an iSW experiment. Also shown is the dark energy figure-of-merit. Correlations between data sets are included for 3dWL*×*iSW.

Parameter	Stage III			Stage IV		
	3dWL	3dWL+iSW	3dWL <i>×</i> iSW	3dWL	3dWL+iSW	3dWL <i>×</i> iSW
$\Omega_m$	0.172	0.149	0.104	0.0299	0.0297	0.0273
$\sigma_8$	0.321	0.270	0.166	0.0464	0.0460	0.0411
$w_0$	1.12	1.04	0.88	0.234	0.233	0.220
$w_a$	6.07	5.27	3.70	1.028	1.021	0.927
$\Omega_b$	0.083	0.083	0.083	0.0185	0.0185	0.0185
$n_s$	0.217	0.215	0.211	0.0458	0.0458	0.0444
$h$	0.781	0.741	0.669	0.154	0.154	0.150
FOM	0.446	0.540	0.946	15.3	15.4	17.9

Averaged over a large number of realisations, the expectation values of both the iSW and the cosmic shear signal vanish,  $\mu = 0$ , independent of the cosmological model, so that only the covariance must be considered. As established in Sec. 7.2.2, the covariance matrix is a block diagonal matrix in absence of angular mixing. Equation (7.63) then simplifies considerably. In the analysis below I use the formula

$$F_{\alpha\beta} = f_{\text{sky}} \sum_{\ell} \frac{(2\ell + 1)\Delta\ell}{2} \text{Tr} [C_{\ell}^{-1} C_{\ell,\alpha} C_{\ell}^{-1} C_{\ell,\beta}]. \quad (7.64)$$

Errors are proportional to  $f_{\text{sky}}^{-1/2}$ . The multiplicity  $2\ell + 1$  for each multipole arises from the range of the zonal wavenumber  $m$  – since the covariance matrix does not depend on  $m$ , each submatrix  $C_{\ell}$  appears  $2\ell + 1$  times. If not all multipoles are calculated, Eq. (7.64) serves as an approximation:  $\Delta\ell$  is the spacing between  $\ell$ -modes. I carry out the calculation for all multipoles up to  $\ell = 40$ , the limit for the iSW effect, and for equidistant values with  $\Delta\ell = 10$  up to  $\ell_{\text{max}} = 1000$ .

## 7.6.2. Error forecasts

I forecast cosmological parameter errors for the following combinations of data sets: ‘3dWL’ denotes a cosmic shear survey; the abbreviation ‘3dWL+iSW’ stands for independent weak lensing and iSW experiments, for which cross-correlations are ignored and the Fisher matrices are simply added; ‘3dWL*×*iSW’ indicates that the covariance between the two data sets is included. I also generate a CMB prior according to the prescription given by Perotto et al. (2006), considering the auto- and cross-correlations of the temperature and  $E$ -modes of the polarisation in a Planck-like experiment, and add it to all of the above combinations.

The marginal 1- $\sigma$  errors are presented in Tables 7.3 and 7.4. Also included is the figure-of-merit for dark energy (abbreviated ‘FOM’), which measures the statistical power of the survey design to test the null hypothesis of a cosmological constant. I adopt the definition by Albrecht et al. (2009):

$$\text{FOM} = \frac{1}{\det(F^{-1})_w}. \quad (7.65)$$

Here  $(F^{-1})_w$  denotes the  $2 \times 2$ -submatrix of the inverse of the Fisher matrix. The figure-of-merit given by Eq. (7.65) is inversely proportional to the area of the confidence ellipse in the  $w_0$ - $w_a$  plane, so that constraints on the equation of state improve with increasing FOM.

Table 7.3 shows that constraints are generally poor for the stage III experiment, implying that it is not possible to constrain such a number of parameters simultaneously for the given survey design.

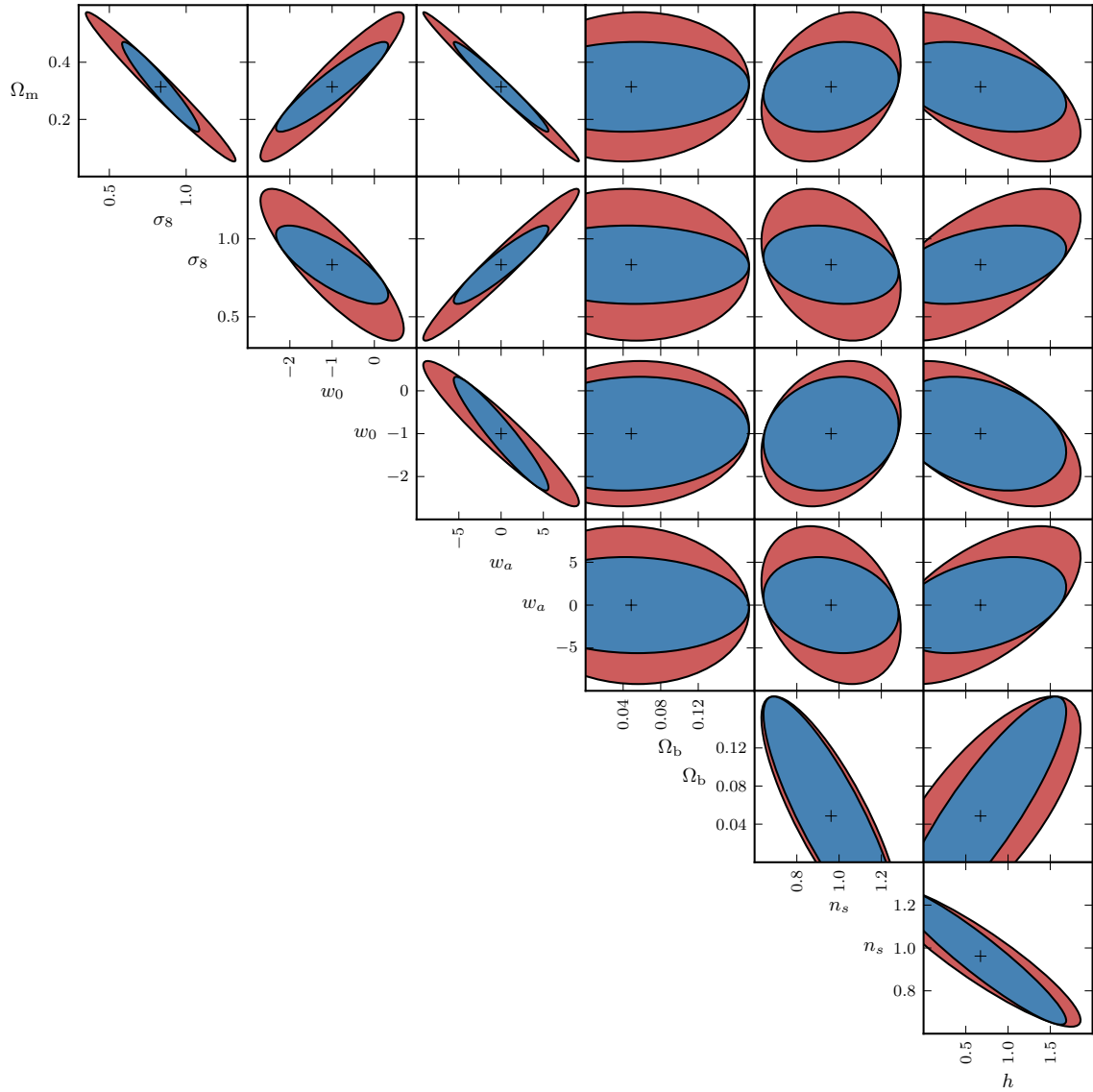


**Figure 7.5.:**  $1\text{-}\sigma$  confidence regions for cosmological parameters derived from a stage III weak lensing survey. The red ellipses illustrate constraints from lensing information alone. For the blue ellipses iSW data have been added.

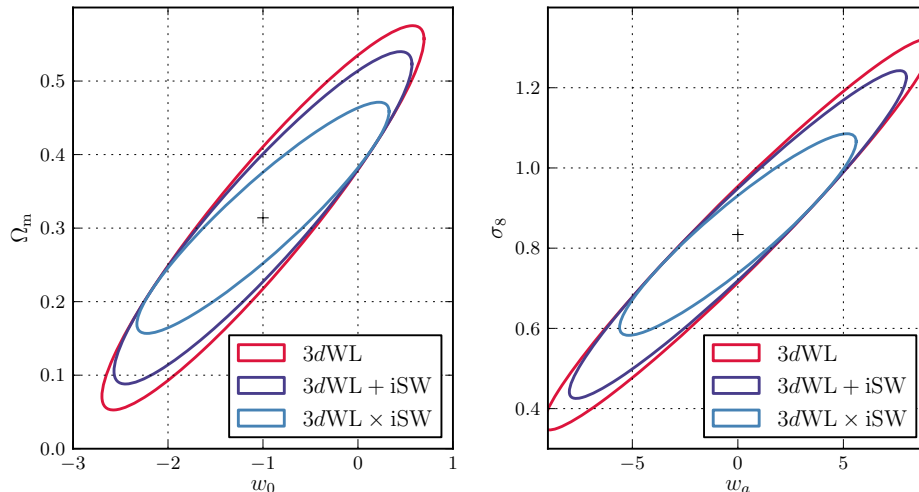


**Figure 7.6.:**  $1\text{-}\sigma$  confidence regions from the combination of cosmic shear with a stage III survey and the iSW effect, with ( $\times$ ) and without ( $+$ ) information from cross-correlations.

However, it is worth noting that improvements between 20 and 50 per cent in the marginal errors on  $\Omega_m$ ,  $\sigma_8$ ,  $w_0$  and  $w_a$  are achieved when iSW data are added, and the figure-of-merit more than doubles. The influence on  $\Omega_b$ ,  $n_s$  and  $h$  is much weaker, which is hardly unexpected, as these parameters only affect the shape of the matter power spectrum and degeneracies cannot be broken by additional iSW information. Error ellipses for all parameter pairs, obtained from cosmic shear alone and the full information, respectively, are shown in Fig. 7.5.

If correlations between lensing and iSW data are ignored, errors reduce by five to ten per cent compared to cosmic shear alone; the figure-of-merit increases by 20 per cent. This demonstrates that valuable information is encoded in the cross-correlation of the signals, in agreement with my interpretation of the Pearson correlation coefficient above (see Sec. 7.5). In Fig. 7.6 the effect of the additional information on the Fisher ellipses is illustrated, demonstrating the decrease in size and the altered degeneracy.

In Fig. 7.7 the contribution of individual angular modes to the full Fisher information is illustrated: I plot the value of the summand in the formula (7.64) for the Fisher matrix, in this example the  $w_0 w_0$ -element, as a function of the multipole order  $\ell$ , which is identical to the Fisher matrix if only a single angular mode is considered. The iSW signal clearly adds power on the largest scales. With growing multipole order the Fisher information in the combined experiment approaches the cosmic shear information; as expected, at  $\ell = 40$ , the maximum multipole order in the iSW calculation, the gain is almost negligible.

Errors obtained for a Euclid-like survey are smaller by about a factor of four (cf. the remarks on the signal-to-noise ratio, Sec. 7.5); the figure-of-merit increases by a factor of 34. Figure 7.8 shows the confidence regions obtained from the full information. The reduction achieved with iSW information is smaller than for the DES-like survey – in absence of correlations constraints on  $\Omega_m$ ,  $\sigma_8$ ,  $w_0$  and  $w_a$  improve by less than one per cent, whereas errors decrease by about ten per cent if the full covariance is considered; the gain in the figure-of-merit is 17 per cent. Figure 7.7 suggests that the additional power in the low  $\ell$  modes is overwhelmed somewhat by the cosmological sensitivity of the high lensing multipoles, which dominate the Fisher information. Note that the sensitivity peaks at smaller scales compared to the stage III survey. It is still high at  $\ell_{\max} = 1000$ , suggesting that a Euclid-like survey can probe even smaller scales; however, an appropriate treatment of non-linear structure formation is indispensable in this case.

Table 7.4 lists errors obtained in combination with a CMB prior. Even a stage III weak lensing survey is capable of narrowing constraints by 10–30 per cent compared to the CMB alone; for the

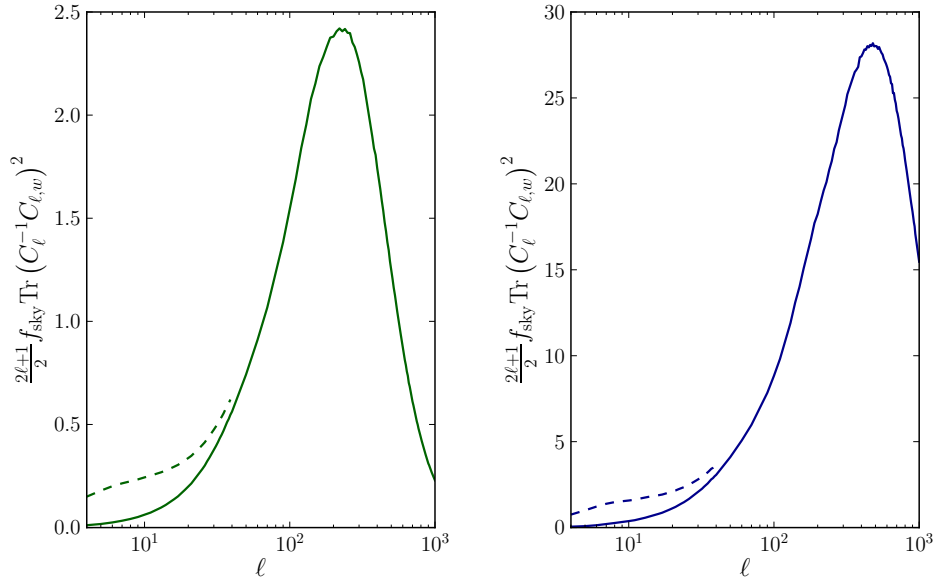


**Figure 7.7.:** Contributions of different angular scales to the  $w_0w_0$ -element of the Fisher matrix for stage III (left) and stage IV (right) weak lensing experiments. The curves show the matrix element as a function of the multipole order  $\ell$ ; the Fisher matrix for the complete information is the sum of these terms over all modes. Solid lines are calculated from lensing data only, dashed lines include iSW measurements.

**Table 7.4.:** Marginal  $1\text{-}\sigma$  errors on cosmological parameters from a cosmic shear survey and the iSW effect, combined with a CMB prior. Also shown is the dark energy figure-of-merit.

Parameter	Stage III			Stage IV	
	CMB	3dWL+CMB	3dWL×iSW+CMB	3dWL+CMB	3dWL×iSW+CMB
$\Omega_m$	0.0139	0.0131	0.0131	0.0082	0.0081
$\sigma_8$	0.0133	0.0086	0.0086	0.0060	0.0059
$w_0$	0.2356	0.2000	0.1992	0.0937	0.0931
$w_a$	0.6588	0.5689	0.5666	0.2412	0.2397
$\Omega_b$	0.0021	0.0019	0.0019	0.0012	0.0012
$n_s$	0.0027	0.0020	0.0020	0.0018	0.0018
$h$	0.0148	0.0135	0.0135	0.0085	0.0085
FOM	54.1	76.3	76.6	311.6	313.9

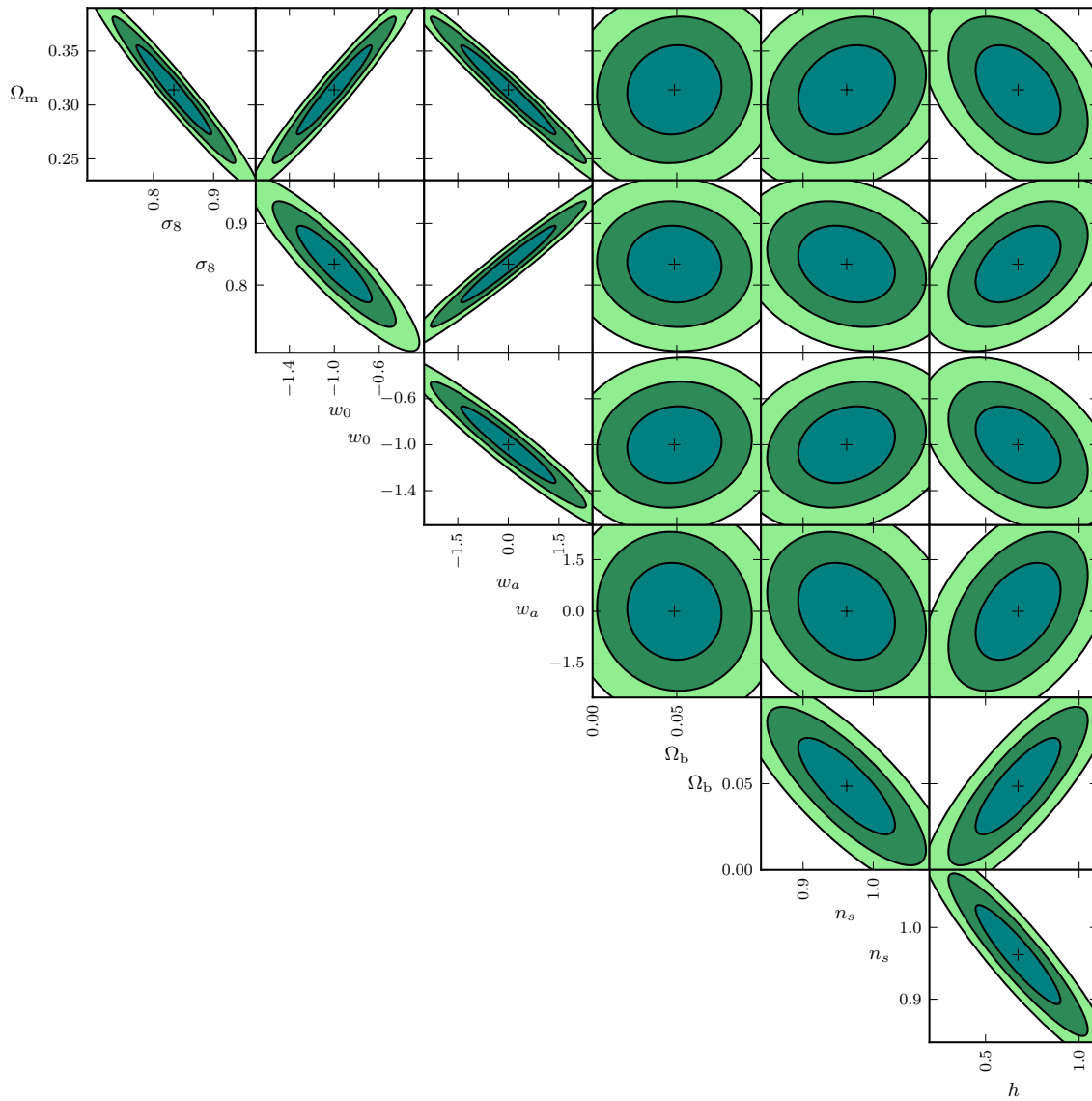


**Figure 7.8.:** Confidence regions for cosmological parameters derived from a stage IV weak lensing survey and iSW data. The 1-, 2- and 3- $\sigma$  ellipses are shown.

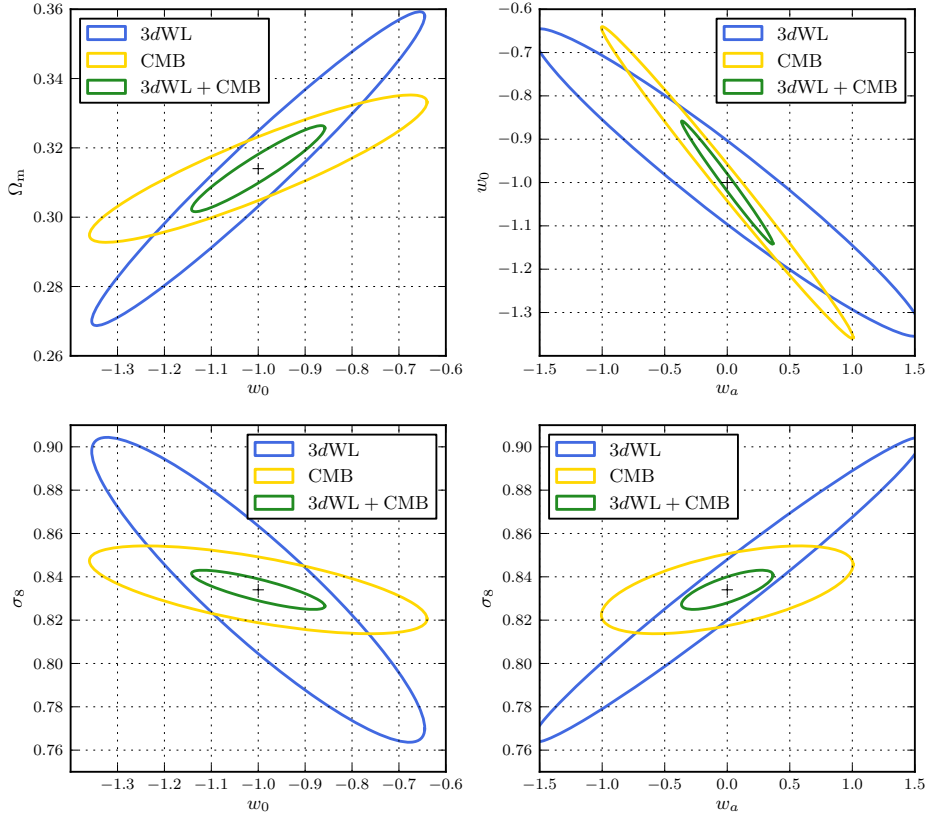


**Figure 7.9.:** 1- $\sigma$  confidence regions from a stage IV weak lensing survey and a CMB prior.

stage IV scenario improvements rise to up to 60 per cent. The correlations between cosmic shear and the integrated Sachs-Wolfe effect only affect the errors on  $w_0$  and  $w_a$  below the per cent level. The figure-of-merit increases by 40 per cent for the DES-like survey when information from weak lensing and the iSW effect is combined with the prior. For the Euclid-like scenario, the gain of a factor of six in the figure-of-merit is remarkable. Figure 7.9 illustrates the complementarity of CMB and cosmic shear surveys: while marginal errors derived from either of the two data sets alone are of the same order, the different degeneracies between parameters help improve the constraints.

## 7.7. Discussion

I have developed a formalism in which the three-dimensional cosmic shear field and its cross-correlations with the integrated Sachs-Wolfe effect can be analysed. These correlations arise because both the weak deflection leading to the former effect and the frequency shift giving rise to the latter are induced by massive structures along the line-of-sight and their evolution. While the iSW effect is observed as an anisotropy of the CMB, weak lensing manifests itself in the distortions of the images of distant galaxies. The variation with the source redshift constrains geometry and the time evolution of the density field; this sensitivity can be exploited by three-dimensional approaches, whereas tomographic studies and conventional two-dimensional analyses are unable to represent the full information.

The gain in information comes at the price of increased numerical complexity. The projected, two-dimensional shear field is statistically homogeneous and isotropic, unless partial sampling is taken into account. Thus in a spherical harmonic expansion multipoles of different order are independent. Statistical homogeneity is lost, however, if the radial dimension is included. The distance dependence of the lensing efficiency and the source density and the photometric redshift errors introduce correlations between the amplitudes of the signal on different scales; the covariance matrix then acquires off-diagonal

terms, the calculation of which is numerically involved. The basis of spherical Bessel functions leads to integrals with rapidly oscillatory kernels, which have to be solved for a large number of parameter combinations. Common quadrature methods based on interpolation generally do not meet requirements in speed and accuracy simultaneously for such a class of integrals; I have instead implemented a collocation method. The algorithm remains straightforward, avoiding e.g. the additional linear algebraic operations suggested by [Ayaita et al. \(2012\)](#). I have demonstrated how the iSW effect can be integrated into this formalism. The covariance matrix is then extended by the auto-correlation of the iSW signal and the cross-correlations between the observables.

I have exploited the speed of this approach in a Fisher analysis and presented error forecasts for seven cosmological parameters, studying two observational scenarios: a DES-like weak lensing survey with a median redshift of  $z_m = 0.7$  and a source density of  $n_0 = 12 \text{ arcmin}^{-2}$  across  $5,000 \text{ deg}^2$ , and a wider and somewhat deeper  $20,000 \text{ deg}^2$  survey with a galaxy density of  $n_0 = 40 \text{ arcmin}^{-2}$  around  $z_m = 0.9$ , representing the goals for the upcoming Euclid survey. A similar set of specifications was investigated by [Heavens et al. \(2006\)](#), whose results are reproduced in my independent implementation. I have demonstrated the complementarity of cosmic shear and the CMB by adding a CMB prior to the Fisher information: marginal errors improve by up to 60 per cent compared to constraints from the CMB alone, and most notably the dark energy figure-of-merit increases by a factor of six.

The systematics of weak lensing measurements have been discussed extensively elsewhere, in particular anisotropies of the point-spread function (see e.g. [Hoekstra, 2004](#); [Van Waerbeke et al., 2005](#); [Heymans et al., 2006b](#); [Jain et al., 2006](#)) and the calibration of shear measurements ([Guzik & Bernstein, 2005](#); [Massey et al., 2007](#); [Bridle et al., 2010](#)). [Kitching et al. \(2008b\)](#) identified uncertainties in the distribution of the redshift errors as the largest contaminant in three-dimensional weak lensing studies, measured by the effect on the figure-of-merit. Distortions due to the CCD, instrument effects or the measurement method were found to have a weaker influence. Corrections to the Born approximation have been shown to be small both analytically ([Dodelson et al., 2005](#); [Shapiro & Cooray, 2006](#); [Krause & Hirata, 2010](#)) and in simulations ([Jain et al., 2000](#); [Hilbert et al., 2009](#); [Becker, 2013](#)).

A challenge for cosmic shear studies is the description of the matter distribution on small scales. In the linear regime, the statistical properties of the density field are preserved, so that correlations between modes can be traced back to the linear matter power spectrum by the appropriate scaling with the growth function. Non-linear growth cannot be represented by such a scaling, since modes no longer evolve independently. Insufficient knowledge of the statistical structure of the matter distribution can bias results for the shear spectrum and cosmological parameters. [Jain & Seljak \(1997\)](#), for example, found that second-order statistics of the shear field were strongly affected by non-linearities on angular scales below  $10'$ , corresponding to multipole orders of  $\ell \gtrsim 2000$ . Deviations from a Gaussian likelihood were studied by [Takada & Jain \(2009\)](#) and [Sato & Nishimichi \(2013\)](#). [Jing et al. \(2006\)](#) showed that the effects of baryons on structure formation, such as radiative cooling and star formation, increased the power spectrum of (two-dimensional) cosmic shear by up to 10 per cent for multipoles  $\ell > 1000$ . [van Daalen et al. \(2011\)](#) similarly found that baryonic feedback lowered the matter power spectrum by a few percent in the range  $0.3 h \text{ Mpc}^{-1} \lesssim k \lesssim 1 h \text{ Mpc}^{-1}$ , and [Semboloni et al. \(2011\)](#) interpreted these results with respect to weak lensing tomography, cautioning that parameter biases might be as large as 40 per cent.

Intrinsic alignments are an additional uncertainty which becomes increasingly important on small scales (for a recent review, see [Troxel & Ishak, 2014b](#)). The formalism of cosmic shear is usually built on the assumption that correlations between image ellipticities are exclusively caused by gravitational lensing. Contrary to this hypothesis, finite correlations between the orientations of close pairs of galaxies, known as *II*-alignments, and anti-correlations with the gravitational shear, so-called *GI*-alignments, have been identified in numerical simulations ([Heavens et al., 2000](#); [Heymans et al., 2006a](#); [Kuhlen et al., 2007](#)) as well as in observations ([Brown et al., 2002](#); [Heymans et al., 2004](#); [Hirata et al., 2007](#); [Okumura et al., 2009](#)). Both types of alignments are attributed to the influence

of the local tidal field on galaxy formation and can mimic a shear signal. The relevance for weak lensing cosmography has been noted e.g. by Joachimi & Bridle (2010) and Kirk et al. (2010). Kirk et al. (2012) found the bias in the equation of state parameter  $w_0$  to be as large as  $8\text{--}20\sigma$ , but estimates vary depending on the modelling of the spurious contribution to the shear spectrum (cf. Bridle & King, 2007; Capranico et al., 2013), implying that the impact on cosmological constraints is still far from clear. For three-dimensional cosmic shear, Merkel & Schäfer (2013) presented auto- and cross-covariances of intrinsic and lensing-induced ellipticities. While  $II$ -alignments were shown to be the major contaminant for a Euclid-like survey with a median redshift of  $z_m = 0.9$ , the lensing signal was still an order of magnitude higher at the multipole order  $\ell = 200$ .

I have circumnavigated these obstacles by restricting the analysis to multipoles below  $\ell = 1000$  and radial modes up to  $k = 1 h \text{Mpc}^{-1}$ . These cuts entail that information from the smallest scales which can be probed by a Euclid-like survey becomes inaccessible, but its evaluation would otherwise be subject to substantial uncertainties. Valuable information is instead gained from the evolution of the large-scale structure along the line-of-sight, which can be resolved in the  $3d$  formalism, and the combination with an iSW experiment. As the iSW effect is observed on large scales, the cosmological sensitivity of the lowest multipoles is raised considerably, though it is still exceeded by the higher multipoles of weak lensing; the relative improvement in cosmological constraints achieved by the combination of data sets is thus higher for the stage III lensing survey, but even for the stage IV scenario marginal errors decrease by 10 per cent. I have demonstrated that this gain is largely due to the information in the cross-correlation: constraints are considerably weaker if the two data sets are treated as independent.

It is worth noting that the formalism presented here, including the numerical implementation, could easily be adapted to other cosmological effects. Analogies could be exploited in particular for a three-dimensional analysis of the brightness of the 21-cm line marking the hyperfine transition in neutral hydrogen clouds. The frequencies at which features are observed translate into redshifts of the corresponding emission or absorption events, effectively introducing a distance coordinate. The variations on the sky and the redshift dependence of the line brightness can then be studied in three dimensions, opening up the possibility of adding cross-correlations with other observables.



# 8

## Chapter 8

---

# Conclusions

In this dissertation, I have explored aspects of the interaction between light and the gravitational potential. A photon which crosses a potential well undergoes a change in its momentum, affecting both the direction of propagation and its energy. The deflection leads to the phenomenon known as gravitational lensing; the gravitational redshift gives rise to the integrated Sachs-Wolfe effect. Weak gravitational lensing induces elliptical distortions in the images of distant galaxies. The analysis of their shapes can thus constrain the distribution of matter in the foreground on different scales. The integrated Sachs-Wolfe effect manifests itself in a secondary anisotropy of the cosmic microwave background.

In the first part, I have demonstrated how gravitational lensing probes the internal structure of galaxy clusters. The simple theoretical model of spherical collapse predicts that the density of a virialised object in the expanding Universe reflects the matter density of the background at the time of formation. This relation already suggests that information about the history of structure formation is encoded in the densities of haloes. The spherical collapse model is, of course, highly idealised: density perturbations display neither such a perfect symmetry nor homogeneity. Consequently the shapes of haloes are better described as triaxial, with significant substructure. Instead of analytic approximations one must resort to numerical simulations to study the morphology of clusters. In cold dark matter scenarios haloes across a wide range of masses are consistently shown to feature a characteristic scale radius, within which the logarithmic slope of the density profile is shallow. The most common parametric model which describes this behaviour is the NFW profile, the logarithmic slope of which has constant asymptotes of  $-1$  in the centre and  $-3$  in the outskirts. It is frequently used as the basis for measurements of the scale radius or the concentration parameter: by comparing the prediction for the observable to the data, the profile parameters are determined by the best fit. Such approaches are prejudiced, as they are built on the null hypothesis that the mass distribution indeed follows the NFW profile. This hypothesis may be flawed in the presence of considerable substructure or deviations from spherical symmetry.

I have proposed a novel approach for the recovery of characteristic scales in density profiles. In the first step, an estimator of the surface mass density, or convergence, is obtained from the weak gravitational shear. This estimator is an integral measure; its value is the convergence smoothed with a circular aperture. No parametric profile is assumed, and the only information required is a shear catalogue.

The density profile is then described by means of excursion sets, i.e. the sets of all points at which the value of the estimator exceeds the respective threshold. The geometry of these excursion sets, in particular its change with varying thresholds, reflects features of the mass distribution. The morphology of spatial patterns in two dimensions is fully characterised by the three Minkowski functionals, which are integral, translation- and rotation-invariant geometric descriptors. In this work I have focused on the first Minkowski functional, which measures the area of the excursion set. If the underlying density profile is a power law, the logarithmic slope of the first Minkowski functional is constant;

for an NFW profile, however, the logarithmic slope decreases as a function of the threshold.

Using mock data, I have shown that measurements display considerable discrepancies from this behaviour, owing to the noise of the shear measurement. The density estimator is an implementation of the  $\zeta$ -statistics: the smoothed convergence is obtained from a weighted integral over the shear across the field. Noise arises from the intrinsic ellipticities of the sources, mimicking a shear signal, which cannot be disentangled from gravitational lensing. The variance of the density estimator over many realisations of the source distribution can be calculated from the weight function; as the shape of the weight function depends on the aperture position, the estimator acquires a characteristic, spatially-varying noise profile, marked by a steep rise of the variance near the borders of the field. Across much of the field the variance is at a nearly constant low level, but the values of neighbouring pixels are strongly correlated.

The noise level depends on the smoothing scale: if the aperture is small, the weight function is steep and the variance high; if the smoothing scale is large, the variance is low, but so is the signal, as features in the underlying mass distribution are smoothed out, and the correlation length increases. A natural choice for the smoothing scale is the Einstein radius of the lens, as it is a characteristic scale that can be obtained from observations. Moreover, it provides a point of reference for the Minkowski functional, as the convergence smoothed with the Einstein radius must not exceed unity.

It is far from obvious how the Minkowski functionals are affected by this noise, or how it can be suppressed. I have shown that the noise on average adds points to the excursion sets, so that the first Minkowski functional is overestimated at all thresholds. Even if the regions of the highest variance, i.e. the outskirts of the field, are excluded from the analysis, deviations from an ideal measurement persist up to thresholds where the scale radius becomes manifest. I have attributed this discrepancy to the structure of the excursion sets, imprinted by the noise profile of the  $\zeta$ -statistics. Up to high thresholds they consist of several connected components of large and intermediate size, reflecting the correlation length, as well as isolated pixels and small groups near the borders of the field. If only the largest connected component is considered, the Minkowski functional agrees remarkably well with an ideal measurement. The gap in size between this largest region representing the signal and the spurious components is so large that misidentifications are unlikely.

I have demonstrated how this strategy can be applied to discriminate between an NFW profile and an isothermal sphere. The latter is characterised by its Einstein radius, from which the Minkowski functional of the smoothed convergence can easily be predicted. By comparing the actual measurement to this prediction, the power law hypothesis can be tested. The scatter associated with noise is smaller than the difference between the Minkowski functionals of NFW and SIS haloes sharing the same Einstein radius, showing that a distinction between the two profiles is possible. This test could be extended to arbitrary power law profiles, so that families of profiles could be ruled out. While I have provided a proof of concept, an analysis of a much wider sample is needed in order to test the power of this method.

In the second part of the dissertation, I have studied the cross-correlation between weak lensing and the integrated Sachs-Wolfe effect. The iSW effect arises from the evolution of the large-scale structure at late epochs, when the contribution of dark energy (or the cosmological constant) to the density becomes appreciable. This evolution is also probed by cosmic shear, weak lensing of galaxies by the large-scale structure. Unlike lensing by galaxy clusters, cosmic shear is analysed statistically across a wide field.

In order to exploit the potential of cosmic shear to constrain the growth of structures and spacetime geometry, an analysis of the redshift-dependence of the signal is crucial. Current and upcoming surveys can supply adequate photometric measurements for this purpose. The heightened cosmological sensitivity is the key advantage of a fully three-dimensional formalism over tomographic studies. The numerical complexity, however, increases considerably. In three dimensions, the shear signal can be expanded in a basis of spin-weighted spherical harmonics and spherical Bessel functions. Not only is the covariance matrix then larger than in two-dimensional studies, its structure is also more com-

plex. The projected shear field is statistically isotropic, so that the covariance matrix is diagonal. The three-dimensional observable, however, is not statistically homogeneous due to the radial weighting resulting from the distance-dependence of the lensing efficiency, the source-redshift distribution and the dispersion of the photometric redshifts. The loss of statistical homogeneity leads to mode coupling, i.e. finite covariances between different radial modes, rendering the calculation of the covariance matrix expensive. In addition to the large number of required operations, the numerical integration of highly oscillatory functions is particularly demanding. I have suggested a collocation method, which exploits recurrence relations of the spherical Bessel functions that appear in the kernels. This algorithm achieves an excellent accuracy with fewer nodes and therefore faster than common interpolation-based quadrature rules.

My analysis has been restricted to multipoles up to  $\ell = 1000$  and radial wavenumbers below  $k = 1 h \text{Mpc}^{-1}$ , avoiding several uncertainties associated with smaller scales. Modes above these cuts have entered the non-linear regime of structure formation, so that an adequate description of the non-linear matter power spectrum is needed, in particular the coupling between modes of the density contrast at different epochs. If baryonic effects are not taken into account, cosmological parameters derived from an analysis which includes these small scales will be biased. Moreover, intrinsic alignments – finite auto-correlations of the intrinsic shapes of galaxies and cross-correlations with the cosmic shear signal – become increasingly important on small scales and can similarly create parameter biases. In principle, the cosmological sensitivity of cosmic shear is high on these scales. Although this information is unavailable if they are excluded, the loss is made up for by the potential of a three-dimensional study to probe the time-evolution of the matter distribution on larger scales, even more so if the cross-correlation between cosmic shear and the iSW effect is also considered. While the latter cannot resolve the growth of structures along the line-of-sight, the signal can be expanded into multipoles, which are correlated with shear modes of the same order; due to statistical isotropy there is no mixing between multipoles of different order.

In order to explore the impact of the additional information encoded in the iSW signal and its cross-correlation with the three-dimensional cosmic shear field on cosmological parameter errors, I have carried out a Fisher analysis, considering DES-like (research stage III) and Euclid-like (stage IV) weak lensing surveys. The iSW effect clearly raises the cosmological sensitivity at the lowest multipole orders. I have been able to demonstrate that the cross-correlation in particular adds valuable information and helps break degeneracies. Marginal errors improve by up to 50 per cent for stage III specifications, but they remain large, about a factor of four higher than for the Euclid-like survey. For the latter, the inclusion of iSW data tightens constraints on  $\Omega_m$ ,  $\sigma_8$ ,  $w_0$  and  $w_a$  by about ten per cent and increases the dark energy figure-of-merit by 17 per cent; the gain is negligible if correlations are ignored. Narrow constraints can be achieved for both scenarios in combination with a CMB prior. CMB data open up the possibility of extending the covariance matrix by the cross-correlation between cosmic shear and CMB lensing, enhancing the cosmological sensitivity even further.



# A

## Appendix A

### Parametrisation of Nested Curves

To calculate the smoothed convergence

$$\Delta\bar{\kappa}(\mathbf{x}_0) = \int db b \oint d\lambda \left\{ \left[ \frac{W(b)}{b^2} - \frac{w(b)}{b} \right] \mathfrak{I} [(C'\dot{C})^* \gamma] + \frac{W(b)}{b} \mathfrak{I} [(C'\dot{C}' - C''\dot{C})^* \gamma] \right\} \quad (\text{A.1})$$

for the geometry presented in Sec. 5.3.1, the filter function  $w$  and its integral  $W$  as well as the nested curves  $C(b, \lambda)$  and their first and second derivatives must be calculated. The aperture position is  $M = x + iy$ . Closed curves are parametrised by Eq. (5.31):

$$\hat{C}(\hat{b}, \hat{\lambda}) = [R + \hat{b}t(\hat{\lambda})] e^{i\hat{\lambda}}, \quad \hat{b} \in [0, 1], \quad \hat{\lambda} \in [0, 2\pi]. \quad (\text{A.2})$$

$t(\hat{\lambda})$  is more easily expressed in terms of  $s(\varphi) = t[\hat{\lambda}(\varphi)] + R$ .  $s(\varphi)$  is defined piecewise as follows:

$$s(\varphi) = \begin{cases} -\frac{a/2 + x}{\cos \varphi} & \text{if } \varphi \leq \varphi_1 \text{ or } \varphi \geq \varphi_8 \\ f(\varphi, R - \frac{a}{2} - x, R - \frac{b}{2} - y) & \text{if } \varphi_1 < \varphi < \varphi_2 \\ -\frac{b/2 + y}{\sin \varphi} & \text{if } \varphi_2 \leq \varphi \leq \varphi_3 \\ f(\varphi, \frac{a}{2} - R - x, R - \frac{b}{2} - y) & \text{if } \varphi_3 < \varphi < \varphi_4 \\ \frac{a/2 - x}{\cos \varphi} & \text{if } \varphi_4 \leq \varphi \leq \varphi_5 \\ f(\varphi, \frac{a}{2} - R - x, \frac{b}{2} - R - y) & \text{if } \varphi_5 < \varphi < \varphi_6 \\ \frac{b/2 - y}{\sin \varphi} & \text{if } \varphi_6 \leq \varphi \leq \varphi_7 \\ f(\varphi, R - \frac{a}{2} - x, \frac{b}{2} - R - y) & \text{if } \varphi_7 < \varphi < \varphi_8 \end{cases}. \quad (\text{A.3})$$

The angles  $\varphi_i$  are the angles of the transitions between the straight sides and the circular arcs replacing the corners of the rectangle:

$$\begin{aligned} \varphi_1 &= \arctan \frac{R - b/2 - y}{-a/2 - x} - \pi; & \varphi_2 &= \arctan \frac{-b/2 - y}{R - a/2 - x} - \pi; \\ \varphi_3 &= \arctan \frac{-b/2 - y}{a/2 - R - x}; & \varphi_4 &= \arctan \frac{R - b/2 - y}{a/2 - x}; \\ \varphi_5 &= \arctan \frac{b/2 - R - y}{a/2 - x}; & \varphi_6 &= \arctan \frac{b/2 - y}{a/2 - R - x}; \\ \varphi_7 &= \arctan \frac{b/2 - y}{R - a/2 - x} + \pi; & \varphi_8 &= \arctan \frac{b/2 - R - y}{-a/2 - x} + \pi. \end{aligned} \quad (\text{A.4})$$

For the numbering see Fig. 5.1. The function  $f(\varphi, \Delta x, \Delta y)$  describes the quarter-circles at the corners:

$$f(\varphi, \Delta x, \Delta y) = \Delta x \cos \varphi + \Delta y \sin \varphi + \sqrt{R^2 - (\Delta x \sin \varphi - \Delta y \cos \varphi)^2}, \quad (\text{A.5})$$

with the derivatives

$$\begin{aligned} \dot{f}(\varphi, \Delta x, \Delta y) &= -\Delta x \sin \varphi + \Delta y \cos \varphi \\ &\quad - \frac{(\Delta x \cos \varphi + \Delta y \sin \varphi)(\Delta x \sin \varphi - \Delta y \cos \varphi)}{\sqrt{R^2 - (\Delta x \sin \varphi - \Delta y \cos \varphi)^2}}, \end{aligned} \quad (\text{A.6})$$

$$\begin{aligned} \ddot{f}(\varphi, \Delta x, \Delta y) &= -\Delta x \cos \varphi - \Delta y \sin \varphi \\ &\quad - \frac{(\Delta x \cos \varphi + \Delta y \sin \varphi)^2 (\Delta x \sin \varphi - \Delta y \cos \varphi)^2}{\left[ R^2 - (\Delta x \sin \varphi - \Delta y \cos \varphi)^2 \right]^{\frac{3}{2}}} \\ &\quad - \frac{(\Delta x \cos \varphi + \Delta y \sin \varphi)^2 - (\Delta x \sin \varphi - \Delta y \cos \varphi)^2}{\sqrt{R^2 - (\Delta x \sin \varphi - \Delta y \cos \varphi)^2}}. \end{aligned} \quad (\text{A.7})$$

The derivatives  $\dot{s}$  and  $\ddot{s}$  for straight sections are easily calculated using

$$\begin{aligned} \frac{d}{d\varphi} \left( \frac{1}{\cos \varphi} \right) &= \frac{\sin \varphi}{\cos^2 \varphi}, & \frac{d^2}{d\varphi^2} \left( \frac{1}{\cos \varphi} \right) &= \frac{1}{\cos \varphi} (1 + 2 \tan^2 \varphi), \\ \frac{d}{d\varphi} \left( \frac{1}{\sin \varphi} \right) &= -\frac{\cos \varphi}{\sin^2 \varphi}, & \frac{d^2}{d\varphi^2} \left( \frac{1}{\sin \varphi} \right) &= \frac{1}{\sin \varphi} \left( 1 + \frac{2}{\tan^2 \varphi} \right). \end{aligned} \quad (\text{A.8})$$

In the nomenclature of Sec. 5.2.2,  $\lambda_{\max} = 2\pi$ . As the coordinate  $b$  is defined by  $\lambda_{\max} b^2 = 2A(\hat{b})$  (Eq. 5.20), the aperture border corresponds to  $b_1 = R$ , while the smoothed rectangle has  $\pi b_2^2 = ab - (4 - \pi)R^2$ . The filter function (Eq. 5.30) is

$$w(b) = \begin{cases} \frac{1}{\pi R^2} & \text{if } b \leq b_1 \\ -\frac{1}{ab - 4R^2} & \text{if } b_1 < b \leq b_2 \\ 0 & \text{if } b > b_2 \end{cases} \quad (\text{A.9})$$

with the integral

$$W(b) = \begin{cases} \frac{b}{2\pi R^2} & \text{if } b \leq b_1 \\ \frac{1}{2\pi b} - \frac{b^2 - R^2}{2(ab - 4R^2)b} & \text{if } b_1 < b \leq b_2 \\ 0 & \text{if } b > b_2 \end{cases}. \quad (\text{A.10})$$

The integral then simplifies to

$$\Delta \bar{\kappa}(\mathbf{x}_0) = \frac{1}{2(ab - 4R^2)} \int_{b_1}^{b_2} db b \oint d\lambda \left\{ \frac{b_2^2 + b^2}{b^3} \Im [(C' \dot{C})^* \gamma] + \frac{b_2^2 - b^2}{b^2} \Im [(C' \dot{C}' - C'' \dot{C})^* \gamma] \right\}. \quad (\text{A.11})$$

The remaining task is the calculation of the derivatives of  $C$ . Any calculus operations could of course be performed numerically, but as the weight function must be calculated at a large number of points and for many different aperture positions, it is worth searching for analytic expressions. With respect to the coordinates  $\hat{b}$  and  $\hat{\lambda}$ ,

$$\partial_{\hat{b}} \hat{C} = t e^{i\hat{\lambda}}; \quad (\text{A.12})$$

$$\partial_{\hat{b}}^2 \hat{C} = 0; \quad (\text{A.13})$$

$$\partial_{\hat{b}} \partial_{\hat{\lambda}} \hat{C} = (i + it) e^{i\hat{\lambda}}; \quad (\text{A.14})$$

$$\partial_{\hat{\lambda}} \hat{C} = [\hat{b}t + i(R + \hat{b}t)] e^{i\hat{\lambda}}; \quad (\text{A.15})$$

$$\partial_{\hat{\lambda}}^2 \hat{C} = [\hat{b}\dot{t} + 2i\hat{b}t - (R + \hat{b}t)] e^{i\hat{\lambda}}. \quad (\text{A.16})$$

In the new coordinate system made up by  $b$  and  $\lambda$ , the derivative operators are

$$\begin{aligned}\partial_b &= \left(\frac{db}{d\hat{b}}\right)^{-1} \partial_{\hat{b}} - \left(\frac{db}{d\hat{b}} \frac{\partial \lambda}{\partial \hat{\lambda}}\right)^{-1} \partial_{\hat{\lambda}}, \\ \partial_{\lambda} &= \left(\frac{\partial \lambda}{\partial \hat{\lambda}}\right)^{-1} \partial_{\hat{\lambda}}.\end{aligned}\quad (\text{A.17})$$

The derivatives of the coordinate transform are listed below. The prime and dot symbols denote derivatives with respect to  $\hat{b}$  and  $\hat{\lambda}$ , respectively.

$$b = \left[ \frac{1}{2\pi} \int_0^{2\pi} d\tilde{\lambda} (R + \hat{b}t)^2 \right]^{\frac{1}{2}}; \quad (\text{A.18})$$

$$b' = \frac{1}{2\pi b} \int_0^{2\pi} d\tilde{\lambda} t (R + \hat{b}t); \quad (\text{A.19})$$

$$b'' = -\frac{b'^2}{b} + \frac{1}{2\pi b} \int_0^{2\pi} d\tilde{\lambda} t^2; \quad (\text{A.20})$$

$$\lambda = \frac{1}{bb'} \int_0^{\hat{\lambda}} d\tilde{\lambda} t (R + \hat{b}t); \quad (\text{A.21})$$

$$\dot{\lambda} = \frac{t(R + \hat{b}t)}{bb'}; \quad (\text{A.22})$$

$$\ddot{\lambda} = \frac{iR + 2\hat{b}t\dot{t}}{bb'}; \quad (\text{A.23})$$

$$\lambda' = \frac{1}{bb'} \left[ \int_0^{\hat{\lambda}} d\tilde{\lambda} t^2 - \frac{\lambda}{2\pi} \int_0^{2\pi} d\tilde{\lambda} t^2 \right]; \quad (\text{A.24})$$

$$\lambda'' = -2\lambda' \left( \frac{b''}{b'} + \frac{b'}{b} \right); \quad (\text{A.25})$$

$$\dot{\lambda}' = \frac{t^2}{bb'} + \frac{\lambda'' \dot{\lambda}}{2\lambda'}. \quad (\text{A.26})$$

In these expressions integrals of  $t$  and  $t^2$  appear. Results for the straight edges can be found quickly:

$$\begin{aligned}\int d\varphi \frac{1}{\cos \varphi} &= \ln \left| \frac{1 + \sin \varphi}{\cos \varphi} \right|, & \int d\varphi \frac{1}{\cos^2 \varphi} &= \tan \varphi, \\ \int d\varphi \frac{1}{\sin \varphi} &= \ln \left| \frac{\sin \varphi}{1 + \cos \varphi} \right|, & \int d\varphi \frac{1}{\sin^2 \varphi} &= -\frac{1}{\tan \varphi}.\end{aligned}\quad (\text{A.27})$$

Finally, analytic integrals exist also for the ‘corners’:

$$\begin{aligned}\int d\varphi f(\varphi, \Delta x, \Delta y) &= \Delta x \sin \varphi - \Delta y \cos \varphi \\ &+ R E \left[ \arcsin \sqrt{\frac{(\Delta x \sin \varphi - \Delta y \cos \varphi)^2}{\Delta x^2 + \Delta y^2}}, \sqrt{\frac{\Delta x^2 + \Delta y^2}{R^2}} \right],\end{aligned}\quad (\text{A.28})$$

$$\begin{aligned}\int d\varphi f^2(\varphi, \Delta x, \Delta y) &= \frac{\Delta x^2 - \Delta y^2}{2} \sin 2\varphi - \Delta x \Delta y \cos 2\varphi + R^2 \varphi \\ &+ (\Delta x \sin \varphi - \Delta y \cos \varphi) \sqrt{R^2 - (\Delta x \sin \varphi - \Delta y \cos \varphi)^2} \\ &+ R^2 \arctan \frac{(\Delta x \sin \varphi - \Delta y \cos \varphi)}{\sqrt{R^2 - (\Delta x \sin \varphi - \Delta y \cos \varphi)^2}}.\end{aligned}\quad (\text{A.29})$$

$E$  denotes the incomplete elliptic integral of the second kind, defined by

$$E(\varphi, k) = \int_0^\varphi d\theta \sqrt{1 - k^2 \sin^2 \theta}. \quad (\text{A.30})$$

Libraries often require  $k \leq 1$  for the evaluation, although the integral is well defined for  $k > 1$  provided that  $\sin \theta \leq \sin \varphi \leq 1/k$ . In the latter case the reciprocal modulus transformation can be used ([Abramowitz et al., 1988](#)):

$$E\left(\varphi, \frac{1}{k}\right) = \frac{1}{k} [E(\beta, k) - (1 - k^2)F(\beta, k)], \quad (\text{A.31})$$

where  $k \sin \beta = \sin \varphi$  and

$$F(\varphi, k) = \int_0^\varphi \frac{d\theta}{\sqrt{1 - k^2 \sin^2 \theta}} \quad (\text{A.32})$$

is the incomplete elliptic integral of the first kind.

# Bibliography

- Abdalla, F. B., Amara, A., Capak, P., et al. 2008, MNRAS, 387, 969
- Abramowitz, M., Stegun, I. A., & Romer, R. H. 1988, Am. J. Phys., 56, 958
- Aghanim, N., Majumdar, S., & Silk, J. 2008, Rep. Prog. Phys., 71, 066902
- Albrecht, A., Bernstein, G., Cahn, R., et al. 2006, ArXiv e-prints, arXiv:0609591
- Albrecht, A., Amendola, L., Bernstein, G., et al. 2009, ArXiv e-prints, arXiv:0901.0721
- Amendola, L., Kunz, M., & Sapone, D. 2008, J. Cosmol. Astropart. Phys., 4, 13
- Amendola, L., & Tsujikawa, S. 2010, Dark Energy: Theory and Observations (Cambridge University Press)
- Angulo, R. E., Springel, V., White, S. D. M., et al. 2012, MNRAS, 426, 2046
- Athreya, R. M., Mellier, Y., van Waerbeke, L., et al. 2002, A&A, 384, 743
- Ayaita, Y., Schäfer, B. M., & Weber, M. 2012, MNRAS, 422, 3056
- Bacon, D. J., Goldberg, D. M., Rowe, B. T. P., & Taylor, A. N. 2006, MNRAS, 365, 414
- Bacon, D. J., Refregier, A. R., & Ellis, R. S. 2000, MNRAS, 318, 625
- Bardeen, J. M., Bond, J. R., Kaiser, N., & Szalay, A. S. 1986, ApJ, 304, 15
- Bartelmann, M. 1995, A&A, 299, 11
- Bartelmann, M. 1996, A&A, 313, 697
- Bartelmann, M. 2010a, Rev. Mod. Phys., 82, 331
- Bartelmann, M. 2010b, Class. Quantum Grav., 27, 233001
- Bartelmann, M., & Meneghetti, M. 2004, A&A, 418, 413
- Bartelmann, M., Narayan, R., Seitz, S., & Schneider, P. 1996, ApJ, 464, L115
- Bartelmann, M., & Schneider, P. 2001, Phys. Rep., 340, 291
- Baugh, C. M., & Efstathiou, G. 1993, MNRAS, 265, 145
- Becker, M. R. 2013, MNRAS, 435, 115
- Bennett, C. L., Larson, D., Weiland, J. L., et al. 2013, ApJS, 208, 20
- Bergmann, A. G., Petrosian, V., & Lynds, R. 1990, ApJ, 350, 23
- Bernardeau, F., van Waerbeke, L., & Mellier, Y. 1997, A&A, 322, 1
- Bernstein, G., & Jain, B. 2004, ApJ, 600, 17

## BIBLIOGRAPHY

---

- Blake, C., James, J. B., & Poole, G. B. 2014, *MNRAS*, 437, 2488
- Blandford, R. D., Saust, A. B., Brainerd, T. G., & Villumsen, J. V. 1991, *MNRAS*, 251, 600
- Blas, D., Lesgourgues, J., & Tram, T. 2011, *J. Cosmol. Astropart. Phys.*, 7, 34
- Boughn, S., & Crittenden, R. 2004, *Nature*, 427, 45
- Boylan-Kolchin, M., Springel, V., White, S. D. M., Jenkins, A., & Lemson, G. 2009, *MNRAS*, 398, 1150
- Bradač, M., Schneider, P., Lombardi, M., & Erben, T. 2005a, *A&A*, 437, 39
- Bradač, M., Erben, T., Schneider, P., et al. 2005b, *A&A*, 437, 49
- Bradač, M., Clowe, D., Gonzalez, A. H., et al. 2006, *ApJ*, 652, 937
- Bridle, S., & King, L. 2007, *New J. Phys.*, 9, 444
- Bridle, S., Balan, S. T., Bethge, M., et al. 2010, *MNRAS*, 405, 2044
- Broadhurst, T., Umetsu, K., Medezinski, E., Oguri, M., & Rephaeli, Y. 2008, *ApJ*, 685, L9
- Broadhurst, T., Benítez, N., Coe, D., et al. 2005, *ApJ*, 621, 53
- Brown, M. L., Taylor, A. N., Hambly, N. C., & Dye, S. 2002, *MNRAS*, 333, 501
- Bryan, G. L., & Norman, M. L. 1998, *ApJ*, 495, 80
- Bullock, J. S., Kolatt, T. S., Sigad, Y., et al. 2001, *MNRAS*, 321, 559
- Cabré, A., Gaztañaga, E., Manera, M., Fosalba, P., & Castander, F. 2006, *MNRAS*, 372, L23
- Cacciato, M., Bartelmann, M., Meneghetti, M., & Moscardini, L. 2006, *A&A*, 458, 349
- Capranico, F., Merkel, P. M., & Schäfer, B. M. 2013, *MNRAS*, 435, 194
- Carroll, S. M. 2001, *Living Rev. Relat.*, 4, 1
- Castro, P. G., Heavens, A. F., & Kitching, T. D. 2005, *Phys. Rev. D*, 72, 023516
- Chevallier, M., & Polarski, D. 2001, *Int. J. Mod. Phys. D*, 10, 213
- Clowe, D., De Lucia, G., & King, L. 2004, *MNRAS*, 350, 1038
- Clowe, D., Luppino, G. A., Kaiser, N., & Gioia, I. M. 2000, *ApJ*, 539, 540
- Clowe, D., & Schneider, P. 2001, *A&A*, 379, 384
- Coble, K., Dodelson, S., & Frieman, J. A. 1997, *Phys. Rev. D*, 55, 1851
- Comerford, J. M., & Natarajan, P. 2007, *MNRAS*, 379, 190
- Cooray, A. 2002, *Phys. Rev. D*, 65, 103510
- Cramér, H. 1974, *Mathematical methods of statistics* (Princeton University Press)
- Dodelson, S. 2003, *Modern cosmology* (Academic Press)
- Dodelson, S., Kolb, E. W., Matarrese, S., Riotto, A., & Zhang, P. 2005, *Phys. Rev. D*, 72, 103004

- Durrer, R. 2008, *The Cosmic Microwave Background* (Cambridge University Press)
- Einstein, A. 1915, *Sitzungsberichte der Königlich Preußischen Akademie der Wissenschaften (Berlin)*, 778
- Eisenstein, D. J., & Hu, W. 1998, *ApJ*, 496, 605
- Eisenstein, D. J., & Hu, W. 1999, *ApJ*, 511, 5
- Eke, V. R., Navarro, J. F., & Steinmetz, M. 2001, *ApJ*, 554, 114
- Fahlman, G., Kaiser, N., Squires, G., & Woods, D. 1994, *ApJ*, 437, 56
- Falco, E. E., Gorenstein, M. V., & Shapiro, I. I. 1985, *ApJ*, 289, L1
- Fedeli, C., Bartelmann, M., Meneghetti, M., & Moscardini, L. 2007, *A&A*, 473, 715
- Fort, B., Le Fevre, O., Hammer, F., & Cailloux, M. 1992, *ApJ*, 399, L125
- Fosalba, P., Gaztañaga, E., & Castander, F. J. 2003, *ApJ*, 597, L89
- Friedmann, A. 1922, *Zeitschrift für Physik*, 10, 377
- Friedmann, A. 1924, *Zeitschrift für Physik*, 21, 326
- Frieman, J. A., Turner, M. S., & Huterer, D. 2008, *ARA&A*, 46, 385
- Gao, L., Navarro, J. F., Cole, S., et al. 2008, *MNRAS*, 387, 536
- Gavazzi, R. 2005, *A&A*, 443, 793
- Gavazzi, R., Fort, B., Mellier, Y., Pelló, R., & Dantel-Fort, M. 2003, *A&A*, 403, 11
- Gaztañaga, E., Manera, M., & Multamäki, T. 2006, *MNRAS*, 365, 171
- Giallongo, E., Ragazzoni, R., Grazian, A., et al. 2008, *A&A*, 482, 349
- Giannantonio, T., Ross, A. J., Percival, W. J., et al. 2014, *Phys. Rev. D*, 89, 023511
- Giannantonio, T., Scranton, R., Crittenden, R. G., et al. 2008, *Phys. Rev. D*, 77, 123520
- Giannantonio, T., Crittenden, R. G., Nichol, R. C., et al. 2006, *Phys. Rev. D*, 74, 063520
- Goldberg, D. M., & Bacon, D. J. 2005, *ApJ*, 619, 741
- Grossman, S. A., & Narayan, R. 1988, *ApJ*, 324, L37
- Guzik, J., & Bernstein, G. 2005, *Phys. Rev. D*, 72, 043503
- Hadwiger, H. 1957, *Vorlesungen über Inhalt, Oberfläche und Isoperimetrie* (Springer)
- Hall, A., & Taylor, A. 2014, *MNRAS*, 443, L119
- Hammer, F. 1991, *ApJ*, 383, 66
- Hammer, F., & Rigaut, F. 1989, *A&A*, 226, 45
- Hammer, F., Rigaut, F., Le Fevre, O., Jones, J., & Soucail, G. 1989, *A&A*, 208, L7
- Hand, N., Leauthaud, A., Das, S., et al. 2015, *Phys. Rev. D*, 91, 062001

## BIBLIOGRAPHY

---

- Hannestad, S., Tu, H., & Wong, Y. Y. 2006, *J. Cosmol. Astropart. Phys.*, 6, 25
- Harrison, E. R. 1970, *Phys. Rev. D*, 1, 2726
- Hattori, M., Matuzawa, H., Morikawa, K., et al. 1998, *ApJ*, 503, 593
- Hayashi, E., & White, S. D. M. 2008, *MNRAS*, 388, 2
- Heavens, A. 2003, *MNRAS*, 343, 1327
- Heavens, A., Refregier, A., & Heymans, C. 2000, *MNRAS*, 319, 649
- Heavens, A. F., Kitching, T. D., & Taylor, A. N. 2006, *MNRAS*, 373, 105
- Hennawi, J. F., Dalal, N., Bode, P., & Ostriker, J. P. 2007, *ApJ*, 654, 714
- Heymans, C., Brown, M., Heavens, A., et al. 2004, *MNRAS*, 347, 895
- Heymans, C., White, M., Heavens, A., Vale, C., & van Waerbeke, L. 2006a, *MNRAS*, 371, 750
- Heymans, C., Van Waerbeke, L., Bacon, D., et al. 2006b, *MNRAS*, 368, 1323
- Heymans, C., Grocutt, E., Heavens, A., et al. 2013, *MNRAS*, 432, 2433
- Hikage, C., Komatsu, E., & Matsubara, T. 2006, *ApJ*, 653, 11
- Hikage, C., Matsubara, T., Coles, P., et al. 2008, *MNRAS*, 389, 1439
- Hikage, C., Schmalzing, J., Buchert, T., et al. 2003, *PASJ*, 55, 911
- Hilbert, S., Hartlap, J., White, S. D. M., & Schneider, P. 2009, *A&A*, 499, 31
- Hirata, C. M., Mandelbaum, R., Ishak, M., et al. 2007, *MNRAS*, 381, 1197
- Ho, S., Hirata, C., Padmanabhan, N., Seljak, U., & Bahcall, N. 2008, *Phys. Rev. D*, 78, 043519
- Hoekstra, H. 2003, *MNRAS*, 339, 1155
- Hoekstra, H. 2004, *MNRAS*, 347, 1337
- Hoekstra, H., Franx, M., Kuijken, K., & Squires, G. 1998, *ApJ*, 504, 636
- Hoekstra, H., Yee, H. K. C., & Gladders, M. D. 2002, *New A Rev.*, 46, 767
- Hollenstein, L., Sapone, D., Crittenden, R., & Schäfer, B. M. 2009, *J. Cosmol. Astropart. Phys.*, 4, 12
- Hu, W. 1999, *ApJ*, 522, L21
- Hu, W., & Sugiyama, N. 1994, *Phys. Rev. D*, 50, 627
- Hubble, E. 1929, *Proc. Natl. Acad. Sci.*, 15, 168
- Hubble, E., & Humason, M. L. 1931, *ApJ*, 74, 43
- Hubble, E. P. 1936, *Realm of the Nebulae* (Yale University Press)
- Huterer, D. 2002, *Phys. Rev. D*, 65, 063001
- Huterer, D. 2010, *Gen. Relat. Grav.*, 42, 2177
- Ilbert, O., Arnouts, S., McCracken, H. J., et al. 2006, *A&A*, 457, 841

- Jain, B., Jarvis, M., & Bernstein, G. 2006, *J. Cosmol. Astropart. Phys.*, 2, 1
- Jain, B., & Seljak, U. 1997, *ApJ*, 484, 560
- Jain, B., Seljak, U., & White, S. 2000, *ApJ*, 530, 547
- Jain, B., & Taylor, A. 2003, *Phys. Rev. Lett.*, 91, 141302
- Jee, M. J., Tyson, J. A., Schneider, M. D., et al. 2013, *ApJ*, 765, 74
- Jing, Y. P. 2000, *ApJ*, 535, 30
- Jing, Y. P., & Suto, Y. 2002, *ApJ*, 574, 538
- Jing, Y. P., Zhang, P., Lin, W. P., Gao, L., & Springel, V. 2006, *ApJ*, 640, L119
- Joachimi, B., & Bridle, S. L. 2010, *A&A*, 523, A1
- Kaiser, N. 1992, *ApJ*, 388, 272
- Kaiser, N. 1995, *ApJ*, 439, L1
- Kaiser, N. 1998, *ApJ*, 498, 26
- Kaiser, N., & Squires, G. 1993, *ApJ*, 404, 441
- Kaiser, N., Squires, G., & Broadhurst, T. 1995, *ApJ*, 449, 460
- Kaiser, N., Wilson, G., & Luppino, G. A. 2000, *ArXiv e-prints*, arXiv:0003338
- Kassiola, A., Kovner, I., & Blandford, R. D. 1992, *ApJ*, 396, 10
- Kerscher, M., Schmalzing, J., Retzlaff, J., et al. 1997, *MNRAS*, 284, 73
- Kilbinger, M., Benabed, K., Guy, J., et al. 2009, *A&A*, 497, 677
- Kilbinger, M., Fu, L., Heymans, C., et al. 2013, *MNRAS*, 430, 2200
- Kim, J., Park, C., Gott, III, J. R., & Dubinski, J. 2009, *ApJ*, 701, 1547
- Kim, J., Park, C., Rossi, G., Lee, S. M., & Gott, III, J. R. 2011, *J. Kor. Astron. Soc.*, 44, 217
- King, L. J., & Schneider, P. 2001, *A&A*, 369, 1
- King, L. J., Schneider, P., & Springel, V. 2001, *A&A*, 378, 748
- Kirk, D., Bridle, S., & Schneider, M. 2010, *MNRAS*, 408, 1502
- Kirk, D., Rassat, A., Host, O., & Bridle, S. 2012, *MNRAS*, 424, 1647
- Kitching, T. D., Heavens, A. F., & Das, S. 2014a, *ArXiv e-prints*, arXiv:1408.7052
- Kitching, T. D., Heavens, A. F., & Miller, L. 2011, *MNRAS*, 413, 2923
- Kitching, T. D., Heavens, A. F., Taylor, A. N., et al. 2007, *MNRAS*, 376, 771
- Kitching, T. D., Miller, L., Heymans, C. E., van Waerbeke, L., & Heavens, A. F. 2008a, *MNRAS*, 390, 149
- Kitching, T. D., Taylor, A. N., & Heavens, A. F. 2008b, *MNRAS*, 389, 173

## BIBLIOGRAPHY

---

- Kitching, T. D., Heavens, A. F., Alsing, J., et al. 2014b, *MNRAS*, 442, 1326
- Klypin, A. A., Trujillo-Gomez, S., & Primack, J. 2011, *ApJ*, 740, 102
- Kneib, J.-P., & Natarajan, P. 2011, *A&A Rev.*, 19, 47
- Kneib, J.-P., Hudelot, P., Ellis, R. S., et al. 2003, *ApJ*, 598, 804
- Koecher, M. 1992, *Lineare Algebra und analytische Geometrie* (Springer)
- Konrad, S., Majer, C. L., Meyer, S., Sarli, E., & Bartelmann, M. 2013, *A&A*, 553, A118
- Kovner, I. 1989, *ApJ*, 337, 621
- Kratochvil, J. M., Lim, E. A., Wang, S., et al. 2012, *Phys. Rev. D*, 85, 103513
- Krause, E., & Hirata, C. M. 2010, *A&A*, 523, A28
- Kuhlen, M., Diemand, J., & Madau, P. 2007, *ApJ*, 671, 1135
- Langlois, D. 2010, *Lect. Notes Phys.*, 800, 1
- Laureijs, R., Amiaux, J., Arduini, S., et al. 2011, *ArXiv e-prints*, arXiv:1110.3193
- Levin, D. 1996, *J. Comput. Appl. Math.*, 67, 95
- Levin, D. 1997, *J. Comput. Appl. Math.*, 78, 131
- Lewis, A., & Challinor, A. 2006, *Phys. Rep.*, 429, 1
- Liddle, A. R. 1999, *ArXiv e-prints*, arXiv:9901124
- Liddle, A. R., & Lyth, D. H. 2000, *Cosmological Inflation and Large-Scale Structure* (Cambridge University Press)
- Limber, D. N. 1953, *ApJ*, 117, 134
- Limber, D. N. 1954, *ApJ*, 119, 655
- Linder, E. V. 2003, *Phys. Rev. Lett.*, 90, 091301
- Linder, E. V., & Jenkins, A. 2003, *MNRAS*, 346, 573
- Lovelock, D. 1971, *J. Math. Phys.*, 12, 498
- Lovelock, D. 1972, *J. Math. Phys.*, 13, 874
- Luppino, G. A., Gioia, I. M., Hammer, F., Le Fèvre, O., & Annis, J. A. 1999, *A&AS*, 136, 117
- Luppino, G. A., & Kaiser, N. 1997, *ApJ*, 475, 20
- Lynds, R., & Petrosian, V. 1989, *ApJ*, 336, 1
- Macciò, A. V., Dutton, A. A., & van den Bosch, F. C. 2008, *MNRAS*, 391, 1940
- Macciò, A. V., Dutton, A. A., van den Bosch, F. C., et al. 2007, *MNRAS*, 378, 55
- Majer, C. L., Meyer, S., Konrad, S., Sarli, E., & Bartelmann, M. 2013, *ArXiv e-prints*, arXiv:1304.6522
- Mandelbaum, R., Seljak, U., Cool, R. J., et al. 2006, *MNRAS*, 372, 758

- Marshall, P. J., Hobson, M. P., Gull, S. F., & Bridle, S. L. 2002, *MNRAS*, 335, 1037
- Massey, R., & Refregier, A. 2005, *MNRAS*, 363, 197
- Massey, R., Heymans, C., Bergé, J., et al. 2007, *MNRAS*, 376, 13
- Matsubara, T. 2010, *Phys. Rev. D*, 81, 083505
- Matsubara, T., & Jain, B. 2001, *ApJ*, 552, L89
- Matsubara, T., & Szalay, A. S. 2001, *ApJ*, 556, L67
- McEwen, J. D., Vielva, P., Hobson, M. P., Martínez-González, E., & Lasenby, A. N. 2007, *MNRAS*, 376, 1211
- Mecke, K. R. 2000, *Lect. Notes Phys.*, 554, 111
- Mecke, K. R., Buchert, T., & Wagner, H. 1994, *A&A*, 288, 697
- Mellier, Y., Fort, B., & Kneib, J.-P. 1993, *ApJ*, 407, 33
- Meneghetti, M., Argazzi, R., Pace, F., et al. 2007a, *A&A*, 461, 25
- Meneghetti, M., Bartelmann, M., Jenkins, A., & Frenk, C. 2007b, *MNRAS*, 381, 171
- Merkel, P. M., & Schäfer, B. M. 2013, *MNRAS*, 434, 1808
- Merten, J., Cacciato, M., Meneghetti, M., Mignone, C., & Bartelmann, M. 2009, *A&A*, 500, 681
- Merten, J., Meneghetti, M., Postman, M., et al. 2014, *ArXiv e-prints*, arXiv:1404.1376
- Mészáros, P. 1974, *A&A*, 37, 225
- Metzler, C. A., White, M., Norman, M., & Loken, C. 1999, *ApJ*, 520, L9
- Miller, L., Kitching, T. D., Heymans, C., Heavens, A. F., & van Waerbeke, L. 2007, *MNRAS*, 382, 315
- Miller, L., Heymans, C., Kitching, T. D., et al. 2013, *MNRAS*, 429, 2858
- Miralda-Escude, J. 1991, *ApJ*, 380, 1
- Miralda-Escude, J. 1992, *ApJ*, 390, L65
- Miralda-Escude, J. 1993, *ApJ*, 403, 497
- Miralda-Escude, J. 1995, *ApJ*, 438, 514
- Miyazaki, S., Komiyama, Y., Sekiguchi, M., et al. 2002, *PASJ*, 54, 833
- Molikawa, K., & Hattori, M. 2001, *ApJ*, 559, 544
- Morandi, A., Pedersen, K., & Limousin, M. 2010, *ApJ*, 713, 491
- Mukhanov, V. 2005, *Physical Foundations of Cosmology* (Cambridge University Press)
- Munshi, D., & Kilbinger, M. 2006, *A&A*, 452, 63
- Narayan, R., & Bartelmann, M. 1996, *ArXiv e-prints*, arXiv:9606001
- Navarro, J. F., Frenk, C. S., & White, S. D. M. 1996, *ApJ*, 462, 563

## BIBLIOGRAPHY

---

- Navarro, J. F., Frenk, C. S., & White, S. D. M. 1997, *ApJ*, 490, 493
- Navarro, J. F., Hayashi, E., Power, C., et al. 2004, *MNRAS*, 349, 1039
- Neto, A. F., Gao, L., Bett, P., et al. 2007, *MNRAS*, 381, 1450
- Newman, E. T., & Penrose, R. 1966, *J. Math. Phys.*, 7, 863
- Nishizawa, A. J. 2014, *Prog. Theor. Exp. Phys.*, 2014, 060000
- Nolta, M. R., Wright, E. L., Page, L., et al. 2004, *ApJ*, 608, 10
- Novikov, D., Feldman, H. A., & Shandarin, S. F. 1999, *Int. J. Mod. Phys. D*, 8, 291
- Oguri, M., Lee, J., & Suto, Y. 2003, *ApJ*, 599, 7
- Okumura, T., Jing, Y. P., & Li, C. 2009, *ApJ*, 694, 214
- Paczynski, B. 1987, *Nature*, 325, 572
- Padmanabhan, N., Hirata, C. M., Seljak, U., et al. 2005, *Phys. Rev. D*, 72, 043525
- Peacock, J. A. 2003, *Cosmological Physics* (Cambridge University Press)
- Peacock, J. A., & Dodds, S. J. 1996, *MNRAS*, 280, L19
- Peebles, P. J. E., & Ratra, B. 1988, *ApJ*, 325, L17
- Peebles, P. J. E., & Yu, J. T. 1970, *ApJ*, 162, 815
- Perlmutter, S., Aldering, G., Goldhaber, G., et al. 1999, *ApJ*, 517, 565
- Perotto, L., Lesgourgues, J., Hannestad, S., Tu, H., & Y Y Wong, Y. 2006, *J. Cosmol. Astropart. Phys.*, 10, 13
- Petri, A., Haiman, Z., Hui, L., May, M., & Kratochvil, J. M. 2013, *Phys. Rev. D*, 88, 123002
- Pietrobon, D., Balbi, A., & Marinucci, D. 2006, *Phys. Rev. D*, 74, 043524
- Planck Collaboration. 2014a, *A&A*, 571, A19
- Planck Collaboration. 2014b, *A&A*, 571, A16
- Planck Collaboration. 2015a, *ArXiv e-prints*, arXiv:1502.01582
- Planck Collaboration. 2015b, *ArXiv e-prints*, arXiv:1502.01589
- Planck Collaboration. 2015c, *ArXiv e-prints*, arXiv:1502.01595
- Prada, F., Klypin, A. A., Cuesta, A. J., Betancort-Rijo, J. E., & Primack, J. 2012, *MNRAS*, 423, 3018
- Pratten, G., & Munshi, D. 2012, *MNRAS*, 423, 3209
- Raccanelli, A., Bonaldi, A., Negrello, M., et al. 2008, *MNRAS*, 386, 2161
- Rao, R. C. 1945, *Bull. Calcutta Math. Soc.*, 37, 81
- Rassat, A., Land, K., Lahav, O., & Abdalla, F. B. 2007, *MNRAS*, 377, 1085
- Ratra, B., & Peebles, P. J. E. 1988, *Phys. Rev. D*, 37, 3406

- Refregier, A. 2003, MNRAS, 338, 35
- Refregier, A., & Bacon, D. 2003, MNRAS, 338, 48
- Riess, A. G., Filippenko, A. V., Challis, P., et al. 1998, AJ, 116, 1009
- Robertson, H. P. 1935, ApJ, 82, 284
- Rosati, P., Borgani, S., & Norman, C. 2002, ARA&A, 40, 539
- Sachs, R. K., & Wolfe, A. M. 1967, ApJ, 147, 73
- Sand, D. J., Treu, T., Smith, G. P., & Ellis, R. S. 2003, ArXiv e-prints, arXiv:0310703
- Sarli, E., Meyer, S., Meneghetti, M., et al. 2014, A&A, 570, A9
- Sato, J., Takada, M., Jing, Y. P., & Futamase, T. 2001, ApJ, 551, L5
- Sato, M., & Nishimichi, T. 2013, Phys. Rev. D, 87, 123538
- Schäfer, B. M., & Heisenberg, L. 2012, MNRAS, 423, 3445
- Schmalzing, J., & Buchert, T. 1997, ApJ, 482, L1
- Schmalzing, J., & Gorski, K. M. 1998, MNRAS, 297, 355
- Schmalzing, J., Takada, M., & Futamase, T. 2000, ApJ, 544, L83
- Schneider, P., & Bartelmann, M. 1997, MNRAS, 286, 696
- Schneider, P., van Waerbeke, L., Mellier, Y., et al. 1998, A&A, 333, 767
- Scranton, R., Connolly, A. J., Nichol, R. C., et al. 2003, ArXiv e-prints, arXiv:0307335
- Seitz, C., & Schneider, P. 1995, A&A, 297, 287
- Seitz, C., & Schneider, P. 1997, A&A, 318, 687
- Seitz, S., & Schneider, P. 1996, A&A, 305, 383
- Seitz, S., Schneider, P., & Bartelmann, M. 1998, A&A, 337, 325
- Seljak, U., & Zaldarriaga, M. 1996, ApJ, 469, 437
- Semboloni, E., Hoekstra, H., Schaye, J., van Daalen, M. P., & McCarthy, I. G. 2011, MNRAS, 417, 2020
- Shapiro, C., & Cooray, A. 2006, J. Cosmol. Astropart. Phys., 3, 7
- Sheldon, E. S., Annis, J., Böhringer, H., et al. 2001, ApJ, 554, 881
- Shirasaki, M., Yoshida, N., Hamana, T., & Nishimichi, T. 2012, ApJ, 760, 45
- Shu, C., Zhou, B., Bartelmann, M., et al. 2008, ApJ, 685, 70
- Silk, J. 1968, ApJ, 151, 459
- Simon, P., King, L. J., & Schneider, P. 2004, A&A, 417, 873
- Slipher, V. M. 1917, Proc. Am. Phil. Soc., 56, 403

## BIBLIOGRAPHY

---

- Smith, D. R., Bernstein, G. M., Fischer, P., & Jarvis, M. 2001, *ApJ*, 551, 643
- Smith, R. E., Peacock, J. A., Jenkins, A., et al. 2003, *MNRAS*, 341, 1311
- Soucail, G., Fort, B., Mellier, Y., & Picat, J. P. 1987, *A&A*, 172, L14
- Springel, V., White, S. D. M., Jenkins, A., et al. 2005, *Nature*, 435, 629
- Springel, V., Wang, J., Vogelsberger, M., et al. 2008, *MNRAS*, 391, 1685
- Straumann, N. 2006, *Mod. Phys. Lett. A*, 21, 1083
- Sugiyama, N. 1995, *ApJS*, 100, 281
- Sunyaev, R. A., & Zel'dovich, I. B. 1980, *ARA&A*, 18, 537
- Takada, M., & Jain, B. 2002, *MNRAS*, 337, 875
- Takada, M., & Jain, B. 2003, *MNRAS*, 340, 580
- Takada, M., & Jain, B. 2004, *MNRAS*, 348, 897
- Takada, M., & Jain, B. 2009, *MNRAS*, 395, 2065
- Takada, M., & White, M. 2004, *ApJ*, 601, L1
- Tchernin, C., Majer, C. L., Meyer, S., et al. 2015, *A&A*, 574, A122
- Tegmark, M., Taylor, A. N., & Heavens, A. F. 1997, *ApJ*, 480, 22
- The Dark Energy Survey Collaboration. 2005, *ArXiv e-prints*, arXiv:0510346
- Troxel, M. A., & Ishak, M. 2014a, *Phys. Rev. D*, 89, 063528
- Troxel, M. A., & Ishak, M. 2014b, *ArXiv e-prints*, arXiv:1407.6990
- Turner, M. S., & White, M. 1997, *Phys. Rev. D*, 56, 4439
- van Daalen, M. P., Schaye, J., Booth, C. M., & Dalla Vecchia, C. 2011, *MNRAS*, 415, 3649
- van Waerbeke, L., Bernardeau, F., & Mellier, Y. 1999, *A&A*, 342, 15
- Van Waerbeke, L., Mellier, Y., & Hoekstra, H. 2005, *A&A*, 429, 75
- Van Waerbeke, L., Mellier, Y., Erben, T., et al. 2000, *A&A*, 358, 30
- Vielva, P., Martínez-González, E., & Tucci, M. 2006, *MNRAS*, 365, 891
- Villumsen, J. V. 1996, *MNRAS*, 281, 369
- Viola, M., Kitching, T. D., & Joachimi, B. 2014, *MNRAS*, 439, 1909
- Vogeley, M. S., & Szalay, A. S. 1996, *ApJ*, 465, 34
- Vogelsberger, M., Genel, S., Springel, V., et al. 2014, *MNRAS*, 444, 1518
- Voit, G. M. 2005, *Rev. Mod. Phys.*, 77, 207
- Walker, A. G. 1935, *Quart. J. Math.*, 6, 81
- Wang, L., & Steinhardt, P. J. 1998, *ApJ*, 508, 483

- Wechsler, R. H., Bullock, J. S., Primack, J. R., Kravtsov, A. V., & Dekel, A. 2002, *ApJ*, 568, 52
- Wetterich, C. 1988, *Nucl. Phys. B*, 302, 668
- White, M., & Hu, W. 2000, *ApJ*, 537, 1
- Winitzki, S., & Kosowsky, A. 1998, *New A*, 3, 75
- Wittman, D. M., Tyson, J. A., Kirkman, D., Dell'Antonio, I., & Bernstein, G. 2000, *Nature*, 405, 143
- Wolz, L., Kilbinger, M., Weller, J., & Giannantonio, T. 2012, *J. Cosmol. Astropart. Phys.*, 9, 9
- Wright, C. O., & Brainerd, T. G. 2000, *ApJ*, 534, 34
- Zel'dovich, Y. B. 1970, *A&A*, 5, 84
- Zel'dovich, Y. B. 1972, *MNRAS*, 160, 1P
- Zel'dovich, Y. B., & Sunyaev, R. A. 1969, *Ap&SS*, 4, 301
- Zhao, D. H., Jing, Y. P., Mo, H. J., & Börner, G. 2003, *ApJ*, 597, L9



# Acknowledgments

As I finish this dissertation, it appears to me the hardest thing I have ever done. While this assessment is likely to be revised in the future, it seems safe to say I would not have managed this feat without the support and confidence of a number of people.

First and foremost I would like to thank my supervisor, Matthias Bartelmann, who invited me on this project and has guided me through many difficulties. His enthusiasm is remarkable, and he has never failed to bring up new ideas when faced with bleak results. I am grateful for his encouragement and patience.

Björn Schäfer has also provided much support and could not be more humble, kind or eager to help. His creativity and love of physics are truly inspiring, and I have enjoyed his frequent visits to our office immensely.

I would like to thank the board of examiners: Prof. Dr. Volker Springel, who kindly agreed to review this dissertation, Prof. Dr. Jörg Jäckel and Prof. Dr. Ulrich Uwer.

I am grateful for funding from the Baden-Württemberg-Stiftung and the Deutsche Forschungsgemeinschaft (DFG). I would also like to thank those people who make the dreaded ‘paperwork’ a little less dreadful: Elisabeth Miller and Gesine Heinzlmann of the Heidelberg Graduate School of Fundamental Physics (HGSFP), Christian Fendt of the International Max Planck Research School for Astronomy and Cosmic Physics at the University of Heidelberg (IMPRS-HD), and of course Anna Zacheus at the Institute for Theoretical Astrophysics (ITA).

I owe thanks to my colleagues at ITA, to some more than to others. Most importantly, Philipp Merkel appointed himself my mentor, and although he would deny it, I doubt that I would have finished this PhD without his support. I would like to thank him for his assistance with the cosmic shear project, which he initiated, and for proofreading this thesis, but most importantly for his advice and his readiness to answer questions. He has also kindly provided me with hours of entertainment and generous amounts of chocolate. Charles Majer has become a friend beyond the workplace. Matthias Redlich, with whom I was lucky to share an office for two years, also stands out for his unquenchable cheerfulness and the countless times he has offered his help. I am grateful to Sven Meyer, my companion in several lectures and seminars, Christian Angrick, Korbinian Huber and Alexander Gelsin, and to my office-mates over the years, Christoph Kommer, Daniel Berg, Celia Viermann and Carsten Littek.

Most of my friends are scattered across different cities, and given that we consequently do not see each other as often as I would wish, it means all the more to me that I have always been able to rely on them, in particular Maria Bous, who always takes time for me and makes things seem much brighter; Anna Labentz, my shoulder to cry on and the epitome of positive attitude, along with Ondřej; Christian Wittemeier, who never fails to make me smile; and Sang-Hee Cho and Nora Schmidt.

While I trust that my family know how much I appreciate their support, I would like to mention them here, though I cannot find the right words. My sister Katrin has listened patiently to my complaints and worries, for which I would like to apologise, and has always given me a nudge when I needed one. Our weekends and vacations together have been a welcome distraction. Finally, I would like to thank my parents for everything they have done for me.

